STUDIES OF TRIAXIAL ROTORS AND BAND MIXING IN NUCLEI

A Thesis
Presented to
The Academic Faculty

by

James Mitchell Allmond

In Partial Fulfillment
of the Requirements for the Degree
Doctor of Philosophy in
Physics

School of Physics
Georgia Institute of Technology
May 2007

STUDIES OF TRIAXIAL ROTORS AND BAND MIXING IN NUCLEI

Approved by:

John L. Wood, Advisor
School of Physics
Georgia Institute of Technology

Brian Kennedy
School of Physics
Georgia Institute of Technology

Walter A. de Heer
School of Physics
Georgia Institute of Technology

Rebecca Howell
School of Mechanical Engineering
Georgia Institute of Technology

Raymond Flannery
School of Physics
Georgia Institute of Technology

Date Approved: 3 April 2007

To my family and friends

for their support and guidance.

ACKNOWLEDGEMENTS

I want to thank John Wood most of all. John has gone beyond the call of duty in all his support and efforts. Whether help or advice was needed in classwork, research, or life, John made time for you. His ability to communicate and provide simple explanations made "difficult" physics simple. He's an inspiration that will be hard to match. Thank you John for all your help and support.

I would also like to thank David Kulp. David has provided countless help and advice with technical issues and has helped guide my understanding of nuclear physics. His patience and guidance has been greatly appreciated.

Lastly, I want to thank my parents. They have given me unconditional support during these years of school and they have been infinitely understanding throughout. I thank you and I love you both.

TABLE OF CONTENTS

LIST OF TABLES

LIST OF FIGURES

SUMMARY

Rigid rotor models were investigated with constraints from data for even-even nuclei. Specifically, from precision gamma-ray intensity measurements for ^{166}Er (from ^{166m}Ho and ^{166}Tm beta decays); from $B(E2)$ systematics; and for ^{186,188,190,192}Os transition $E2$ matrix element data.

CHAPTER I

INTRODUCTION

Even-even nuclei are known to have 0^+ (zero angular momentum and even parity) ground states and several low-energy integer spin states. The transition strengths between these levels are sufficiently strong and well established to support the view that most nuclei are collective. While the full and true structure of these nuclei is not known, the structure is clearly dominated by low spin degrees of freedom. To establish a reference frame in which we can discuss and compare data, models of adiabatic rotations are by far the most useful. To first order this is the best starting point for viewing selection rules and transition strengths.

1.1 Basic Nuclear Structure

The basic framework in which nuclear structure is placed is the shell model. This divides nuclei across the mass surface into closed and near-closed shell nuclei, which are spherical and weakly collective, and open-shell nuclei, which are collective.

There is a further simplification due to pairing. Pairing in doubly-even nuclei produces an energy gap that separates the ground state from the large number of "unpaired" states. Within this energy gap one observes a few excited states which are collective states, i.e., states resulting from correlations among the nucleons. Empirically, one deduces these correlations to be due to simple collective motion such as rotations and vibrations.

The collective model was a result of two major works: the liquid drop model for describing nuclear fission (which was developed largely by N. Bohr [1] and initiated the possibility of deformation), and the observation of large electric quadrupole moments in nuclei by J. Rainwater [2]. These two works provided the basis for the Bohr collective model [3]. However, the first account of a quantum rigid rotor (applied to molecules) was considered

by R.L. Kronig and I.I. Rabi [4].

Following A. Bohr's original study, details of the quantum rigid rotor applied to nuclei were worked out in detail. Selection rules (body projection, K, selection rules) and general intensity rules for the model were derived by G. Alaga [5]. This paved the way for simple, algebraic models. V.M. Mikhailov developed a simple linear theory [6] for collective rotations proportional to Alaga's intensity rule (where the linearity is in the spin difference $I_f(I_f+1)-I_i(I_i+1)$). This theory was based on a perturbation expansion of the $\Delta K = \pm 2$ mixing that occurs in the Bohr collective model (see in CHAPTER 3.3, Equation (24)). The Bohr collective model was then widely developed by A. Bohr and B. Mottelson [7] (where they made use of Alaga and Mikhailov's findings).

The triaxial quantum rigid rotor (see in CHAPTER 3.3, Equation (22)) was introduced by Davydov and Filippov [8] (where they assumed irrotational flow moments of inertia), and it was further developed and reviewed by Davydov [9].

Electromagnetic processes in nuclei were first explored by Weisskopf who introduced the concept of a single-particle unit. This described electromagnetic processes in terms of a single particle in a shell model orbit. Early experimental work [10] following A. Bohr's original paper revealed electric quadrupole transitions with strengths of 100's of "Weisskopf" units (which implies collectivity amongst the nucleons). The total transition probability for an electric multipole ($E\lambda$) process is

$$\Lambda(E\lambda;\, I_1 \rightarrow I_2) = \frac{8\pi(\lambda+1)}{\hbar\lambda[(2\lambda+1)!!]^2}\left(\frac{E_\gamma}{\hbar c}\right)^{2\lambda+1} B(E\lambda;\, I_1 \rightarrow I_2) \;\; \text{sec}^{-1} \tag{1}$$

where E_γ is in MeV and $B(E\lambda)$ is in units of $e^2(\text{fm})^{2\lambda}$. Therefore, the total transition probability for an electric quadrupole ($E2$) transition is

$$\Lambda(E2) = 1.22 \times 10^9\, E_\gamma^5\, B(E2) \;\; \text{sec}^{-1}. \tag{2}$$

The quantity, $B(E\lambda)$, is known as the reduced transition probability and it is unique to the structure of a specific nucleus. For quadruple transitions (which is the dominant mode for

collective nuclei), it is common to use $B(E2)$'s to test and compare models, and it is done in units of $e^2{\cdot}b^2$ (where 1 b = 100 fm^2) or in units of w.u. (where $e^2{\cdot}b^2 = (5.94{\times}10^{-6})A^{4/3}$ w.u.).

1.2 First Order Rotor and Vibrator Systematics

There are two types of collective motion assumed here: vibrational (near closed shells) and rotational (far from closed shells). The energy and reduced transition probability ratios for these simple models are shown in Table 1. These constant ratios, when compared to

Table 1: First order energy and reduced $E2$ transition probability ratios for a rigid rotor and vibrator.

	Rotor	Vibrator
$\frac{\text{Energy}(I{=}4)}{\text{Energy}(I{=}2)}$	3.333	2.000
$\frac{B(E2;\, I{=}4{\rightarrow}I{=}2)}{B(E2;\, I{=}2{\rightarrow}I{=}0)}$	1.429	2.000
$\frac{B(E2;\, I{=}6{\rightarrow}I{=}4)}{B(E2;\, I{=}4{\rightarrow}I{=}2)}$	1.573	3.000
$\frac{B(E2;\, I{=}8{\rightarrow}I{=}6)}{B(E2;\, I{=}6{\rightarrow}I{=}4)}$	1.647	4.000

systematic data, provide a means for evaluating the dominant properties of collective nuclei.

Nuclear data systematics (Evaluated Nuclear Structure Data File, ENSDF, [11]) are tabulated with a search engine (Georgia Tech Nuclear Data Search Engine, GTNDSE, [12]). These tabulated systematics are used to test models. The first order relations of the rotor and vibrator, Table 1, are compared to the horizontal systematics in Figure 1 through Figure 3.

Figure 1 through Figure 3 shows that most collective nuclei are rotational with respect to their reduced $E2$ transition probabilities. The energy ratios in Figure 1 show that nuclei range from the rotor ratio limit to a little below the vibrational ratio limit. Most collective nuclei appear to be more rotational than vibrational. The collective rotor is therefore used as the basis for describing even-even collective nucei.

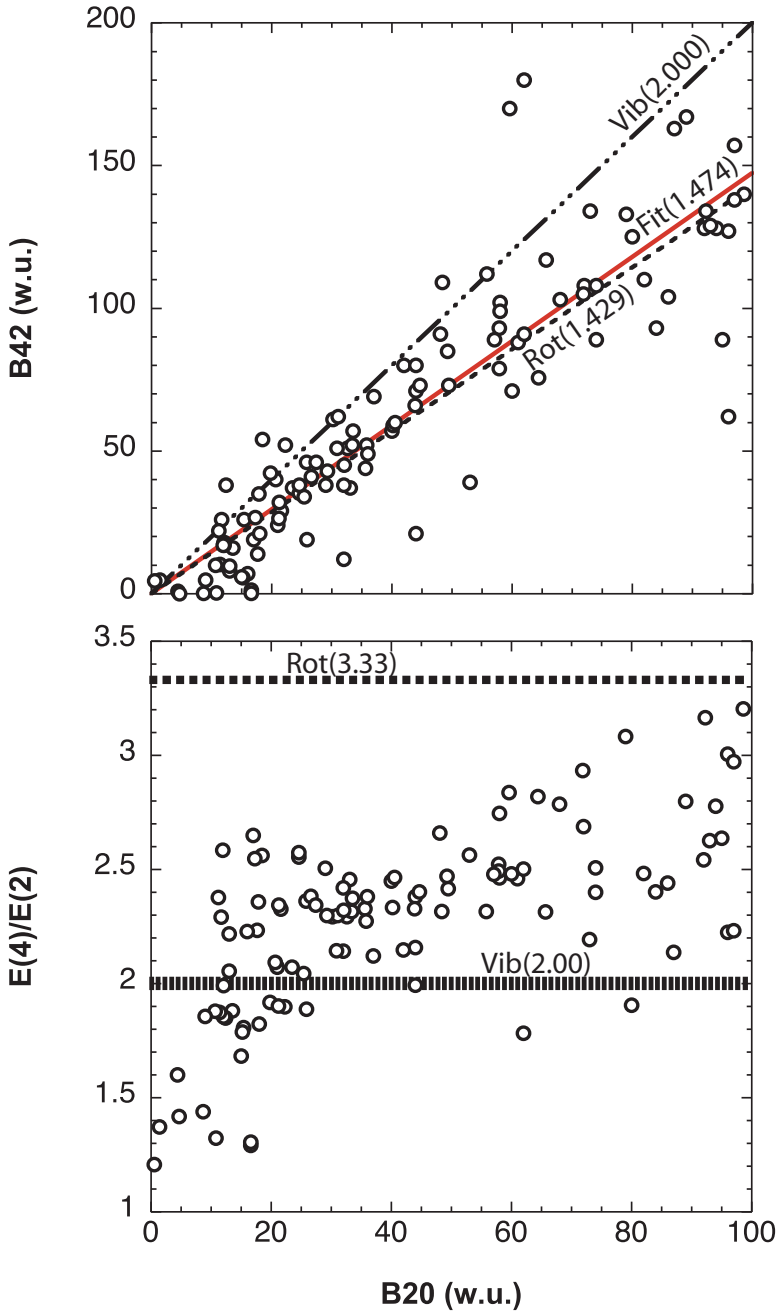

Figure 1: Systematics from the ENSDF [11] database of even-even nuclei $Z \geq 56$ acquired using GTNDSE [12]. The values plotted are reduced $E2$ transition probabilities (in Weisskopf units, w.u.) of the 2nd excited state to the first excited state, $B(E2; I^\pi = 4^+ \rightarrow I^\pi = 2^+)$, and the energy ratios of the 2nd and 1st excited state, $E(I^\pi = 4^+)/E(I^\pi = 2^+)$. These quantities are plotted against the reduced $E2$ transition probabilities of the 1st excited state to the ground state, $B(E2; I^\pi = 2^+ \rightarrow I^\pi = 0^+)$. The selection is for the "less-collective" nuclei, i.e., the strongly-collective, rotational nuclei are not included.

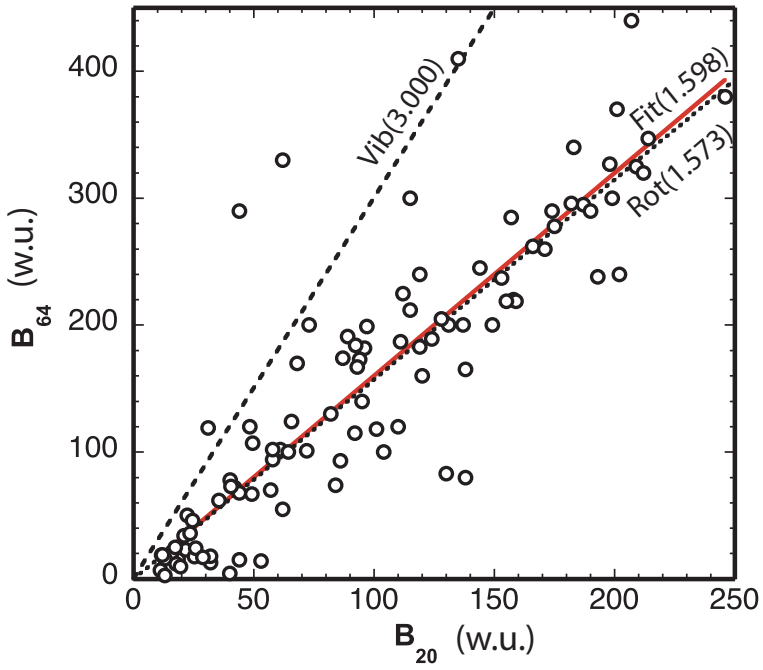

Figure 2: ENSDF [11] systematics of $B(E2;\, I^\pi = 6^+ \rightarrow I^\pi = 4^+)$ vs. $B(E2;\, I^\pi = 2^+ \rightarrow I^\pi = 0^+)$.

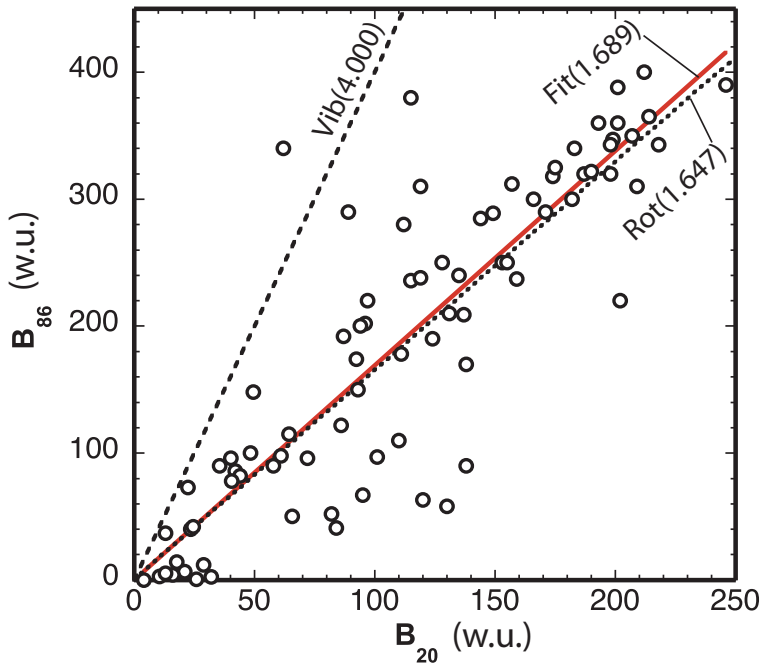

Figure 3: ENSDF [11] systematics of $B(E2;\, I^\pi = 8^+ \rightarrow I^\pi = 6^+)$ vs. $B(E2;\, I^\pi = 2^+ \rightarrow I^\pi = 0^+)$.

1.3 Precision Test of Rotor

A precision test (the most precise test ever done) of the rotor model is conducted with relative γ-ray intensities from ^{166}Er. This well deformed nucleus is one of the best candidates for a near symmetric rotor. With a detailed precision study, it can provide a measure for the validity of a rotor description and an understanding of its breakdown.

For well deformed nuclei, the zeroth order energies and electric quadrupole properties can be described by a rotor. First order correction terms to the energy, $I^2(I+1)^2$, can be applied to achieve $\pm 1\%$ agreement at $I^+ = 10^+$. Precise measurements for the electric quadrupole properties have been lacking due to the difficulty in measuring them (e.g., lifetime measurements for rotational states). The difficulty in determining these properties has been circumvented by using branching ratios between bands. The precision study agrees with the rotor description at the 0.62% precision level.

1.4 Basic Rotor Model Development

The rotor is first developed to represent near symmetric nuclei as a limit of the general form. This limit provides excitation bands (non-zero body projections on the symmetry axis, e.g., for $K = 0$, $I = 0, 2, 4, 6, \ldots$ and for $K = 2$, $I = 2, 3, 4, 5, 6, \ldots$) but it provides no mixing between them. However, asymmetry in the electric quadrupole (as opposed to the inertia) can provide transitions between the bands. This limit of the general rotor model has a diagonal Hamiltonian and unmixed rotational states.

Mikhailov theory [6] is used and expanded upon to analyze the precision data in the ^{166}Er study. This limit of the rotor is used in describing near symmetric nuclei that have minimal mixing between bands. Mikhailov theory is useful for describing branching ratios between bands of different spin, I^+. Therefore, it provides a means for relating relative intensities to absolute intensities.

The rotor model is also developed in general form (triaxial rotor model) to allow unique moments of inertia and rotation about each axis (i.e., asymmetric deformed nuclei with

mixing between the bands). The triaxial rotor model has historically tied the moments of inertia to an assumption of irrotational flow [8]. No such assumption is made here and it is left in general form.

The triaxial rotor model is used side-by-side with Mikhailov theory to study the ^{166}Er precision data and to understand the breakdown of the rotor. The triaxial rotor model is also used to analyze global systematics of collective even-even nuclei in order to determine its global applicability and to understand the failure of irrotational flow. Finally, the triaxial rotor model is used (with the precise knowledge of how it breaks down for a near symmetric rotor) to test the opposite situation of extremely asymmetric nuclei. The ^{186,188,190,192}Os isotopes are among the best candidates of triaxial nuclei and are fitted to the model to investigate the breakdown of the model (which is the same breakdown seen in the ^{166}Er study but with a larger effect and an additional breakdown for $K > 2$).

CHAPTER II

ERBIUM-166 AND PRECISION SPECTROSCOPY

The motivation for studying ^{166}Er is attributed to it being a very deformed, $E(4_1^+)/E(2_1^+) = 3.30$, and near symmetric, $B_{42}/B_{20} = 1.45$, rotor (cf., Table 1 and Figure 1). Furthermore, the ground band ($K = 0$) and gamma band ($K = 2$) are well isolated from other excited bands. This avoids mixing with those bands.

The study of ^{166}Er has been well established by Bohr and Mottelson (who chose it as a case study in their monograph [7]) and by a few individuals who have pursued developing it as a standard for detector photopeak efficiency calibration [13].

2.1 Experimental Details

The present study (and see [14]) was carried out using the 8π spectrometer [15]. This is an array of 20 Compton-suppressed Ge detectors, shown in Figures 4 and Figure 5, with (nominal) characteristics of: volume = 115 cm^3, diam. = 51.5 mm, resolution = 3.0 keV FWHM @ 1332 keV, peak:total = 0.48 @ 677 keV. The array was configured with source-to-detector distances of 22.0 cm and detectors were pairwise distributed at angles(no. pairs) of 41.8°(60), 70.5°(120), 109.5°(120), 138.2°(60), and 180.0°(20). The pairwise angle combinations result in very low angular correlation distortions (e.g., 0.57% and 1.50% attenuations for 4-2-0 and 2-4-2 spin cascades, respectively) for coincidence intensities. A ^{166m}Ho source (5 ml solution of $HoCl_3$ dissolved in 0.1 M HCl) was obtained from Isotope Products Laboratories (Burbank, CA.). This source contained (4.7±0.2)% ^{154}Eu, determined as a disintegration rate in this study, and had a strength of ∼9μCi. A 3.8 cm tall, 1.0 cm diameter glass vial inside of a 5.1 cm tall, 1.6 cm diameter polyethylene screw-top sample cylinder held the liquid during the measurement. Sources of ^{166}Tm were produced via the decay of ^{166}Yb ($T_{\frac{1}{2}} = 56.7$ h), made using the ^{166}Er(α, $4n$) reaction by bombarding 96.3% enriched $^{166}Er_2O_3$ powder with a 50 MeV ^{4}He beam from the LBNL 88″ cyclotron. The oxide powder was dissolved in

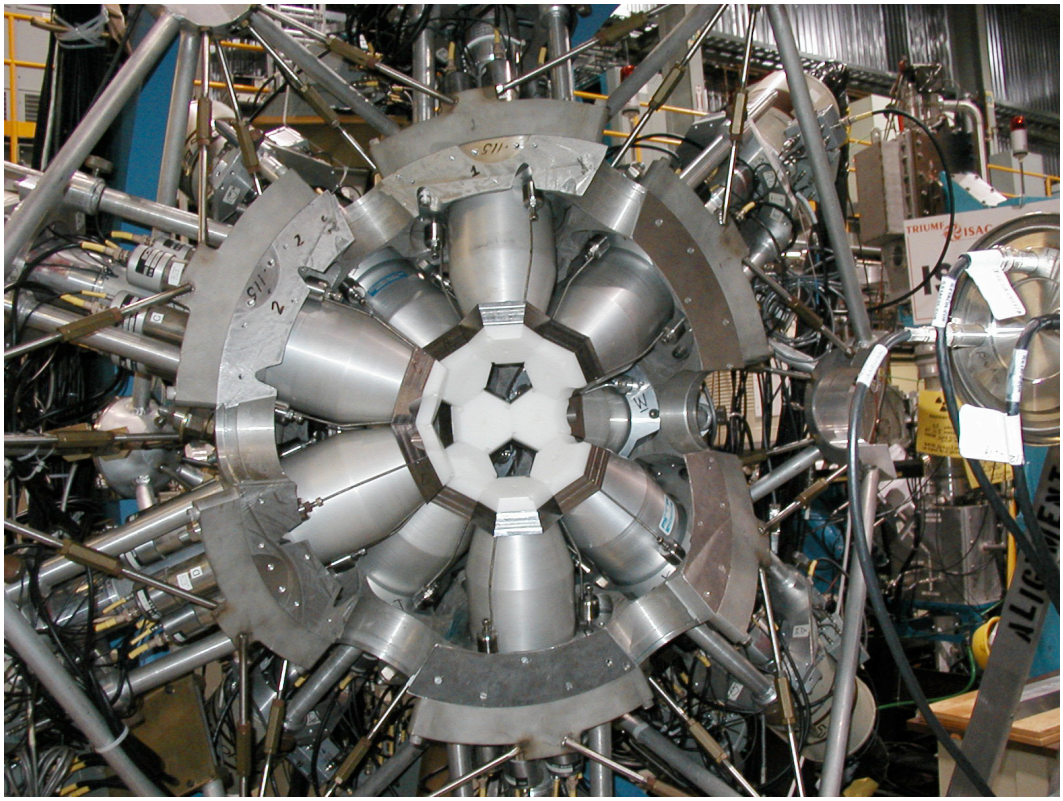

Figure 4: View of the 8π array when open. This array consists of 20 Compton-suppressed Ge detectors (see text for details).

HNO_3 and the resulting solution was packaged similarly to the ^{166m}Ho source for measurement in the 8π spectrometer; typical source strengths were $\sim 25\mu$Ci. Source impurities included ^{167}Tm and ^{165,168}Tm (traces).

In the ^{166m}Ho decay study we obtained a total of 1.5×10^8 $\gamma\gamma$ coincidence events in a running time of 107 hours. In the ^{166}Tm decay study we obtained a total of 2.9×10^8 $\gamma\gamma$ coincidence events in a running time of 266 hours.

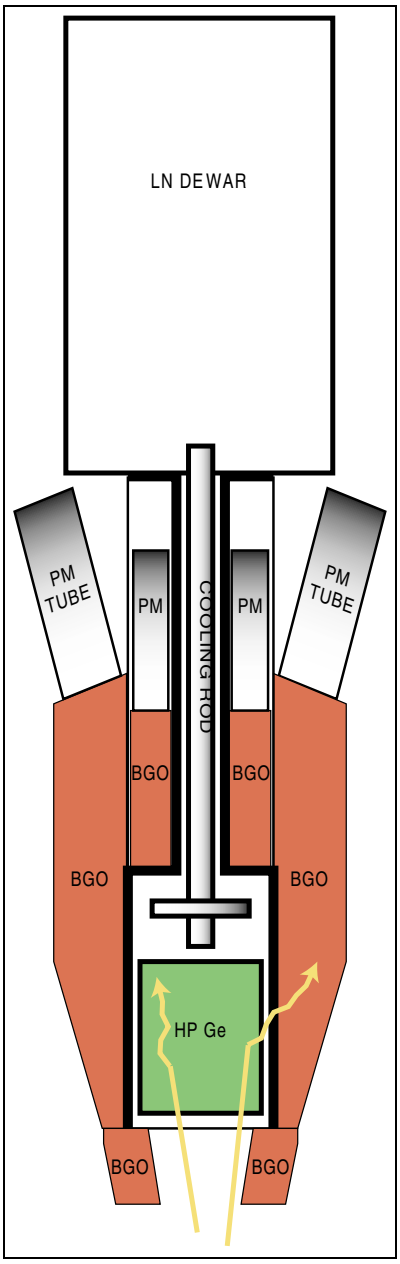

Figure 5: Schematic view [16] of an individual unit of the 8π array showing the configuration for Compton suppression. Positions of the high-purity (HP) Ge crystal, Bismuth Germanate (BGO) suppression crystals, and photomultiplier (PM) units are shown. The interaction of γ-rays is also shown schematically. The Ge crystal is cooled by liquid nitrogen (LN).

2.2 Level Schemes and Transitions from Beta Decay

The gamma-ray decay of ^{166}Er [17] was studied as described above following $\beta^{+/-}$ decay or ϵ^{+} (electron capture) of parent nuclei. The isotopes ^{166m}Ho and ^{166}Tm were used in this study for their strong feeding into the ground band ($K^{\pi} = 0^{+}$) and gamma band ($K^{\pi} = 2^{+}$) of ^{166}Er. The half-life of ^{166m}Ho is 1.2×10^{3} yr with a decay energy of $Q^{-} = 1853.9$ keV. The decay feeds states of $I^{+} \geq 6^{+}$. The half-life of ^{166}Tm is 7.70 hr with a decay energy of $Q^{+} = 3047$ keV. The decay feeds states of $I^{+} \leq 4^{+}$. Figure 6 shows the beta-decay processes.

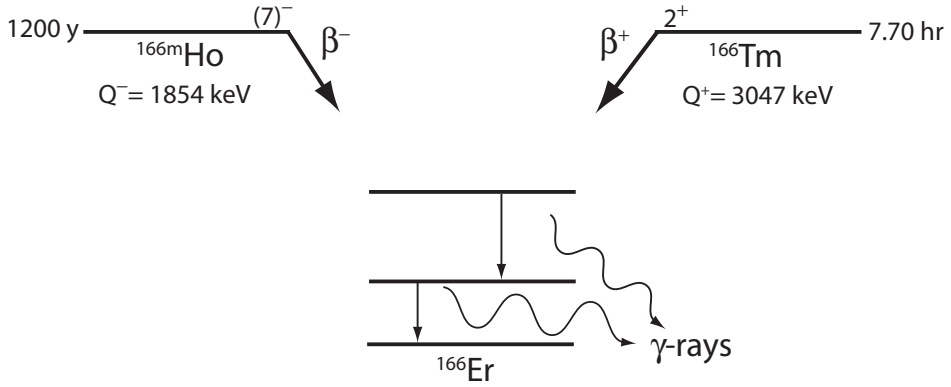

Figure 6: Beta decay of ^{166m}Ho and ^{166}Tm to ^{166}Er.

The gamma-ray spectrum of ^{166}Er, following the ^{166m}Ho β^{-} decay, is shown in Figure 7. The two largest peaks are at 184 keV and 280 keV. These two peaks are from transitions in the ground band (i.e., $I^{\pi} = 4^{+}$ to $I^{\pi} = 2^{+}$ and $I^{\pi} = 6^{+}$ to $I^{\pi} = 4^{+}$).

The level diagram for ^{166}Er that is relevant to the present discussion is given in Figure 8. The two bands ($K^{\pi} = 0^{+}$, 2^{+}) shown are isolated from other bands in excitation energy. This isolation makes ^{166}Er very attractive for study since mixing effects with other bands can be ignored. The low-energy $E(2_1^{+})$ (80.6 keV) and high-energy $E(2_2^{+})$ (785.9 keV) [1] suggest a very deformed and near axially symmetric structure.

[1]The following interchange of notation is used here: I_g(even) = I_1(even), I_γ(even) = I_2(even), and I_γ(odd) = I_1(odd), (e.g., the states are labeled either by their band name, ground(I_g) and gamma(I_γ), or by their order of appearance in energy where odd spin states first appear in the gamma band).

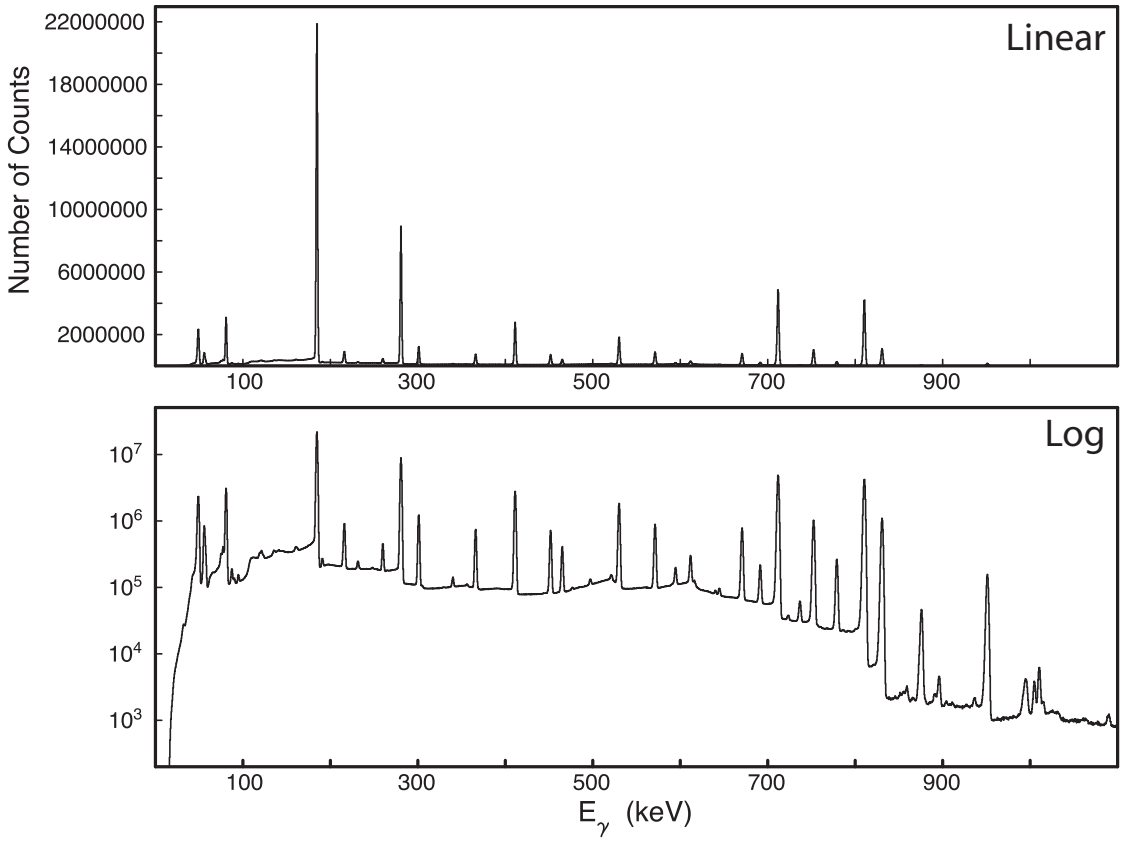

Figure 7: Linear and log based gamma-ray spectra following the β^- decay of ^{166m}Ho to ^{166}Er [14]. The x-axis represents the gamma-ray energy and the y-axis represents the number of events detected at a given energy.

Gamma-gamma coincidences are used to isolate decay scheme details from the data. The spectra in Figure 7 show all events in a single display. A coincidence "gate" is constructed by choosing a peak and nearby background region where equal channels are used in both. The coincidence spectrum, to first order, has transitions (photopeaks) that either feed or follow the transition (peak) selected in the coincidence gate. The technique is extremely powerful for organizing the order of events, assigning spins, separating unresolved peaks, and identifying artifacts (e.g., sum peaks).

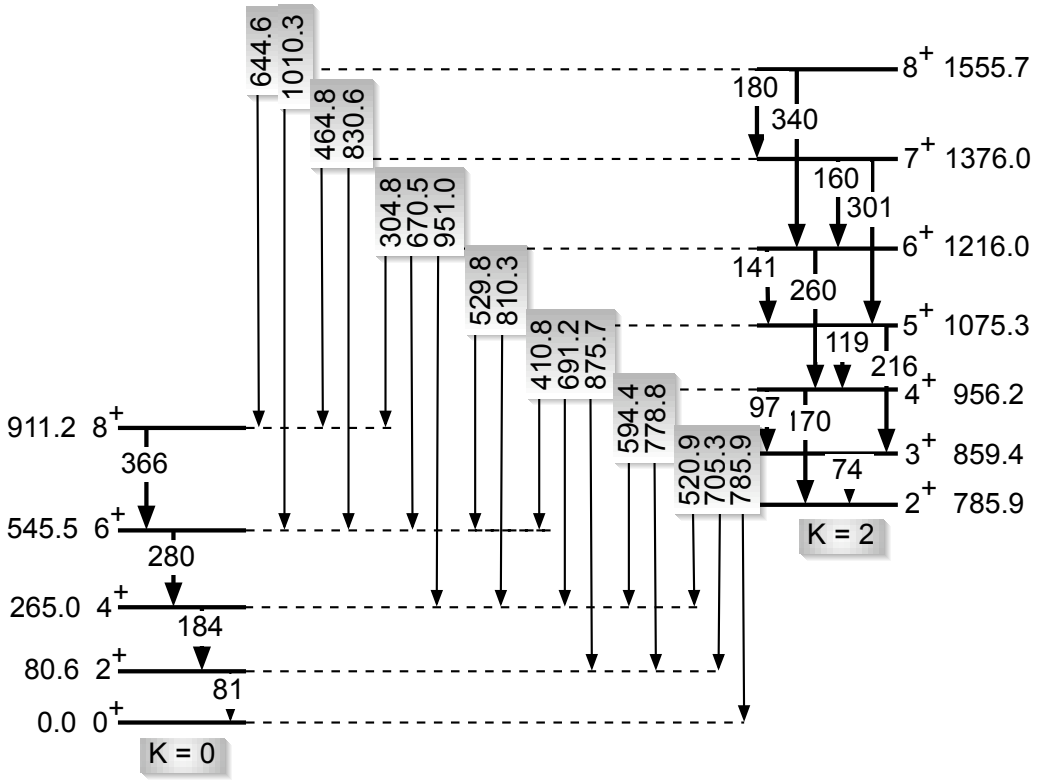

Figure 8: Energy level diagram [14] for ^{166}Er. The $\Delta K = -2$ transitions are highlighted in the center. The high spin interband transitions involving $I = 6$ and $I = 8$ are of specific interest in testing the limits of the rotor model.

2.3 Calibration and Reduction of Data

The goal of the present study is the precise determination of gamma-ray intensities, particularly those corresponding to weak transitions (which are poorly known). The response of a detector to gamma radiation is characterized by

$$\text{Peak-Area(Energy)} = \text{Efficiency(Energy)} \times \text{Intensity(Energy)}. \tag{3}$$

This requires the determination of the relative efficiency of the detector as a function of energy. Because intensities were measured in coincidence mode it was necessary to determine the efficiency of the detectors in coincidence mode. This was carried out using strong lines (184, 280, 366, 530, 594, 670, 691, 779, 810, 831, 951, 1147, 1241, 1401, 1427) in the 81, 184, and 280 coincidence gates. The intensities of these strong lines are known to a precision of, respectively, 1.00%, 0.73%, 0.88%, 0.67%, 1.16%, 0.53%, 1.08%, 0.71%, 0.34%, 0.52%, 0.31%, 2.16%, 2.24%, 0.99%, and 2.16% [17]. The efficiency curve is shown in Figure 9.

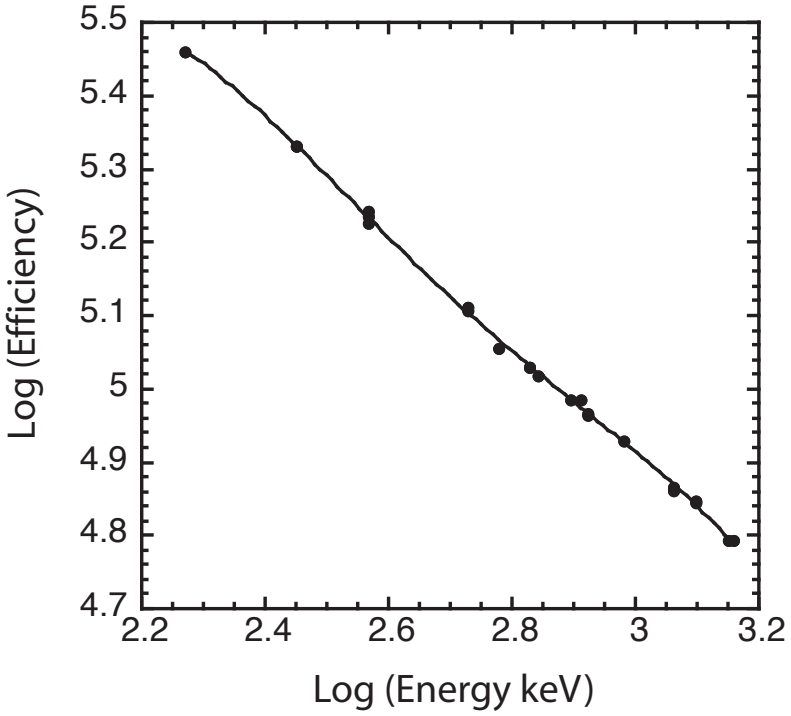

Figure 9: Gated calibration photopeak efficiency curve for the ^{166m}Ho and ^{166}Tm $\beta^{-,+}$ decay. A 4th order polynomial was used for the calibration fit. Log(Eff) = $-66.523395 + 109.239675x - 61.222966x^2 + 15.062887x^3 - 1.382375x^4$, where $x = \mathrm{Log}(E)$ and $\Delta_{\mathrm{Avg.pt.dev.}} = 0.853\%$.

High statistics are needed to resolve weak transitions in coincidence spectra. A minimum of 400 events must be measured in a peak for it to have a statistical error of 5% (e.g., Poisson error of $\sqrt{N}/N$). Figure 10 shows the weak transition at 304.8 keV ($6_\gamma \rightarrow 8_g$) and the quality of the data. The transition can only be seen in a coincidence spectrum (e.g., from a 365 keV, $8_g \rightarrow 6_g$ gate). The weak transition has an intensity that is 1/2500 of the strongest interband transition (810 keV, $5_\gamma \rightarrow 4_g$) in this study. An accurate determination of this weak high-spin transition is critical for testing the limits of the rotor model.

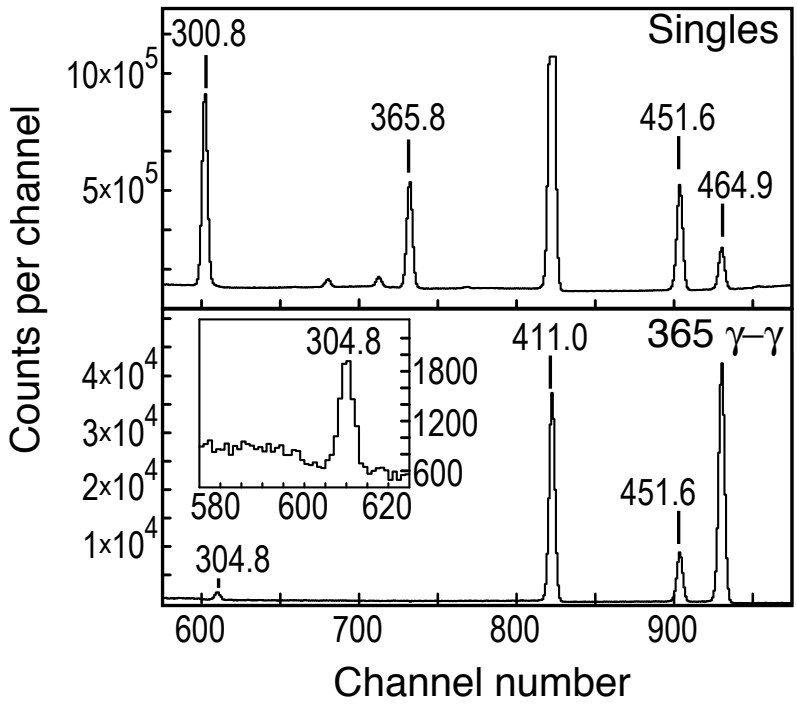

Figure 10: Weak transition for 304.8 keV ($6_\gamma \rightarrow 8_g$) where $I_\gamma(304.8\ keV) = \frac{2.28\times10^{-2}}{100\beta^-(^{166m}\mathrm{Ho})}$. It is obscured by a strong and nearly degenerate peak in the singles spectrum. It is revealed in a 365 keV ($8_g \rightarrow 6_g$) $\gamma - \gamma$ coincidence gate.

2.4 Corrections to Data

A detailed summing analysis was carried out for the data. Figure 11 shows the 1010 keV ($8_\gamma \rightarrow 6_g$) peak for the 184 keV and 280 keV coincidence gates. Since this high spin transition is an extremal point for the rotor model, precision is needed. The 280 keV gated coincidence spectrum contains a sum peak at 1015.3 keV ($\Sigma = 184 + 831$). In order to avoid this artifact, the 184 keV gate was used instead. Typical summing losses were found to be 0.50% and typical summing gains were found to be 0.24%. This was determined to be too low to impact the precision of the study.

The 521.2 keV ($2_\gamma \rightarrow 4_g$) transition, following the ^{166}Tm decay, rests on a large Compton bump in the 1374 keV ($2160 \rightarrow 2_\gamma$) gated spectrum, Figure 12. The Compton artifacts are from 705.8 keV ($2_\gamma \rightarrow 2_g$) and 786.4 keV ($2_\gamma \rightarrow 0_g$). The Compton bump under the 521.2 keV peak is from the 705.8 keV Compton continuum and it was deduced by using the Compton bump from the 786.4 keV Compton continuum (where the bump was corrected

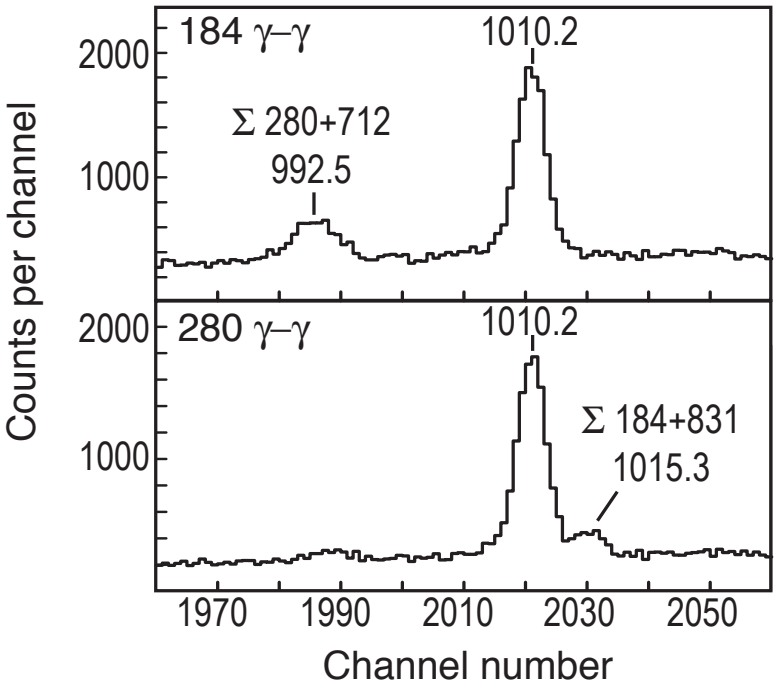

Figure 11: Gated coincidence spectra, 184 keV $\gamma-\gamma$ and 280 keV $\gamma-\gamma$, showing 1010.2 keV ($8_\gamma \rightarrow 6_g$). The 184 keV $\gamma - \gamma$ gate is used to avoid summing artifacts at 1015.3 keV.

for the γ-ray energy dependence).

Corrections for $M1$ admixtures, $\delta(E2/M1)$, must be accounted for in converting the $\Delta I = 0, 1$ transition intensities to reduced $E2$ transition probabilities, $B(E2)$. The admixtures can be deduced from γ-ray angular correlation measurements or distribution measurements carried out on nuclei oriented at low temperature. The work done by Hamilton *et al.* [18] and J. Loats [19] was adopted for establishing the $\delta(E2/M1)$ mixing ratios. The interband transitions relevant to the present study are all uniformly $\geq$ 99.7% $E2$ strength. The exception is for the $8_\gamma \rightarrow 8_g$ transition with an $E2$ strength of $96.0^{+2.1}_{-2.5}$%.

The results of the precision spectroscopy work are summarized in Table 2. The relative intensities have been normalized to absolute intensities. They are all $\sim$ 100% $E2$ strength except for the $8_\gamma \rightarrow 8_g$ transition (which is 96.0% $E2$ strength). These precision measurements provide a valuable means for testing the rotor model (discussed later).

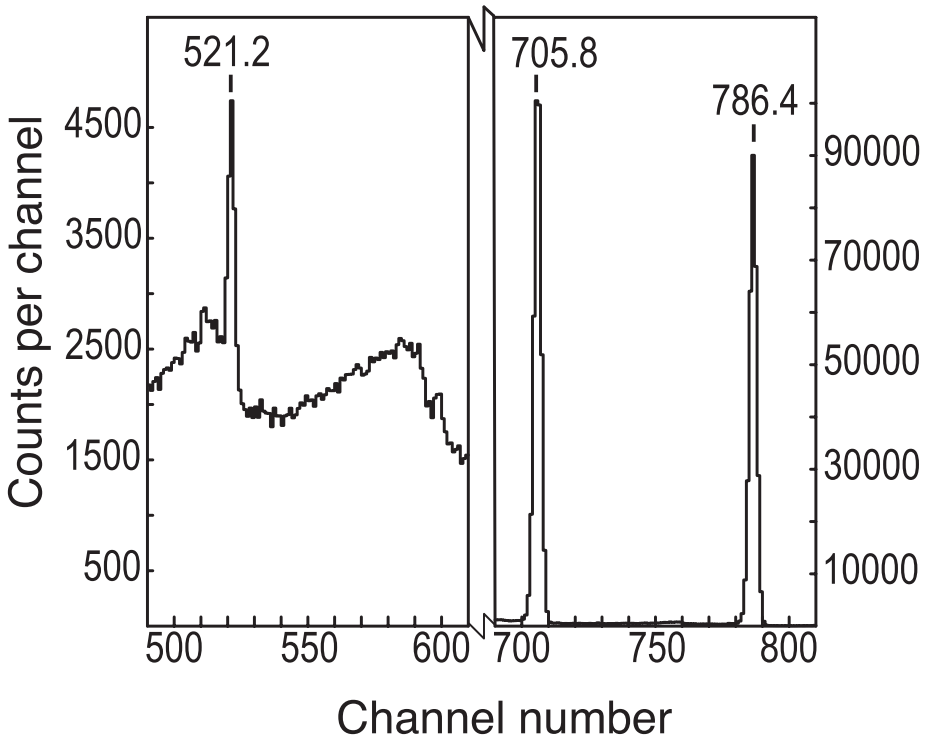

Figure 12: The gated coincidence sectrum (1374 keV, $2160 \rightarrow 2_\gamma$), following the ^{166}Tm β^+ decay, possess large Compton artifacts at and around 521.2 keV ($2_\gamma \rightarrow 4_g$) from transitions at 705.8 keV ($2_\gamma \rightarrow 2_g$) and 786.4 keV ($2_\gamma \rightarrow 0_g$).

Table 2: Gamma-ray transitions relevant to the present study and the intensities adopted.

Transition	Energy(keV)[1]	Intensity[2]	$\Delta I\%$	Source[3]
$8_\gamma \rightarrow 8_g$	644.61	0.2097	1.38%	Ho
$8_\gamma \rightarrow 6_g$	1010.29	0.1096	1.75%	Ho
$8_\gamma \rightarrow 6_\gamma$	339.74	0.226	1.55%	Ho
$7_\gamma \rightarrow 8_g$	464.80	1.639	1.15%	Ho
$7_\gamma \rightarrow 6_g$	830.58	13.52	0.52%	NDS
$7_\gamma \rightarrow 5_\gamma$	300.76	5.14	0.58%	NDS
$6_\gamma \rightarrow 8_g$	304.82	0.0314	3.71%	Ho
$6_\gamma \rightarrow 6_g$	670.50	7.55	0.53%	NDS
$6_\gamma \rightarrow 4_g$	950.97	3.795	0.32%	NDS
$6_\gamma \rightarrow 4_\gamma$	259.74	1.446	1.17%	Ho
$5_\gamma \rightarrow 6_g$	529.80	13.35	0.67%	NDS
$5_\gamma \rightarrow 4_g$	810.28	80.0	0.38%	NDS
$5_\gamma \rightarrow 3_\gamma$	215.89	3.59	1.95%	NDS
$4_\gamma \rightarrow 6_g$	410.80	0.0233	2.23%	Tm[4]
$4_\gamma \rightarrow 4_g$	691.25	1.85	1.08%	NDS
$4_\gamma \rightarrow 2_g$	875.65	1.026	1.59%	(Ho,Tm[4])[5]
$4_\gamma \rightarrow 2_\gamma$	170.31	0.0197	2.91%	Ho
$3_\gamma \rightarrow 4_g$	594.43	0.775	1.16%	NDS
$3_\gamma \rightarrow 2_g$	778.82	4.24	0.71%	NDS
$2_\gamma \rightarrow 4_g$	520.95	0.0172	2.07%	Tm
$2_\gamma \rightarrow 2_g$	705.32	1.000		Tm
$2_\gamma \rightarrow 0_g$	785.89	0.9059	1.05%	Tm

[1] Calculated from differences of adopted [17] level energies.
[2] Normalized (^{166m}Ho decay) to $I_\gamma(810.28) \equiv 80.0$ ($\equiv 58.1/100$ β decays, i.e., $\times 0.726$ [17]) or (^{166}Tm decay) $I_\gamma(705.32) \equiv 1.000$.
[3] NDS(I_γ taken from NDS adopted value [17]); Ho(I_γ extracted from the ^{166m}Ho data; Tm(I_γ extracted from the ^{166}Tm data).
[4] Normalized through $I_\gamma(691.25) \equiv 1.85$ (^{166m}Ho decay).
[5] Average of Ho and Tm.

CHAPTER III

ROTOR MODELS AND BAND MIXING

The rotor model has been extremely successful at describing deformed even-even nuclei since its introduction by A. Bohr [3]. The rotor can provide insightful correlations to transition strengths and selection rules, and it can be solved algebraically.

The angular momentum structure of a collective nuclear state is depicted in Figure 13. In its simplest form a near symmetric prolate deformed nucleus is assumed to execute adiabatic rotations (separation of internal degrees of freedom from collective degrees of freedom). From this view, which is in agreement with the systematics of even-even nuclei,

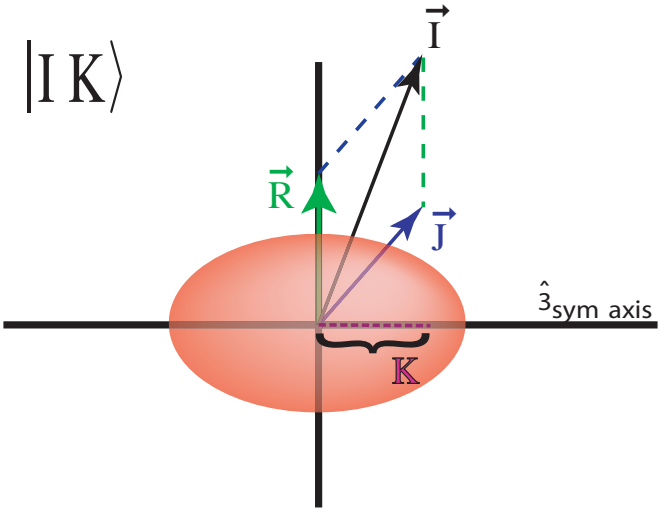

Figure 13: Representation of a deformed nucleus and its angular momentum and projection in the body frame. This is the basis for the angular component in the nuclear state.

the nucleus has a 0^+ angular momentum and even parity ground state and excited integer spin states. The excited states can be grouped into a "ground band" with spin projection in the body frame of $K^\pi = 0^+$, and a "gamma band" with spin projection of $K^\pi = 2^+$ (note that for $K^\pi = 2^+$, $I^\pi \geq 2^+$). Positive and negative body projections must be used to

symmetrize the state and preserve parity. The ground band ($K^\pi = 0^+$) has only even spin states ($I^\pi = 0^+, 2^+, 4^+, 6^+, \ldots$) since an odd spin state produces an asymmetric state for even integer body projections. The term "near symmetric" is used since a true symmetric deformation would not allow collective rotations about the symmetry axis.

3.1 First Order Rotor Basis State, Hamiltonian, and Quadrupole Operator

The assumption of a near symmetric prolate deformation gives a simple and useful place to start. In this limit the states,

$$|IK\rangle_\diamondsuit = \frac{1}{\sqrt{2}}\left(|IK\rangle + (-1)^{I+K}|I,-K\rangle\right), \tag{4}$$

$$|I0\rangle_\diamondsuit = |I0\rangle, \tag{5}$$

are pure (unmixed); and the Hamiltonian,

$$\hat{H} = A\hat{I}^2 + F\hat{I}_3^2, \tag{6}$$

is diagonal. The energy eigenvalues are given by

$$\langle IK|\hat{H}|IK\rangle = AI(I+1) + FK^2 \tag{7}$$

and therefore,

$${}_\diamondsuit\langle IK|\hat{H}|IK\rangle_\diamondsuit = AI(I+1) + FK^2. \tag{8}$$

Following Bohr and Mottelson the $E2$ quadrupole operator [7] is defined in the following way:

$$\begin{aligned}\hat{T}^{(2)} &= \hat{T}(E2) \\ &= \left[\cos\gamma\,\hat{T}_0^{(2)} + \frac{\sin\gamma}{\sqrt{2}}(\hat{T}_{+2}^{(2)} + \hat{T}_{-2}^{(2)})\right](e\cdot b),\end{aligned} \tag{9}$$

where

$$\hat{T}_q^{(2)} \equiv \sqrt{\frac{5}{16\pi}}Q_0 D_{qm}^2 \tag{10}$$

and

$$\beta = Q_0\frac{\sqrt{5\pi}}{3ZR^2}. \tag{11}$$

The term D^2_{qm} represents a Wigner-D function (which carries both body and lab frame indices). The structure of the operator reflects the degree of "diagonal" ($\hat{T}^{(2)}_0$, $\Delta K = 0$) and "off-diagonal" ($\hat{T}^{(2)}_{\pm 2}$, $\Delta K = \pm 2$) $E2$ quadrupole deformation. The quadrupole asymmetry is controlled by the parameter, γ; and the overall strength of the electric quadrupole deformation is scaled by $\sqrt{\frac{5}{16\pi}}Q_0$ (where, cf. Equation (11), β is the shape deformation strength). Diagonal quadrupole deformations preserve the symmetry axis and off-diagonal quadrupole deformations either break or change the symmetry axis. Figure 14 shows images of quadrupole deformed shapes and the symmetries of γ. While a one-to-one correspondence can be drawn [8] between the asymmetry of the $E2$ quadrupole tensor and the inertia tensor of the Hamiltonian, no such assumption is made here (this point is amplified later).

The Wigner-Eckart theorem, APPENDIX B, provides a powerful way to evaluate the $E2$ quadrupole operator matrix elements. The reduced $E2$ transition probability of gamma-ray decay (cf. Equation (72))

$$B(E2;\, I_\mathrm{i}K_\mathrm{i} \to I_\mathrm{f}K_\mathrm{f}) = \frac{|\langle I_\mathrm{f}K_\mathrm{f}||\hat{T}^{(2)}||I_\mathrm{i}K_\mathrm{i}\rangle|^2}{2I_\mathrm{i}+1} \tag{12}$$

is related to the square of the reduced $E2$ matrix element

$$\langle \alpha' I'K'||\hat{T}^{(2)}_{\pm q}||\alpha IK\rangle = Q_0\sqrt{\frac{5}{16\pi}}\sqrt{2I+1}\langle IK;2,\pm q|I'K'\rangle \tag{13}$$

given by the Wigner-Eckart theorem. The consequence of this is that transition probability ratios within bands are determined by ratios of Clebsch-Gordan coefficients, e.g.,

$$\frac{B(E2;\, I=4,\, K=0 \to I=2,\, K=0)}{B(E2;\, I=2,\, K=0 \to I=0,\, K=0)} = \left(\frac{\langle 40;20|20\rangle}{\langle 20;20|00\rangle}\right)^2 = \frac{10}{7} = 1.429. \tag{14}$$

These are the so-called Alaga rules [7]. Ratios of interband transitions to intraband transitions are determined by ratios of Clebsch-Gordan coefficients scaled by $\tan^2\gamma$, e.g.,

$$\frac{B(E2;\, I=2,\, K=2 \to I=0,\, K=0)}{B(E2;\, I=2,\, K=0 \to I=0,\, K=0)} = \left(\frac{\sin\gamma\langle 22;2,-2|00\rangle}{\cos\gamma\langle 20;20|00\rangle}\right)^2 = \tan^2\gamma. \tag{15}$$

The first order $E2$ quadrupole deformation and asymmetry for a near symmetric rotor is represented in Figure 15.

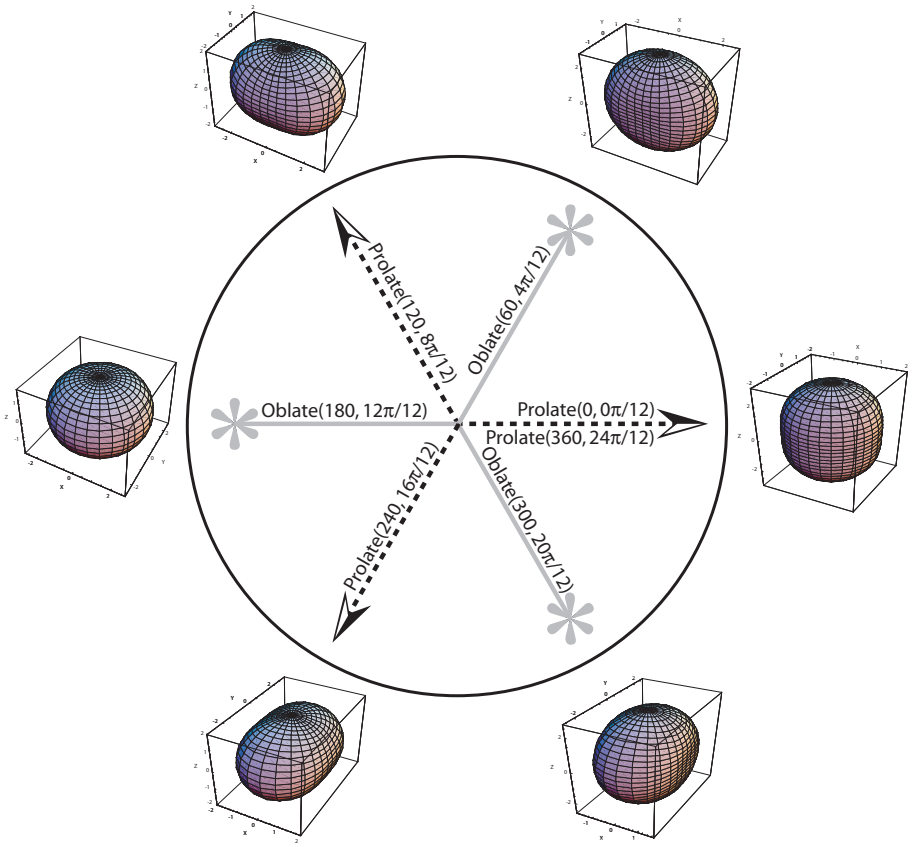

Figure 14: Quadrupole deformations on a sphere by varying the asymmetry angle (γ) with the strength of the deformation (β) held constant. There is a three-fold redundancy of prolate and oblate shapes and a six-fold redundancy of triaxial shapes. The angular basis (e.g., definition of symmetry axis and its magnitude) dictates the region of the asymmetry used. More shapes are given in APPENDIX C.

The trace of the $E2$ quadrupole operator, Equation (9), is independent of the basis used. Therefore, the trace satisfies

$$\begin{aligned} Tr\{\hat{T}^{(2)}\}_I &= Q_0 \cos\gamma \sqrt{\frac{5}{16\pi}} \sqrt{2I+1} \times \{ \\ &\langle I0;20|I0\rangle + \langle I2;20|I2\rangle + \langle I4;20|I4\rangle + \cdots \} \\ &= 0, \end{aligned} \tag{16}$$

independent of any Hamiltonian defined. If the experimental trace or sum of diagonal matrix elements for a given I do not equal zero, it would suggest that the full space was not summed (e.g., there are K-admixtures from outside the model space).

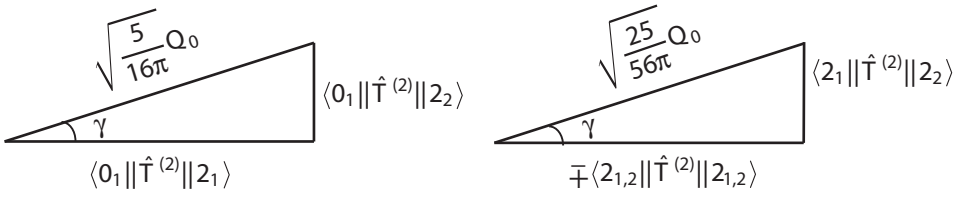

Figure 15: "Pythagoras" representation of first order $E2$ quadrupole deformation and asymmetry.

3.2 Mikhailov Theory

Mikhailov theory was first introduced by V. M. Mikhailov [6]. It provides a simple way to linearly fit interband ($\Delta K = \pm 2$) transitions. Bohr and Mottelson outline its derivation and use in detail (see pp. 145-175 in Bohr and Mottelson Vol. 2 [7]).

Mikhailov theory [7] is defined by the linear relation

$$\frac{\sqrt{B(E2;\, I_\mathrm{i} \to I_\mathrm{f})}}{\langle I_\mathrm{i} K_\mathrm{i}; 2-2 | I_\mathrm{f} K_\mathrm{f}\rangle} = \sqrt{1+\delta_{K_\mathrm{f}0}}\,[M_1 - M_2\Delta], \quad M_2 < 0 \tag{17}$$

$$\Delta \equiv [I_\mathrm{f}(I_\mathrm{f}+1) - I_\mathrm{i}(I_\mathrm{i}+1)], \tag{18}$$

where M_2 is defined to be negative to match with Bohr and Mottelson [7] parameters M_1 and M_2(they give the conjugate $B(E2)$ and Clebsch-Gordan coefficient from what is used here). The Mikhailov relation provides a convenient method for relating transition strengths between bands and is accurate for nuclei that are near symmetric and slightly asymmetric. However, high-spin (large I) states and nuclei that are strongly asymmetric deviate from the simple linear relation.

The intrinsic matrix element of the off-diagonal ($\Delta K = \pm 2$) $E2$ quadrupole deformation [7] is given by

$$\sqrt{\frac{5}{16\pi}} Q_0 \frac{\sin\gamma}{\sqrt{2}} = M_1 + 4(K_\mathrm{i} - 1)M_2 \tag{19}$$

and the off-diagonal mixing strength [7] between bands of an asymmetric rotor Hamiltonian is given by

$$G = \sqrt{\frac{8\pi}{15}} \frac{M_2 \Delta E_{I=2}}{Q_0 \cos\gamma}, \quad G < 0. \tag{20}$$

These two relations provide a connection between the Mikhailov representation and the general asymmetric rotor model.

The usefulness of Mikhailov theory is exploited in its ability to correlate multiple $I_\mathrm{i} \rightarrow I_\mathrm{f}$ transitions to $\Delta = 0$. The correlation to $\Delta = 0$ condenses multiple $\Delta K = \pm 2$ transitions to a single reference and provides an averaged intrinsic $E2$ matrix element, Equation (19), and intrinsic band mixing strength, Equation (20). This is especially useful when only relative $B(E2)$ or intensity data are available since different decay branches out of a given state can be normalized through the $\Delta = 0$ points. A well known Mikhailov plot of ^{166}Er is shown in Figure 16 and is from Bohr and Mottelson [7].

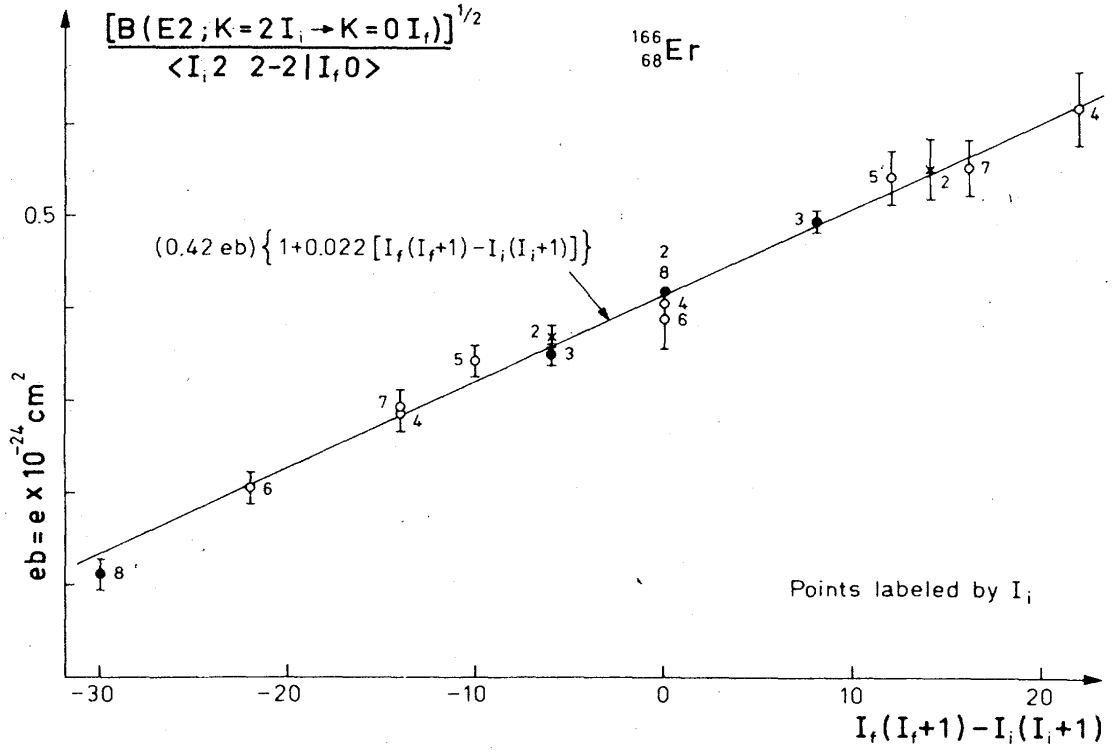

Figure 16: Mikhailov plot of ^{166}Er from Bohr and Mottelson [7]

Higher-order terms in Mikhailov theory were explored by the Baker-Hausdorff expansion technique outlined by Bohr and Mottelson [7], yielding

$$\frac{\sqrt{B(E2;\, I_\mathrm{i} \rightarrow I_\mathrm{f})}}{\langle I_\mathrm{i} 22 - 2 | I_\mathrm{f} 0 \rangle} = m_0 + m_1 \Delta + m_2 \Delta^2 + m_3 \Delta^3, \quad m_0 \sim \sqrt{2} M_1,\, m_1 \sim -\sqrt{2} M_2. \qquad (21)$$

The unitary transformation that diagonalizes the Hamiltonian is expanded with the Baker-Hausdorff lemma. The first commutator term in the expansion provides the Mikhailov linear relation (e.g., linear term and constant term). The second commutator term provides a quadratic term exactly and lower-order terms. The third commutator term provides a cubic term exactly and lower-order terms. The lower order correction terms (from the second and third commutator) are difficult to simplify (complex expansion of commutator relations). However, the lower-order corrections are too weak in magnitude to significantly alter the constant and linear Mikhailov term. This offers insight into the manner in which the linear relation should break down.

3.3 Triaxial Rotor Model

The triaxial rotor model was introduced for the description of nuclear data by Davydov and Filippov [8]. Historically, irrotational flow has been used to describe the inertia tensor. We make no assumptions about the inertia tensor and leave it general.

The general Hamiltonian of an asymmetric, triaxial rotor [20] is

$$H = A_1\hat{I}_1^2 + A_2\hat{I}_2^2 + A_3\hat{I}_3^2, \tag{22}$$

where A_1, A_2, and A_3 are related to $\mathcal{J}_1, \mathcal{J}_2, \mathcal{J}_3$ by $A_1 = 1/(2\mathcal{J}_1)$, etc. In this form nothing is assumed other than that there are three unique moments of inertia.

New parameters are formed, [20], by rewriting the Hamiltonian to use standard angular momentum theory and are as follows

$$\begin{aligned} 0 < A &= \frac{1}{2}(A_1 + A_2), \\ 0 < F &= A_3 - A, \\ 0 > G &= \frac{1}{4}(A_1 - A_2). \end{aligned} \tag{23}$$

The transformed Hamiltonian,

$$\hat{H} = A\hat{I}^2 + F\hat{I}_3^2 + G(\hat{I}_+^2 + \hat{I}_-^2), \tag{24}$$

allows direct use of angular momentum algebra. In the body frame, $[\hat{I}_1, \hat{I}_2] = -i\hat{I}_3$, $[\hat{I}_3, \hat{I}_\pm] = \mp\hat{I}_\pm$, and $[\hat{I}_+, \hat{I}_-] = -2\hat{I}_3$, [7]. The body-frame commutator relations are opposite to the lab frame commutator relations. The lab frame angular momentum operators are infinitesimal generators of right rotations while the body frame angular momentum operators are infinitesimal generators of left rotations.

The $E2$ quadrupole operator used here takes the same form in which it was originally defined, Equation (9).

The asymmetric or triaxial rotor Hamiltonian and eigenstates are outlined below in general form. The diagonal and off-diagonal matrix elements of the Hamiltonian are ($\hbar = 1$)

$$\hat{H}_0 = A\hat{I}^2 + F\hat{I}_3^2, \tag{25}$$

$$\langle IK|\hat{H}_0|IK\rangle = AI(I+1) + FK^2, \tag{26}$$

$$\hat{H}_1 = G(\hat{I}_+^2 + \hat{I}_-^2), \tag{27}$$

$$\langle I, K \pm 2|\hat{H}_1|IK\rangle = G\sqrt{(I \mp K)(I \pm K + 1)(I \mp K - 1)(I \pm K + 2)}, \tag{28}$$

and therefore,

$$_\diamondsuit\langle I, K \pm 2|\hat{H}_1|IK\rangle_\diamondsuit = G\sqrt{(I \mp K)(I \pm K + 1)(I \mp K - 1)(I \pm K + 2)} \tag{29}$$

$$\times \sqrt{1 + \delta_{K\pm 2,\,0}}\sqrt{1 + \delta_{K,\,0}}. \tag{30}$$

The Hamiltonian for $I = 2$ can be written as

$$H(2) = \begin{pmatrix} 6A & 4\sqrt{3}G \\ 4\sqrt{3}G & 6A + 4F \end{pmatrix} \tag{31}$$

and transformed to

$$H(2) = 6A \begin{pmatrix} 1 & 0 \\ 0 & 1 \end{pmatrix} + G \begin{pmatrix} 0 & 4\sqrt{3} \\ 4\sqrt{3} & 4F/G \end{pmatrix} \tag{32}$$

for establishing the eigenvectors and energy spacing (the two-by-two $I = 2$ space provides exact fitting of the model parameters, discussed later in CHAPTER 3.3.1). The Hamiltonian

for $I = 4$ can be written as

$$H(4) = \begin{pmatrix} 20A & 12\sqrt{5}G & 0 \\ 12\sqrt{5}G & 20A + 4F & 4\sqrt{7}G \\ 0 & 4\sqrt{7}G & 20A + 16F \end{pmatrix} \tag{33}$$

and transformed to

$$H(4) = 20A \begin{pmatrix} 1 & 0 & 0 \\ 0 & 1 & 0 \\ 0 & 0 & 1 \end{pmatrix} + G \begin{pmatrix} 0 & 12\sqrt{5} & 0 \\ 12\sqrt{5} & 4F/G & 4\sqrt{7} \\ 0 & 4\sqrt{7} & 16F/G \end{pmatrix} \tag{34}$$

for determining the eigenvectors and energy spacing. The process can be continued for other I (e.g., $I = 3$ (dimension 1x1), $I = 5$ (dimension 2x2), $I = 6$ (dimension 4x4), etc...). In general the regular or transformed Hamiltonian can be diagonalized (e.g., numerically with computer) to provide the energy eigenvalues and mixed state amplitudes. The mixed states will be superpositions of the symmetrized states in Equation (4) and Equation (5).

3.3.1 Triaxial Two-Band Prescription

A useful two-by-two subspace approximation is made here

$$H(I) = \begin{pmatrix} AI(I+1) & G\sqrt{2I(I+1)(I-1)(I+2)} \\ G\sqrt{2I(I+1)(I-1)(I+2)} & AI(I+1) + 4F \end{pmatrix}, \tag{35}$$

since $|G| << F$ and $16F > 4F$ isolate the ground ($K = 0$) and gamma ($K = 2$) bands from others. The real value of the approximation is its ability to produce general solutions that are analytical and cross-compatible with different values of angular momentum I.

The mixed states and energy eigenvalues for the ground and gamma band are

$$|I_g\rangle = \cos\Gamma_I |I0\rangle_\diamond - \sin\Gamma_I |I2\rangle_\diamond, \tag{36}$$

$$E_g(I) = AI(I+1) + 2F - \sqrt{4F^2 + 2G^2 I(I+1)(I-1)(I+2)}, \tag{37}$$

$$|I_\gamma\rangle = \sin\Gamma_I |I0\rangle_\diamond + \cos\Gamma_I |I2\rangle_\diamond, \tag{38}$$

$$E_\gamma(I) = AI(I+1) + 2F + \sqrt{4F^2 + 2G^2 I(I+1)(I-1)(I+2)}, \tag{39}$$

where the mixed states are represented by a unitary transformation through an angle Γ_I that diagonalizes the Hamiltonian. The mixing angle for $I = 2$ is related to the Hamiltonian by

$$\tan 2\Gamma_2 = 2\sqrt{3}\frac{G}{F}, \tag{40}$$

where $G < 0$ and $\Gamma_2 < 0$. The remaining mixing angles are related to Γ_2 by

$$\tan(2\Gamma_I) = \sqrt{\frac{(I-1)I(I+1)(I+2)}{24}}\tan(2\Gamma_2). \tag{41}$$

The mixing angle, Γ_2, can be related to the Mikhailov mixing strength, Equation (20), by setting $\Delta E_{I=2} = F$ to get

$$\tan 2\Gamma_2 = \sqrt{\frac{32\pi}{5}}\frac{M_2}{Q_0\cos\gamma}. \tag{42}$$

The reduced $E2$ matrix element and trace of the $E2$ quadrupole operator are given below in general form for the $K = 0$, 2 subspace

$$|I_i\rangle = c_1|I_i0\rangle_\diamond + c_2|I_i2\rangle_\diamond, \tag{43}$$

$$|I_f\rangle = c_3|I_f0\rangle_\diamond + c_4|I_f2\rangle_\diamond, \tag{44}$$

$$\begin{aligned}\langle I_f||\hat{T}^{(2)}||I_i\rangle = Q_0\sqrt{\frac{5}{16\pi}}\sqrt{2I_i+1}\times\{ \\ + c_1c_3\cos\gamma\langle I_i0;20|I_f0\rangle \\ + c_1c_4\sin\gamma\langle I_i2;2,-2|I_f0\rangle \\ + c_2c_3\sin\gamma\langle I_i0;22|I_f2\rangle \\ + c_2c_4\cos\gamma\langle I_i2;20|I_f2\rangle\ \}\,,\end{aligned} \tag{45}$$

$$\begin{aligned}Tr\{\hat{T}^{(2)}\}_I = Q_0\cos\gamma\sqrt{\frac{5}{16\pi}}\sqrt{2I+1}\times\{ \\ \langle I0;20|I0\rangle + \langle I2;20|I2\rangle\ \}\,.\end{aligned} \tag{46}$$

This provides a quick and powerful tool to analyze ground and gamma bands of even-even nuclei. Any property of the ground plus gamma band can be computed with a hand calculator, a set of model parameters (discussed below), and a table of Clebsch-Gordan coefficients. See APPENDIX A for expressions and tables of Clebsch-Gordan coefficients.

Starting parameters for the model can be solved exactly in the $I = 0,\ 2$ space, Figure 17. The parameters are solved in the following way

$$A = \frac{1}{6}E(2_1^+), \tag{47}$$

$$F = \frac{1}{4}[E(2_2^+) - E(2_1^+)]. \quad F >> G \tag{48}$$

$$\tag{49}$$

The $I = 2$ energies alone are unable to provide a value for G. Band separation energies

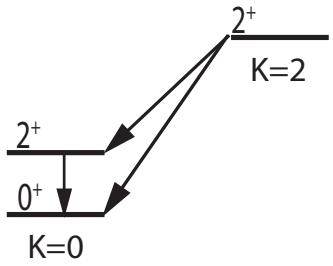

Figure 17: Level diagram ($I \leq 2$) of an even-even nucleus. The $I = 0, 2$ space of the model is exactly solvable and able to determine all the model parameters.

can be used to estimate G but an alternative approach is used in fitting (discussed below) to the reduced $E2$ transition matrix elements $\langle 0_1||\hat{T}^{(2)}||2_2\rangle$ and $\langle 2_1||\hat{T}^{(2)}||2_2\rangle$. This solves it exactly and only with the use of the $I = 0,\ 2$ space.

The reduced $E2$ matrix elements and quadrupole moments for the $I = 0,\ 2$ space are

$$\langle 0_1||\hat{T}^{(2)}||2_1\rangle = \sqrt{\frac{5}{16\pi}}Q_0\cos(\gamma + \Gamma_2), \tag{50}$$

$$\langle 0_1||\hat{T}^{(2)}||2_2\rangle = \sqrt{\frac{5}{16\pi}}Q_0\sin(\gamma + \Gamma_2), \tag{51}$$

$$\langle 2_1||\hat{T}^{(2)}||2_2\rangle = \sqrt{\frac{25}{56\pi}}Q_0\sin(\gamma - 2\Gamma_2), \tag{52}$$

$$\begin{aligned}\langle 2_1||\hat{T}^{(2)}||2_1\rangle &= -\sqrt{\frac{25}{56\pi}}Q_0\cos(\gamma - 2\Gamma_2) \\ &= -\langle 2_2||\hat{T}^{(2)}||2_2\rangle,\end{aligned} \tag{53}$$

$$Q(2_1^+) = -\frac{2}{7}Q_0\cos(\gamma - 2\Gamma_2) = -Q(2_2^+). \tag{54}$$

and the $E2$ sensitive parameters can be solved (using the most commonly occurring and accurately known experimental data)

$$Q_0 = \sqrt{\frac{16\pi}{5}} \sqrt{\langle 0_1||\hat{T}^{(2)}||2_1\rangle^2 + \langle 0_1||\hat{T}^{(2)}||2_2\rangle^2}, \tag{55}$$

$$\gamma + \Gamma_2 = \tan^{-1}\left(\frac{\langle 0_1||\hat{T}^{(2)}||2_2\rangle}{\langle 0_1||\hat{T}^{(2)}||2_1\rangle}\right), \tag{56}$$

$$\gamma - 2\Gamma_2 = \sin^{-1}\left(\sqrt{\frac{56\pi}{25}}\frac{\langle 2_1||\hat{T}^{(2)}||2_2\rangle}{Q_0}\right). \tag{57}$$

The deduction of Γ_2 from $E2$ data can then provide an estimate for G in the Hamiltonian by using (cf. Equation (40))

$$G = \frac{F}{2\sqrt{3}}\tan(2\Gamma_2). \tag{58}$$

The $E2$ sensitive parameters and matrix elements of the $I = 0$, 2 space are summarized in Figure 18.

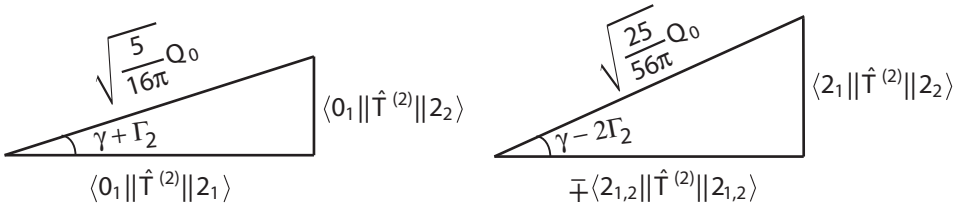

Figure 18: "Pythagoras" representation of model parameters and $I = 0$, 2 subspace. This is useful for qualitatively and quantitatively correlating the reduced $E2$ matrix element strengths and shape asymmetries (e.g., possible angle components). Since $\langle 0_1||\hat{T}^{(2)}||2_1\rangle$ is always the most precisely known reduced $E2$ matrix element and since it is controlled by the smallest angle (Γ_2 is negative), Q_0 is always extracted from the left triangle relation.

The matrix elements for the $I = 0$, 2 space are the only single-term expressions other than those for odd-spin states in the gamma band. The odd spin states in the two-by-two approximation are pure or unmixed which gives rise to their simple relations. However, the 3_1 state is important since there is only one $I = 3$ state in the full triaxial rotor model and

it is exact already in the two-by-two prescription. Note

$$\langle 2_1||\hat{T}^{(2)}||3_1\rangle = Q_0\sqrt{7}\sqrt{\frac{5}{16\pi}}\sqrt{\frac{5}{14}}\sin(\gamma+\Gamma_2), \tag{59}$$

$$\langle 2_2||\hat{T}^{(2)}||3_1\rangle = -Q_0\sqrt{7}\sqrt{\frac{5}{16\pi}}\sqrt{\frac{5}{14}}\cos(\gamma+\Gamma_2), \tag{60}$$

$$\langle 3_1||\hat{T}^{(2)}||3_1\rangle = 0, \tag{61}$$

i.e., these relations also possess "triangle" representations. The reduced diagonal $E2$ matrix element of 3_1 is zero. This follows from the trace rule (cf. Equation (46)) because it is the only term in the sum. In this regard an $I = 3$ state behaves like an $I = 0$ state (e.g., both are of dimension 1x1).

Unfortunately, few data exist for 3_1 states. If accurate data could be obtained for transitions involving 3_1 states, it would provide a powerful aid in understanding nuclear collectivity. Many expressions and ratios of reduced $E2$ matrix elements are in APPENDIX A, but one specific ratio of use is given here, viz.

$$\frac{\langle 2_1||\hat{T}^{(2)}||3_1\rangle}{\langle 0_1||\hat{T}^{(2)}||2_2\rangle} = \sqrt{\frac{5}{2}}, \tag{62}$$

and it is exact. A breakdown in this relationship would indicate additional $K = 0$ and or $K = 2$ admixtures from outside the model space (i.e., intruder bands [21]).

For relatively large values of Γ_2 in Equation (41), the mixing saturates at $\Gamma_I = 45°$. An Alaga-like relation (cf. Equation 14)) for interband transitions of high spin or saturated mixing is the result and follows, viz.

$$\frac{B(E2; I_\mathrm{i}2 \to I_\mathrm{f}0)}{B(E2; I'_\mathrm{i}2 \to I'_\mathrm{f}0)} = \left(\frac{\langle I_\mathrm{i}2; 20|I_\mathrm{f}2\rangle - \langle I_\mathrm{i}0; 20|I_\mathrm{f}0\rangle}{\langle I'_\mathrm{i}2; 20|I'_\mathrm{f}2\rangle - \langle I'_\mathrm{i}0; 20|I'_\mathrm{f}0\rangle}\right)^2. \tag{63}$$

This sets a limit that interband transition ratios can have.

CHAPTER IV

MODEL TEST

In this Chapter the model details presented in CHAPTER 3 are tested. These tests include a global fit of the basic triaxial rotor model to systematic data obtained from the Evaluated Nuclear Structure Data File (ENSDF, [11]); a fit to precision data (described in CHAPTER 2) for ^{166}Er; and a detailed fit to local systematic data [22] in ^{186,188,190,192}Os.

4.1 ENSDF Systematics

The primary goal of the global fit was to determine how widely applicable the triaxial rotor is to data for even-even collective nuclei. A primary outcome of this was the recognition that irrotational moments of inertia fail. Irrotational moments of inertia have, prior to this work, always been used. We first give details of irrotational moments of inertia in terms of the model parameters used here.

Irrotational moments of inertia were introduced by Davydov and Filippov [8] following the lead of A. Bohr in his original paper [3]. It was extensively developed later, [9]. The Davydov and Filippov model directly correlates the inertia tensor to the $E2$ quadrupole tensor Equation (9) and Equation (11), via the parameters β and γ, by

$$\mathcal{J}_k = 4B\beta^2 \sin^2\left(\gamma - k\frac{2\pi}{3}\right),\ k = 1, 2, 3, \tag{64}$$

where B is the irrotational flow mass parameter and the dependence on γ gives the ratios of the components of the inertia tensor according to irrotational flow [20]. These irrotational moments, with the use of Equation (23), reduce to the following model parameters and

expressions

$$A = \frac{1}{4B\beta^2}\frac{1+\frac{1}{2}\cos 2\gamma}{(\frac{1}{2}+\cos 2\gamma)^2}, \tag{65}$$

$$F = \frac{3}{8B\beta^2\sin^2 3\gamma}(\cos 4\gamma + 2\cos 2\gamma), \tag{66}$$

$$G = \frac{\sqrt{3}}{16B\beta^2\sin^2 3\gamma}(\sin 4\gamma - 2\sin 2\gamma), \tag{67}$$

$$\Gamma_{irrot} = -\frac{1}{2}\cos^{-1}\left(\frac{\cos 4\gamma + 2\cos 2\gamma}{\sqrt{9-8\sin^2 3\gamma}}\right), \tag{68}$$

$$\frac{E(2_2^+)}{E(2_1^+)} = \frac{3+\sqrt{9-8\sin^2 3\gamma}}{3-\sqrt{9-8\sin^2 3\gamma}}, \tag{69}$$

$$\frac{B(E2;2_2^+\rightarrow 0_1^+)}{B(E2;2_1^+\rightarrow 0_1^+)} = \frac{\sqrt{9-8\sin^2 3\gamma}-3+2\sin^2 3\gamma}{\sqrt{9-8\sin^2 3\gamma}+3-2\sin^2 3\gamma}. \tag{70}$$

Irrotational flow is an idealization of nuclear rotation but it is more realistic than rigid flow. In comparison, the present triaxial rotor model assumes the electric quadrupole tensor and the inertia tensor are independently parameterized. Fitting to data reveals that these parameters are strongly correlated.

Figure 19 shows predicted irrotational $B(E2)$ ratios vs. Energy ratios, Equation (69) and Equation (70), and experimental even-even nuclear data for $Z > 28$. The Os isotopes have $B(E2)$ ratios in the vicinity of 0.09. The irrotational assumption achieves a qualitative global fit.

A dramatic limitation of irrotational flow moments of inertia is revealed in Figure 19. The $B(E2)$ ratio obtained using irrotational moments cannot exceed 0.0718. For example, the Osmium nuclei lie entirely outside of the possible range of $B(E2)$ values. This is simply explained by the model introduced here. Table 3 shows that $\gamma + \Gamma_{irrot}$ has a maximum possible value of 15.00° for $\gamma = 20.00^\circ$. From the equation

$$\frac{B(E2;2_2^+\rightarrow 0_1^+)}{B(E2;2_1^+\rightarrow 0_1^+)} = \tan^2(\gamma+\Gamma_2), \tag{71}$$

it is seen that $\tan^2(15.00^\circ) = 0.0718$ explains this limit.

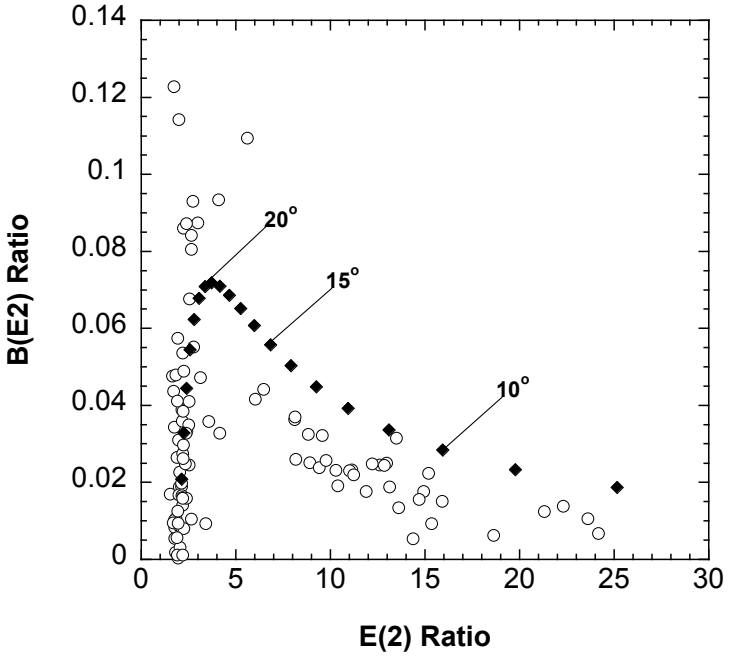

Figure 19: $B(E2;\, 2_2 \rightarrow 0_1)/B(E2;\, 2_1 \rightarrow 0_1)$ vs $E(2_2)/E(2_1)$ systematics from ENSDF database [11] of even-even nuclei $Z > 28$ (excluding closed shell nuclei and ^{84}Kr with 0.232 for display reasons) and retrieved by using GTNDSE [12]. The dark diamond points are from the irrotational theory predictions, Equation (69) and Equation (70).

Table 3 also shows another severe limitation to the use of irrotational flow moments of inertia. For $\gamma = 30.00^\circ$, $\Gamma_{irrot} = -30.00^\circ$ and this results in $\langle 2_1||\hat{T}^{(2)}||2_1\rangle = 0$ (because of its $\cos(\gamma - 2\Gamma)$ dependence, Equation (53)) and $\langle 0_1||\hat{T}^{(2)}||2_2\rangle = 0$ (because of its $\sin(\gamma + \Gamma)$ dependence, Equation (51)). There is only one nucleus known (^{196}Pt) for which $\langle 0_1||\hat{T}^{(2)}||2_2\rangle$ is consistent with zero. There are no known nuclei with $\langle 2_1||\hat{T}^{(2)}||2_1\rangle = 0$, i.e, all known nuclei have non-zero values for this matrix element.

While the use of irrotational flow moments is demonstrated by the present comparisons to fail, the model introduced here requires one additional parameter to describe the global data. We note that the qualitative trend exhibited by the data shown in Figure 19 is the same as that for irrotational flow. This would be worth exploring further.

A few experimental moments of inertia (for nuclei ranging from very symmetric to triaxial) are tested against irrotational moments of inertia in Table 4. The ratios between irrotational moments (fitted to the experimental A_1 moment) and experimental moments are not in

Table 3: Values of Γ_{irrot} and $\gamma + \Gamma_{irrot}$ as a function of γ, according to Equation(68), in the vicinity of $\gamma = 20°$.

γ	Γ_{irrot}	$\gamma + \Gamma_{irrot}$	$\gamma - 2\Gamma_{irrot}$
19.0°	−4.085°	14.915°	27.170°
19.9°	−4.90091°	14.99909°	29.70182°
20.0°	−5.00000°	15.00000°	30.00000°
20.1°	−5.10090°	14.99910°	30.30180°
21.0°	−6.096°	14.904°	33.192°
24.0°	−10.866°	13.134°	45.732°
27.0°	−18.793°	8.207°	64.586°
30.0°	−30.000°	0.000°	90.000°

agreement. Irrotational flow over-predicts the strength of the inertia moments. Rigid moments would over-shoot the prediction even more so. The triaxial rotor model introduced here is flexible enough to accommodate these experimental values.

Table 4: Fitted rotational parameters and their ratios with respect to irrotational parameters, Equation(64), for selected nuclei.

Nucleus	$A_1^{\rm expt}$	$A_2^{\rm expt}$	$A_3^{\rm expt}$	$\frac{A_2^{\rm expt}}{A_2^{\rm irrot}}$ [1]	$\frac{A_3^{\rm expt}}{A_3^{\rm irrot}}$ [1]
^{186}Os	17.5	28.1	181	0.918	0.614
^{188}Os	20.2	31.4	145	0.768	0.633
^{166}Er	11.4	15.4	189	0.885	0.610
^{172}Yb	11.9	14.3	360	0.841	0.798
^{184}W	16.4	20.6	217	0.821	0.485

[1] For $A_1^{\rm irrot} \equiv A_1^{\rm expt}$

4.2 Erbium-166

The precision γ-ray intensity data for ^{166}Er from Table 2 is used as a precision test of the present rotor models. Specifically, the data are analyzed with Mikhailov theory and the triaxial two-band model. The goal is to learn how well nuclei can rotate and how the rotational picture fails.

Gamma-ray intensities are a direct measure of nuclear transition probabilities. Reduced transition probabilities are related to γ-ray intensities by

$$B(E2;\, I_i \to I_f) \propto \frac{\text{Intensity}}{(\text{Energy})^5} = \frac{I_\gamma}{(E_\gamma)^5}. \tag{72}$$

This is the essential step for comparing gamma-ray data to theoretical models. The relationship of $B(E2)$'s to theory is via (cf. Equation (12))

$$B(E2;\, I_{\rm i}K_{\rm i} \rightarrow I_{\rm f}K_{\rm f}) = \frac{|\langle I_{\rm f}K_{\rm f}||\hat{T}^{(2)}||I_{\rm i}K_{\rm i}\rangle|^2}{2I_{\rm i}+1}. \tag{73}$$

The essential result emerging from Mikhailov theory is (cf. Equation (21))

$$\frac{\sqrt{B(E2;\, I_{\rm i} \rightarrow I_{\rm f})}}{\langle I_{\rm i}22-2|I_{\rm f}0\rangle} = m_0 + m_1\Delta + m_2\Delta^2 + m_3\Delta^3. \tag{74}$$

This permits relative $B(E2)$ data to be plotted in the manner shown in Figure 16. To convert the data in Table 2 into a plot such as shown in Figure 16, one first establishes the $\Delta = 0$ point.

The Mikhailov value for $2_\gamma \rightarrow 0_g$ is equal to the reduced $E2$ matrix element and it has the most accurate absolute measurement that is relevant to the study. The Mikhailov $2_\gamma \rightarrow 0_g$, $\Delta = -6$ point is normalized to an average $2_\gamma \rightarrow 0_g$ reduced matrix element, Table 5, of 0.373 ± 0.009 e·b. The normalization sets the $\Delta = 0$ value for $2_\gamma \rightarrow 2_g$. The intrinsic quadrupole strength, Q_0^γ, is then fixed to normalize the $I_i = I_f > 2$ transitions to $\Delta = 0$.

Table 5: Experimental values for $\langle 2_\gamma||\hat{T}(E2)||0_g\rangle$ and the (linearly-weighted) average adopted in the present study.

Process	$\langle 2_\gamma\|\|\hat{T}(E2)\|\|0_g\rangle$ e·b	Source
Coul.	0.372 (19)	[23]
Coul.-RDM	0.331 (17)	[24]
$(p,\, p')$	0.360 (7)	[25]
$(\alpha,\, \alpha'\gamma)$	0.374 (11)	[26]
$(\alpha,\, \alpha')$	0.420 (10)	[27]
$(\alpha,\, \alpha')$	0.374 (8)	[28]
$(\alpha,\, \alpha')$	0.377 (7)	[29]
Coul.	0.366 (12)	[30]
$(d,\, d')$	0.390 (10)	[31]
Avg.	0.373 (9)	

The intrinsic quadrupole strength, $Q_0^\gamma > Q_0^g$, is deduced by initially normalizing $\gamma \rightarrow g$, $\Delta = 0$ transitions to $2_\gamma \rightarrow 2_g$. Values for Q_0^γ are then deduced for each $I_i \rightarrow$ branch by comparing the normalized interband transitions to the intraband transitions through

relative intensities. In extracting Q_0^γ from the intraband transitions, mixing is assumed to have no impact in the intraband strengths (e.g., a near symmetric rotor is used for intraband transitions). An intrinsic quadrupole strength of $Q_0^\gamma = 8.028 \pm 0.108$ is determined for the gamma band ($K = 2$) which can be compared to $Q_0^g = 7.656 \pm 0.033$ [32] for the ground band ($K = 0$).

The Mikhailov plot for the precision study is shown in Figure 20. A cubic polynomial is used in the fit, Equation (21). The error bars for the data are smaller than the points (as drawn) except for $\Delta = 30$ (304 keV, $6_\gamma \rightarrow 8_g$). The extremal points, $\Delta = \pm 30$ ($6_\gamma \rightarrow 8_g$ and

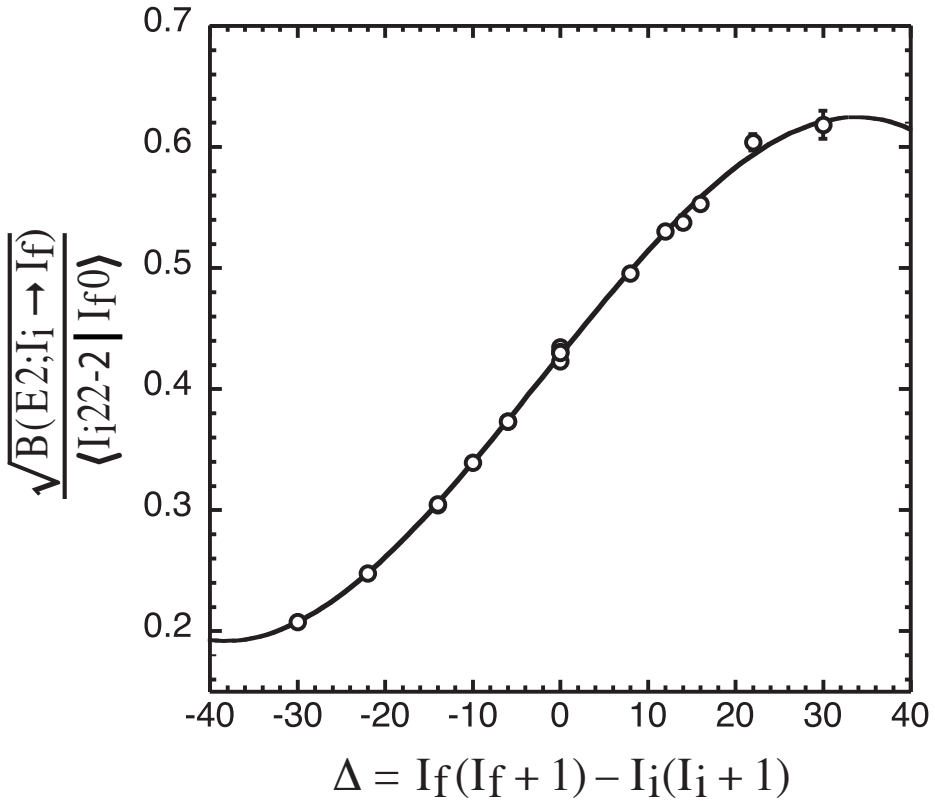

Figure 20: Mikhailov plot for ^{166}Er using the intensities in Table 2 and average $\langle 2_\gamma || \hat{T}(E2) || 0_g \rangle$ in Table 5 for normalization. The cubic fit parameters are $m_0 = 0.427666$ e·b, $m_1 = 8.98016 \times 10^{-3}$ e·b, $m_2 = -1.51023 \times 10^{-5}$ e·b, and $m_3 = -2.31703 \times 10^{-6}$ e·b. The R^2 for the fit is 0.998821. (Note the addition of the $\Delta = 30$ (304 keV, $6_\gamma \rightarrow 8_g$) point and the reduction of the error bars from Figure 16)

$8_\gamma \rightarrow 6_g$), are critical for establishing the cubic term and could not be validated without precision measurements. In the Mikhailov expansion, Equation (21), the quadratic and

cubic terms were estimated to be smaller than the fitted values. The breakdown of the linear Mikhailov theory, Equation (17), is outside the allowed deviations of the expanded model.

The cubic term or breakdown in mixing strength (e.g., the slope represents the mixing strength between bands, Equation (20)) of Figure 20 can be looked at with the triaxial two-band prescription. Triaxial $E2$ model parameters of $Q_0 = 7.748$ e·b, $\gamma = 9.225°$, and $\Gamma = -0.445°$ were determined.

Table 6: Transitions relevant to the present study and the $\sqrt{B(E2;\, I_\mathrm{i} \rightarrow I_\mathrm{f})}/\langle I_\mathrm{i}22 - 2|I_\mathrm{f}0\rangle \equiv \sqrt{B_\mathrm{norm}(E2)}/\langle|\rangle$ e·b adopted.

Transition	Δ	$\langle\|\rangle$	$\sqrt{B_\mathrm{norm}(E2)}/\langle\|\rangle$[1]	Dev. of poly.	$B_\mathrm{2\text{-}band}$	Dev. of 2-band
$8_\gamma \rightarrow 8_g$	0	0.6070	0.4228[2](29)	1.2%	0.06407	−2.7%
$8_\gamma \rightarrow 6_g$	-30	0.2970	0.2074 (18)	−0.1%	0.002660	−29.9%
$7_\gamma \rightarrow 8_g$	16	0.4472	0.5531 (32)	0.9%	0.06185	1.1%
$7_\gamma \rightarrow 6_g$	-14	0.5477	0.3038 (8)	0.5%	0.02829	2.2%
$6_\gamma \rightarrow 8_g$	30	0.1961	0.6181 (115)	0.5%	0.01697	15.5%
$6_\gamma \rightarrow 6_g$	0	0.6030	0.4344[3](12)	−1.6%	0.06494	−5.3%
$6_\gamma \rightarrow 4_g$	-22	0.3129	0.2477 (4)	−0.1%	0.005628	−6.3%
$5_\gamma \rightarrow 6_g$	12	0.4264	0.5303 (18)	−0.2%	0.05020	−1.8%
$5_\gamma \rightarrow 4_g$	-10	0.5641	0.3392 (6)	−0.2%	0.03700	1.1%
$4_\gamma \rightarrow 6_g$	22	0.1741	0.6039 (67)	−1.8%	0.01117	1.1%
$4_\gamma \rightarrow 4_g$	0	0.5922	0.4307[3](23)	−0.7%	0.06330	−2.7%
$4_\gamma \rightarrow 2_g$	-14	0.3450	0.3048 (24)	0.2%	0.01124	1.6%
$3_\gamma \rightarrow 4_g$	8	0.3780	0.4954 (29)	0.4%	0.03469	−1.1%
$3_\gamma \rightarrow 2_g$	-6	0.5976	0.373 (1)	0.2%	0.05018	1.0%
$2_\gamma \rightarrow 4_g$	14	0.1195	0.5376 (56)	1.2%	0.004212	2.1%
$2_\gamma \rightarrow 2_g$	0	0.5345	0.4297[3]	−0.5%	0.05172	−2.0%
$2_\gamma \rightarrow 0_g$	-6	0.4472	0.373 (2)	0.2%	0.02810	1.0%

[1] The numbers in parentheses are uncertainties from ΔI_γ (cf. Table 2) only.

[2] The spread in these $\Delta = 0$ points, i.e., ±1.34%, provides a measure of our uncertainty in the fitted value of $Q_0^\gamma = 8.028$ e·b. Note that their unweighted average is 0.4294 which is close to the independent $\Delta = 0$ value of 0.4297 for $2_\gamma \rightarrow 2_g$.

[3] Note in Table 2 the $2_\gamma \rightarrow 2_g$ intensity is ≡ 1.000, i.e., its uncertainty is incorporated into the $2_\gamma \rightarrow 0_g$ and $2_\gamma \rightarrow 4_g$ intensities.

The summarized Mikhailov and triaxial two-band results for the interband transitions ($\gamma \rightarrow g$) are in Table 6. The cubic polynomial (in Δ) fits the data extremely well (0.62% precision avg.) with the $4_\gamma \rightarrow 6_g$, $\Delta = 22$ point having the largest deviation of -1.8%. The triaxial two-band model agrees with low spin and begins to fail at high spin (note that the cubic fit has 4 $E2$ sensitive parameters where the triaxial rotor has 3). The high spin can be accommodated by reducing the mixing strength Γ_I. This is in agreement with the interpretation that the overly-strong cubic term in the Mikhailov plot is from a breakdown in the mixing strength which acts to reduce the linear relation with increase in I.

Table 7 shows the intraband transitions for the ground and gamma band. The triaxial two-band model is consistent with the result deduced from Mikhailov theory that $Q_\gamma > Q_g$ is inherent as opposed to a mixing effect. Intraband transitions are dictated almost entirely by the intrinsic quadrupole strength Q_0. Therefore, the near constant underestimate ($\sim 10\%$) of the $K = 2$ intraband transitions by the triaxial two-band model reflects the degree to which Q_0^γ deviates from Q_0^g.

Table 7: Intraband $B(E2)$ $\mathrm{e}^2{\cdot}\mathrm{b}^2$

Transition	B_{expt} [1]	$B_{\text{2-band}}$	Dev. of $B_{\text{2-band}}$
$2_g \rightarrow 0_g$	1.166	1.166	0.00%
$4_g \rightarrow 2_g$	1.686	1.671	−0.9%
$6_g \rightarrow 4_g$	1.880	1.852	−1.5%
$8_g \rightarrow 6_g$	1.978	1.955	−1.2%
$10_g \rightarrow 8_g$	2.011	2.029	0.9%
$12_g \rightarrow 10_g$	2.037	2.090	2.6%
$4_\gamma \rightarrow 2_\gamma$	0.7636	0.6893	−9.7%
$5_\gamma \rightarrow 3_\gamma$	1.224	1.111	−9.2%
$6_\gamma \rightarrow 4_\gamma$	1.506	1.351	−10.3%
$7_\gamma \rightarrow 5_\gamma$	1.691	1.534	−9.3%
$8_\gamma \rightarrow 6_\gamma$	1.818	1.614	−11.22%

[1] Ground intraband from NDS [17] except for $2_g \rightarrow 0_g$, which is from [32]. Gamma intraband from relative intensities in present study normalized to Mikhailov extracted absolute $B(E2)$'s .

4.3 Osmium-186,188,190,192

The nuclei ^{186,188,190,192}Os have been studied in great detail by Wu et al. [22] using multi-Coulomb excitation. This has provided a large number of $E2$ matrix elements of good to very good precision. These Osmium nuclei are among the best candidates for triaxial rotation in nuclei. This is because of the very low 2_2^+ energy, as shown in Figure 21. Further, these nuclei exhibit low $K^\pi = 4^+$ bands which qualitatively agree with expectations of a triaxial rotor description. However, as discussed later, the interpretation of those $K^\pi = 4^+$ structures is the subject of controversy [33, 34, 35, 36].

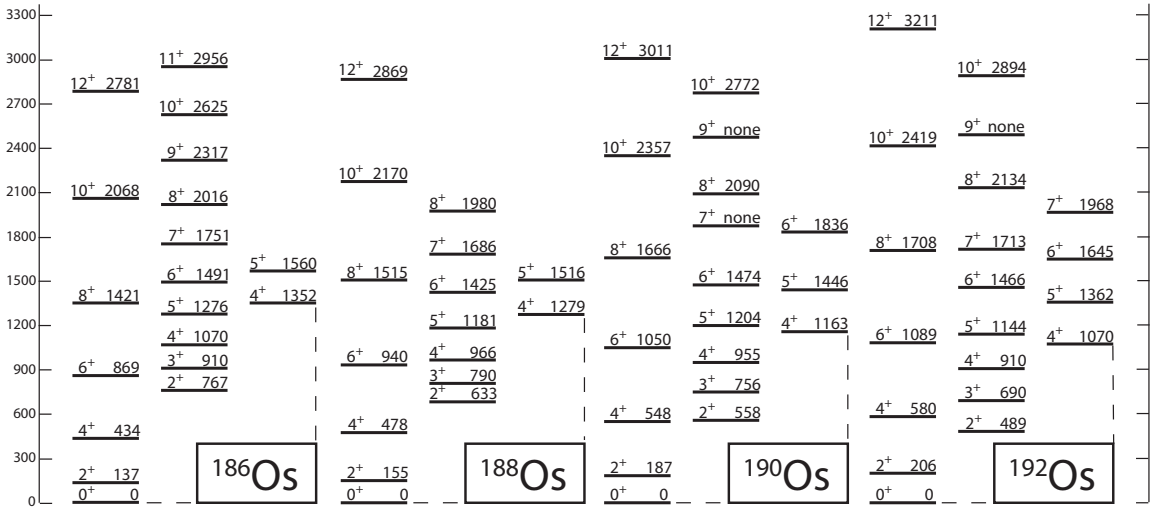

Figure 21: Energy levels for ^{186,188,190,192}Os showing the lowest $K = 0$, 2, and 4 bands. The energy data are taken from ENSDF [11].

4.3.1 Ground and Gamma Band Evaluation

The model is evaluated with the experimental reduced $E2$ matrix elements in Table 8 which were taken from Wu and Cline [22]. These local systematics provide a valuable means for testing axially asymmetric rotor models. Reduced $E2$ matrix elements are ideal for testing models because they provide signs and diagonal matrix elements ($B(E2)$'s square the matrix element).

Table 8: Experimental $\langle I_f||\hat{T}^{(2)}||I_i\rangle$'s (e·b), $(I_i \to I_f)$

	^{186}Os	^{188}Os	^{190}Os	^{192}Os
$2_g \to 2_g$	-1.75^{+22}_{-13}	-1.73^{+19}_{-5}	-1.25^{+22}_{-13}	-1.21^{+6}_{-17}
$4_g \to 4_g$	-2.02^{+39}_{-18}	-2.00^{+9}_{-20}	-1.28^{+27}_{-19}	-0.73^{+26}_{-6}
$6_g \to 6_g$	-1.67^{+29}_{-31}	-1.60^{+18}_{-33}	-0.91^{+24}_{-15}	-1.16^{+11}_{-26}
$8_g \to 8_g$	-2.26^{+24}_{-108}	-1.38^{+44}_{-26}	-0.94^{+49}_{-41}	-1.31^{+18}_{-36}
$2_\gamma \to 2_\gamma$	2.12^{+6}_{-22}	2.10^{+9}_{-6}	1.53^{+6}_{-31}	0.985^{+45}_{-85}
$4_\gamma \to 4_\gamma$	-1.12^{+25}_{-23}	-1.22^{+16}_{-10}	-1.29^{+20}_{-25}	-0.83^{+9}_{-8}
$6_\gamma \to 6_\gamma$	$\oslash$	-1.33^{+23}_{-56}	-0.80^{+47}_{-27}	-1.35^{+11}_{-37}
$8_\gamma \to 8_\gamma$	$\oslash$	$\oslash$	-1.05^{+62}_{-38}	-0.91^{+49}_{-34}
$2_g \to 0_g$	1.674^{+25}_{-21}	1.585^{+10}_{-10}	1.530^{+20}_{-11}	1.456^{+8}_{-9}
$4_g \to 2_g$	2.761^{+61}_{-70}	2.642^{+25}_{-20}	2.367^{+80}_{-31}	2.115^{+29}_{-28}
$6_g \to 4_g$	3.89^{+8}_{-5}	3.31^{+4}_{-4}	2.970^{+63}_{-40}	2.930^{+74}_{-44}
$8_g \to 6_g$	4.32^{+11}_{-10}	3.97^{+11}_{-11}	3.72^{+10}_{-10}	3.58^{+10}_{-9}
$10_g \to 8_g$	5.02^{+93}_{-60}	5.00^{+34}_{-21}	3.98^{+44}_{-39}	3.80^{+16}_{-48}
$12_g \to 10_g$	5.16^{+38}_{-131}	3.76^{+30}_{-30}	$\oslash$	$\oslash$
$4_\gamma \to 2_\gamma$	1.965^{+87}_{-66}	1.78^{+7}_{-5}	1.871^{+42}_{-37}	1.637^{+24}_{-33}
$6_\gamma \to 4_\gamma$	2.78^{+18}_{-11}	2.46^{+10}_{-10}	2.60^{+12}_{-16}	2.09^{+6}_{-13}
$8_\gamma \to 6_\gamma$	3.26^{+35}_{-28}	2.55^{+22}_{-69}	2.60^{+36}_{-19}	2.31^{+17}_{-16}
$10_\gamma \to 8_\gamma$	3.45^{+88}_{-40}	$\oslash$	$\oslash$	$\oslash$
$2_\gamma \to 0_g$	0.545^{+13}_{-7}	0.483^{+2}_{-9}	0.444^{+9}_{-7}	0.430^{+8}_{-4}
$2_\gamma \to 2_g$	0.897^{+64}_{-14}	0.865^{+11}_{-11}	1.065^{+20}_{-37}	1.230^{+34}_{-16}
$4_g \to 2_\gamma$[1]	0.227^{+32}_{-32}	0.378^{+50}_{-63}	0.19^{+12}_{-9}	0.35^{+16}_{-4}
$4_\gamma \to 2_g$	0.419^{+27}_{-15}	0.283^{+8}_{-7}	0.203^{+7}_{-7}	0.130^{+5}_{-8}
$4_\gamma \to 4_g$	1.220^{+62}_{-55}	1.10^{+3}_{-3}	1.435^{+43}_{-45}	1.35^{+8}_{-4}
$6_g \to 4_\gamma$[1]	0.67^{+30}_{-12}	0.57^{+7}_{-12}	0.66^{+26}_{-8}	0.40^{+9}_{-9}
$6_\gamma \to 4_g$	$\pm 0.325^{+20}_{-26}$	$\pm 0.127^{+6}_{-12}$	0.195^{+75}_{-74}	$\pm 0.069^{+157}_{-73}$
$6_\gamma \to 6_g$	1.37^{+9}_{-11}	1.46^{+13}_{-25}	1.76^{+20}_{-15}	1.49^{+15}_{-6}
$4_3 \to 2_g$	0.08^{+5}_{-8}	0.123^{+23}_{-23}	0.052^{+5}_{-7}	0.115^{+45}_{-31}
$4_3 \to 2_\gamma$	1.19^{+13}_{-14}	0.83^{+4}_{-3}	0.77^{+5}_{-5}	0.786^{+37}_{-37}
$4_3 \to 3_\gamma$[1]	-1.52^{+9}_{-29}	-1.17^{+17}_{-5}	-1.55^{+7}_{-40}	-1.63^{+11}_{-22}
$4_3 \to 4_\gamma$	1.83^{+32}_{-34}	1.64^{+7}_{-7}	1.59^{+11}_{-17}	1.19^{+8}_{-11}
$4_3 \to 4_3$	2.35^{+92}_{-69}	2.68^{+22}_{-19}	1.02^{+18}_{-4}	1.28^{+15}_{-41}

[1] Note: $\langle I_f||\hat{T}^{(2)}||I_i\rangle$ is not hermitian. In our case $\langle I_f||\hat{T}^{(2)}||I_i\rangle = (-1)^{I_f - I_i}\langle I_i||\hat{T}^{(2)}||I_f\rangle$.

We fit the Osmium isotopes to the $I \leq 2$ space and obtain, Table 9, exact solutions for the parameters of the triaxial rotor model. The parameters can be adjusted (e.g., Γ_2) to provide a best average fit but it is instructive to fix the parameters to the readily available and exactly solvable $I \leq 2$ data and understand how the model breaks down thereafter (discussed later).

Table 9: Triaxial rotor starting parameters where $\gamma + \Gamma_2 > 15^\circ$ (irrotational limit).

mass	A (keV)	F (keV)	Q_0 (e·b)	γ°	Γ_2°	G (keV)
186	22.86	157.6	5.582	20.43	−2.40	−3.82
188	25.84	119.5	5.254	19.93	−2.98	−3.60
190	31.12	92.8	5.051	22.12	−5.94	−5.64
192	34.30	70.8	4.814	25.19	−8.74	−6.44

The $E2$ sensitive parameters are shown and correlated in Figure 22. Anti-correlation is revealed between Q_0 and γ, and it is relatively constant among the isotopes (e.g., $Q_0 \sin\gamma = 1.95, 1.79, 1.90$, and 2.05, respectively, for ^{186,188,190,192}Os). This anti-correlation consistency has been observed before, [37]. The ratios Γ_2/Γ_{irrot} are 0.441, 0.604, 0.783, 0.644 for ^{186,188,190,192}Os which are in direct support of earlier findings in the systematics [20] (i.e, irrotational and rigid flow fail).

The triaxial two-band prescription is tested with the starting parameters of Table 9 against the data in Table 8 and the results are shown in Table 10. The starting parameters obtained from the $I \leq 2$ space fit the data to the following precision level (excluding the data used in the fit): 3 of 21 ^{186}Os matrix elements are outside 30%, similarly 5 of 21 for ^{188}Os, 9 of 21 for ^{190}Os, and 8 of 21 for ^{192}Os. The disagreements, due to destructive-interference, are in the interband transitions (e.g., $\Delta I = -2$ and $\Delta K = -2$) and the diagonal reduced matrix elements.

In order to explore the sensitivity of the model, percent difference curves, Figure 23 through Figure 26, are plotted against Γ_2 (Γ_I is a function of Γ_2) with Q_0 and γ held constant. The value for Q_0 is known to be good from intraband transition agreement. The

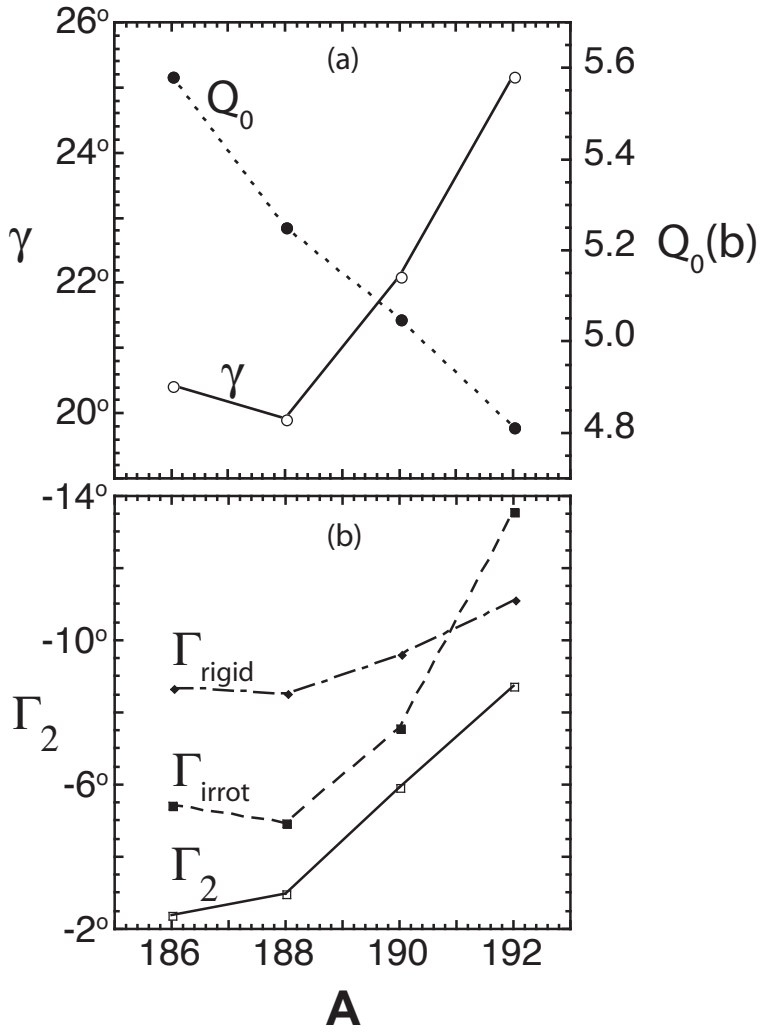

Figure 22: (a): Systematics of the fitted values of Q_0 and γ, cf. Table 9. (b): Systematics of the fitted values of Γ_2, cf. Table 9. The values of Γ_{irrot} determined using Eq. (68) are also shown.

ordering of the percent difference curves are (from left to right): diagonal matrix elements, intraband transitions, and interband transitions. The transitions can be categorized in terms of sensitivity to Γ_2 from most sensitive to least sensitive by: $\Delta I = \pm 2$ interband transitions, diagonal matrix elements, $\Delta I = 0$ interband transitions, and intraband transitions. The extreme sensitivity of $\Delta I = -2$, $\Delta K = -2$ transitions to Γ_2 suggest that the spin dependence, which relates Γ_I to Γ_2, is too strong (e.g., the $I > 2$ interband transitions intersect at a lower Γ_2).

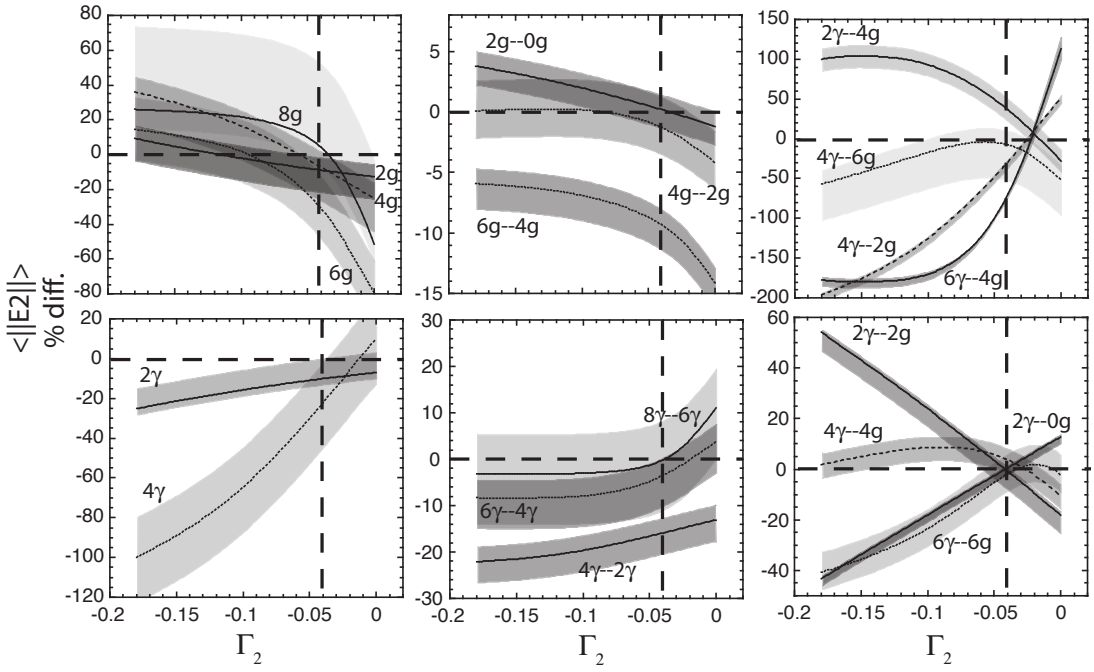

Figure 23: Percent difference for calculated versus experimental $E2$ matrix elements for ^{186}Os. The quantity $\langle||E2||\rangle$ % diff. $= (\langle||E2||\rangle_{\rm th} - \langle||E2||\rangle_{\rm ex}) \times 100 / |\langle||E2||\rangle_{\rm ex}|$. The vertical dashed lines are the starting values (cf. Table 9) for Γ_2, given here in radians. The shaded zones reflect the uncertainties in the experimental quantities. Quantities labeled, e.g., "4_γ" are diagonal matrix elements. (Note the very different vertical scales used.)

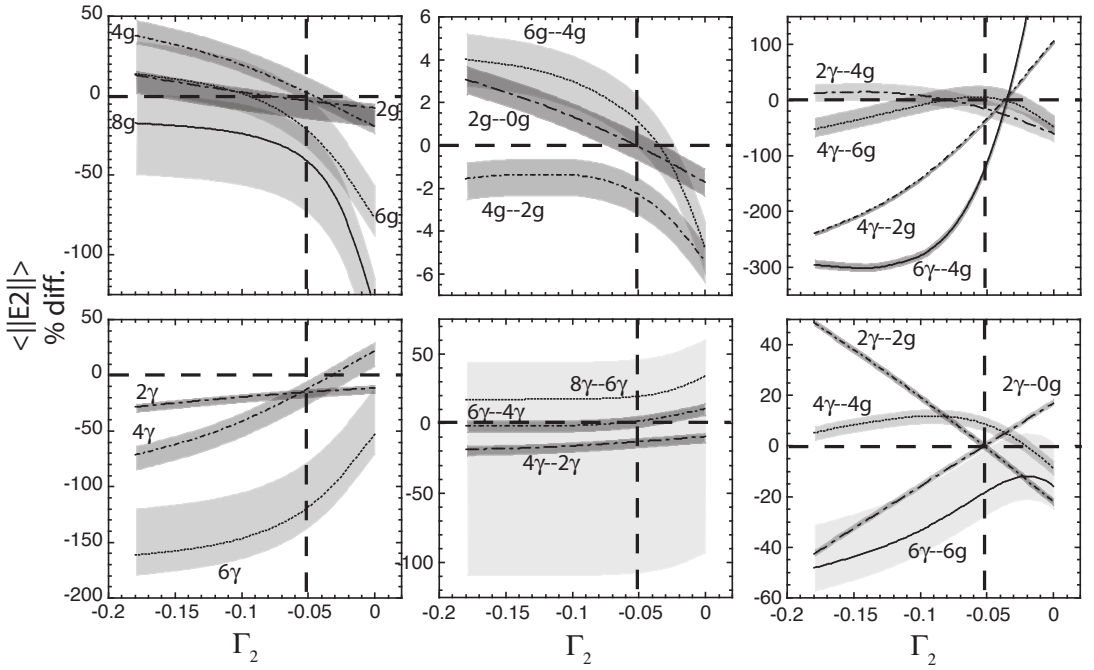

Figure 24: Percent difference curves for ^{188}Os. See caption to Figure 23 for details.

Table 10: Calculated $\langle||E2||\rangle$ values for ^{186,188,190,192}Os in e·b. The % values are the differences $(\langle||E2||\rangle_{\rm th} - \langle||E2||\rangle_{\rm ex}) \times 100/|\langle||E2||\rangle_{\rm ex}|$.

	^{186}Os $Q_0 = 5.582$ $\gamma = 20.43°$ $\Gamma_2 = -2.40°$	^{188}Os $Q_0 = 5.254$ $\gamma = 19.93°$ $\Gamma_2 = -2.98°$	^{190}Os $Q_0 = 5.051$ $\gamma = 22.12°$ $\Gamma_2 = -5.94°$	^{192}Os $Q_0 = 4.814$ $\gamma = 25.19°$ $\Gamma_2 = -8.74°$
$2_1 - 0_1$	1.6741 (fit)	1.5851 (fit)	1.5299 (fit)	1.4561 (fit)
$4_1 - 2_1$	2.7281 (-1.2%)	2.5840 (-2.2%)	2.4933 $(+5.3\%)$	2.3673 $(+11.9\%)$
$6_1 - 4_1$	3.533 (-9.2%)	3.351 $(+1.2\%)$	3.2769 $(+10.3\%)$	3.1438 $(+7.3\%)$
$8_1 - 6_1$	4.257 (-1.5%)	4.039 $(+1.7\%)$	3.946 $(+6.1\%)$	3.770 $(+5.3\%)$
$10_1 - 8_1$	4.903 (-2.3%)	4.640 (-7.5%)	4.501 $(+13.1\%)$	4.290 $(+12.9\%)$
$12_1 - 10_1$	5.466 $(+5.9\%)$	5.160 $(+31.4\%)$	4.985 $(\oslash)(\oslash)$	4.748 $(\oslash)(\oslash)$
$4_2 - 2_2$	1.6505 (-16.0%)	1.547 (-13.1%)	1.3996 (-25.2%)	1.2488 (-23.7%)
$6_2 - 4_2$	2.674 (-3.8%)	2.498 $(+1.5\%)$	2.259 (-13.1%)	2.032 (-2.8%)
$8_2 - 6_2$	3.244 (-0.5%)	3.043 $(+19.3\%)$	2.784 $(+7.1\%)$	2.506 $(+8.5\%)$
$10_2 - 8_2$	3.682 $(+6.7\%)$	3.470 $(\oslash)(\oslash)$	3.195 $(\oslash)(\oslash)$	2.877 $(\oslash)(\oslash)$
$2_2 - 0_1$	0.5449 (fit)	0.4831 (fit)	0.4439 (fit)	0.4299 (fit)
$2_2 - 2_1$	0.8969 (fit)	0.8648 (fit)	1.0647 (fit)	1.2300 (fit)
$2_2 - 4_1$	0.3156 $(+39.0\%)$	0.3222 (-14.8%)	0.407 $(+114.4\%)$	0.409 $(+17.0\%)$
$4_2 - 2_1$	0.2834 (-32.4%)	0.1776 (-37.2%)	-0.0638 (-131.4%)	-0.1498 (-215.2%)
$4_2 - 4_1$	1.2722 $(+4.3\%)$	1.198 $(+8.9\%)$	1.2537 (-12.6%)	1.215 (-10.0%)
$4_2 - 6_1$	0.630 (-6.0%)	0.604 $(+6.0\%)$	0.498 (-24.5%)	0.328 (-17.9%)
$6_2 - 4_1$	0.0747 (-77.0%)	-0.0340 (-126.8%)	-0.1690 (-186.7%)	-0.1208 (-275.1%)
$6_2 - 6_1$	1.340 (-2.2%)	1.191 (-18.4%)	0.978 (-44.4%)	0.832 (-44.1%)
$2_1 - 2_1$	-1.903 (-8.8%)	-1.782 (-3.0%)	-1.579 (-26.3%)	-1.334 (-10.3%)
$4_1 - 4_1$	-2.148 (-6.3%)	-1.954 $(+2.3\%)$	-1.431 (-11.8%)	-0.982 (-34.6%)
$6_1 - 6_1$	-2.155 (-29.0%)	-1.926 (-20.4%)	-1.357 (-49.1%)	-0.955 $(+17.6\%)$
$8_1 - 8_1$	-2.127 $(+5.9\%)$	-1.928 (-39.7%)	-1.457 (-54.9%)	-1.081 $(+17.48\%)$
$2_2 - 2_2$	1.903 (-10.2%)	1.782 (-15.2%)	1.579 $(+3.2\%)$	1.3343 $(+35.5\%)$
$4_2 - 4_2$	-1.384 (-23.5%)	-1.381 (-13.2%)	-1.728 (-33.9%)	-1.959 (-136.0%)
$6_2 - 6_2$	-2.990 $(\oslash)(\oslash)$	-2.932 (-120.5%)	-3.246 (-305.7%)	-3.329 (-146.6%)
$8_2 - 8_2$	-4.141 $(\oslash)(\oslash)$	-3.990 $(\oslash)(\oslash)$	-4.151 (-295.3%)	-4.139 (-354.8%)

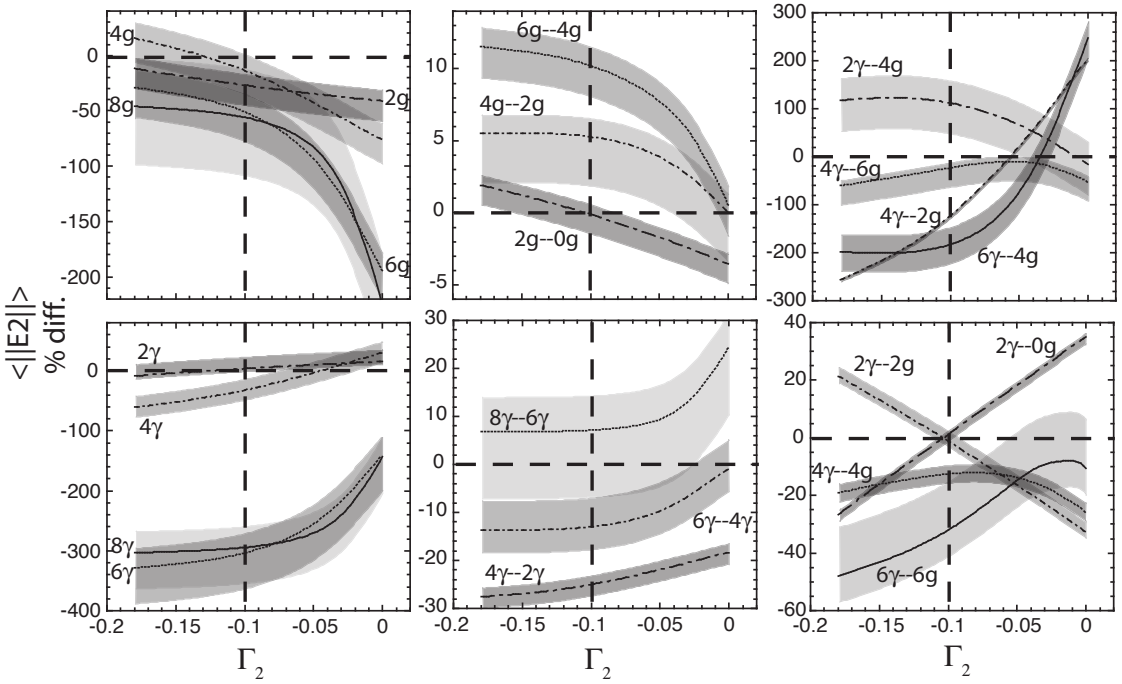

Figure 25: Percent difference curves for ^{190}Os. See caption to Figure 23 for details.

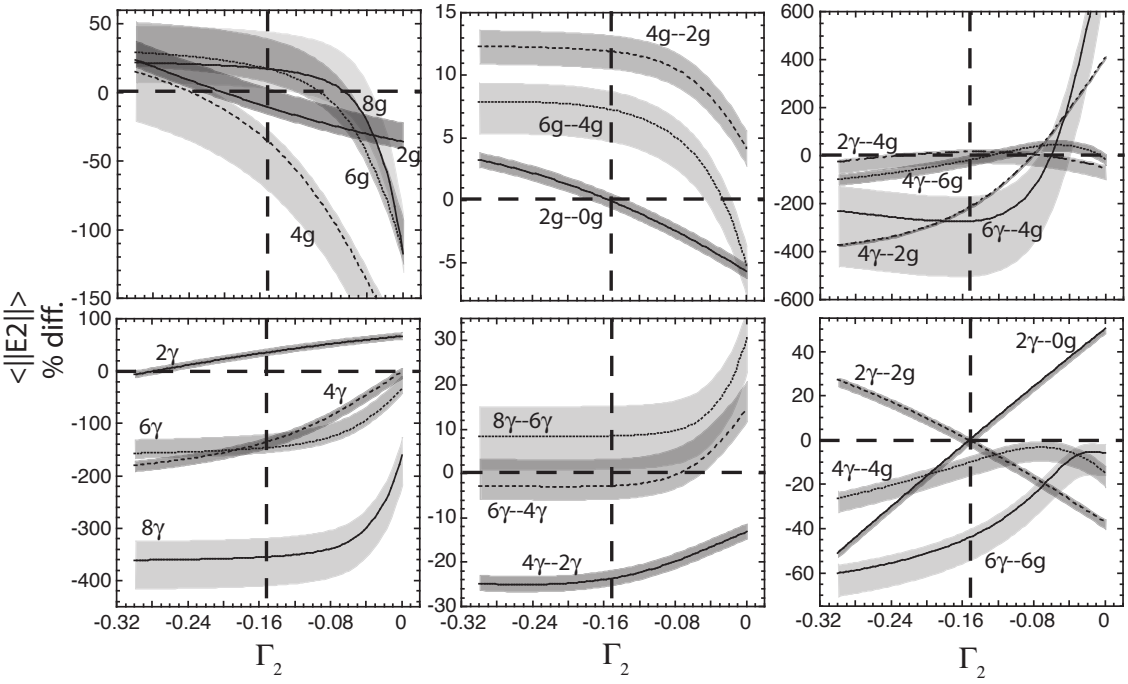

Figure 26: Percent difference curves for ^{192}Os. See caption to Figure 23 for details.

The triaxiality angle, γ, is deduced to be adequately stable (i.e, much more stable than Γ_2) from the fact that the Γ_2 correlations (intersection of curves) for the interband transitions in Figure 23 through Figure 26 occur near or at the 0% horizontal line. The reduced matrix elements for interband transitions change monotonically with changes in γ. Increasing γ adds a positive contribution to the strength of the matrix element and decreasing γ adds a negative contribution to the strength.

The breakdown of the mixing strength with increasing spin is shown in Figure 27 for destructively interfering $\Delta I = -2$, $\Delta K = -2$ transitions. This is in agreement with the cubic term measured in the ^{166}Er precision study. Figure 27 also shows the use of this perspective to determine the sign of the $6_\gamma \rightarrow 4_g$ matrix element for ^{186,188,192}Os (where ^{190}Os is shown for comparison but is reported by Wu et al. to be positive, cf. Table 8). A negative value for ^{186}Os is not allowed by the model based on its quadrupole strength and triaxiality angle, and a negative value for ^{192}Os would suggest a weaker mixing strength than that for ^{190}Os which is more symmetric. The $6_\gamma \rightarrow 4_g$ matrix elements are determined to be positive.

The triaxial energies (full diagonalization), Figure 28, begin to diverge from experiment at high spin partially due to fitting the inertia parameter, A, to spin two. While A can be adjusted to produce a better fit, it is irrelevant to the model with regard to the relative energies and eigenvectors. Since $AI(I+1)$ sets the absolute placement for all diagonal matrix elements in the Hamiltonian, the eigenvectors and relative energies are only dependent on Γ_I and therefore G/F. Notice that the energy difference is constant for all spins when there is no mixing and that it increases with spin as mixing is turned on. However, the experimental energy difference with spin is roughly constant and in fact ^{186}Os and ^{188}Os have points where the energy difference even decreases with spin.

Agreement of the energy differences between experiment and fitted Γ_2 turns out to be partially correlated to the agreement in $E2$ matrix elements (breaks down above spin 4 for ^{186,188}Os and at spin 4 for ^{190,192}Os). Also, the "Fit Adjusted (Γ_2)" represents a decreased

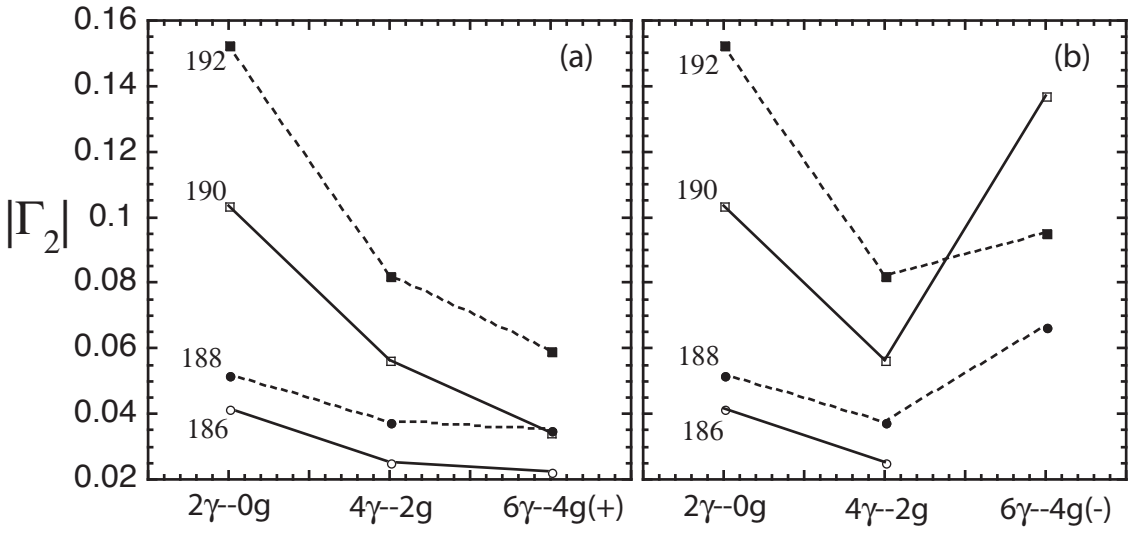

Figure 27: (a): Exact fit of Γ_2 to destructive interference ($\Delta I = -2$ and $\Delta K = -2$) matrix elements. (b): A similar plot to (a) for the choice of negative values for $6_\gamma \rightarrow 4_g$, cf. Table 8. Thus, there is a model-based preference for positive values for the $6_\gamma \rightarrow 4_g$ matrix elements. (A negative value for $6_\gamma \rightarrow 4_g$ in ^{186}Os cannot be fitted by the model.)

adjustment in the fitted Γ_2 to the best fit for the interband ($K = 2$ to $K = 0$) transitions. Since the interband transitions involving spin 4 and 6 are the most sensitive (because of the systematic breakdown), the adjusted fit value falls between the two. Notice that the energy difference of the adjusted fit is correlated to the experimental energy difference up to spin 6. In fact, the lines intersect exactly between spin 4 and 6 for ^{190,192}Os. The lack of complete correlation suggests that not only is the off-diagonal spin dependence breaking down in the Hamiltonian but that the diagonal K dependence is breaking down as well.

In order to understand the deviation of the γ-band diagonals (which cannot be accommodated by the triaxial two-band prescription or full diagonalization of the triaxial rotor), we inspect the influence and sensitivity of stronger mixing from higher K admixtures. The Hamiltonian diagonalized for $I = 4$ was

$$H(4) = \begin{pmatrix} 0 & 12\sqrt{5} & 0 \\ 12\sqrt{5} & 4F/G' & 4\sqrt{7} \\ 0 & 4\sqrt{7} & 16F'/G' \end{pmatrix}, \tag{75}$$

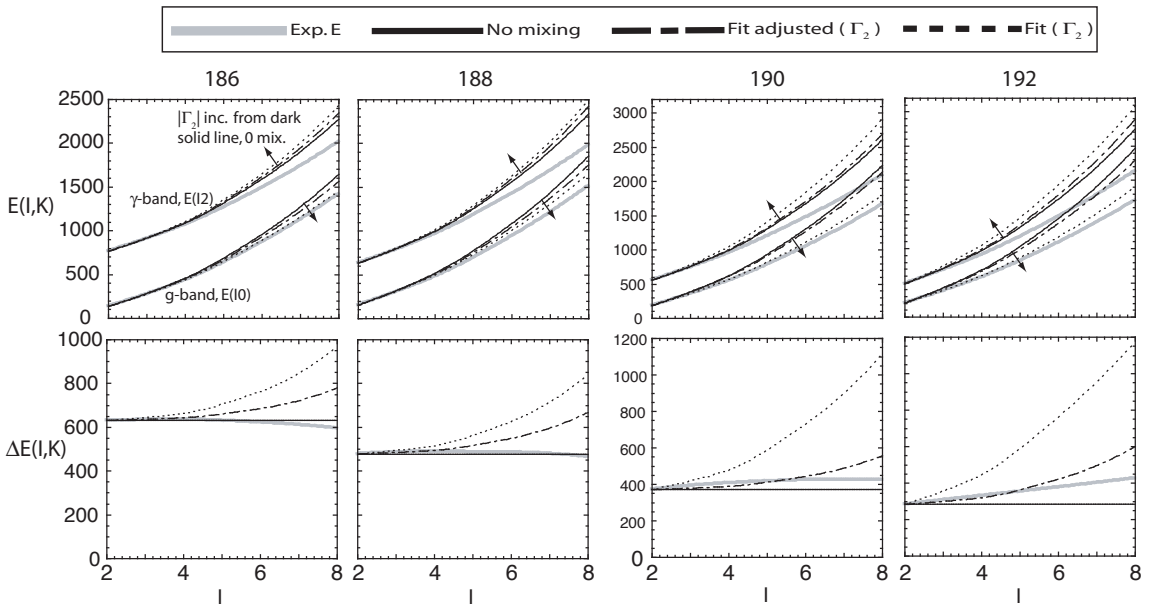

Figure 28: Triaxial energies (full diagonlization). The reduced $E2$ matrix elements do not correlate with the absolute energies but do correlate with the energy difference for a given spin I. Since we never mix states of different I, we should expect a stronger correlation of the angular state amplitudes with the relative energy structure of a given I.

where the common diagonal energy of $20A$ was removed, $F' = 0.38F$, and the remaining matrix was rescaled by $1/G'$, where G' was obtained from Eq. (40) using the "adjusted" Γ_2 values of Figure 28 from Figure 27 (i.e., $G'(\Gamma_2) = -3.10(-1.95°)$, $-3.04(-2.52°)$, $-4.32(-4.58°)$, $-5.00(-6.88°)$ for ^{186,188,190,192}Os, respectively). The Hamiltonian diagonalized for $I = 6$ was

$$H(6) = \begin{pmatrix} 0 & 4\sqrt{210} & 0 & 0 \\ 4\sqrt{210} & 4F/G' & 6\sqrt{30} & 0 \\ 0 & 6\sqrt{30} & 16F'/G' & 2\sqrt{66} \\ 0 & 0 & 2\sqrt{66} & 36F'/G' \end{pmatrix}. \tag{76}$$

It is seen that the off-diagonal matrix element strengths decrease with increasing K and, e.g., for ^{192}Os

$$H(6) = \begin{pmatrix} 0 & 57.96 & 0 & 0 \\ 57.96 & -56.62 & 32.86 & 0 \\ 0 & 32.86 & -86.07 & 16.25 \\ 0 & 0 & 16.25 & -193.65 \end{pmatrix}. \tag{77}$$

The diagonal separation between $K = 0, 2$ is surpassed by the off-digonal strength and the diagonal separation between $K = 2, 4$ is nearly surpassed by it's off-diagonal strength. This produces severe alteration to the gamma-band state amplitudes.

The results of modifying the triaxial Hamiltonian to approximate the effect of higher K-admixtures on the ground and gamma band are shown in Table 11. The effect of high-K admixtures is much more dramatic for the γ-band diagonals. This is due to a significant change of the state amplitudes for the γ band along with a large change in weighting from the Clebsch-Gordan coefficients (these can be very different between bands for the same $I_\mathrm{i} \rightarrow I_\mathrm{f}$). The result is that the γ-band diagonal $E2$ matrix elements are significantly improved while the other matrix elements are maintained. Furthermore, the predicted energy separations for a given I^+ correlate with agreement in the matrix elements.

Table 11: Calculated $\langle||E2||\rangle$ values for ^{186,188,190,192}Os in e·b. The % values are the differences $(\langle||E2||\rangle_{\rm th} - \langle||E2||\rangle_{\rm ex}) \times 100/|\langle||E2||\rangle_{\rm ex}|$. The values are given to one decimal place more than the experimental quantities.

	^{186}Os Q_0, γ, F $F' = 0.38F$ $G' = -3.10$	^{188}Os Q_0, γ, F $F' = 0.38F$ $G' = -3.04$	^{190}Os Q_0, γ, F $F' = 0.38F$ $G' = -4.32$	^{192}Os Q_0, γ, F $F' = 0.38F$ $G' = -5.00$
$2_1 - 0_1$	1.6697 (−0.3%)	1.5812 (−0.2%)	1.5190 (−0.7%)	1.4414 (−1.0%)
$4_1 - 2_1$	2.7170 (−1.6%)	2.5761 (−2.5%)	2.4853 (+5.0%)	2.3628 (+11.7%)
$6_1 - 4_1$	3.512 (−9.7%)	3.338 (+0.8%)	3.2369 (+9.0%)	3.1448 (+7.3%)
$8_1 - 6_1$	4.237 (−1.9%)	4.035 (+1.6%)	4.009 (+7.8%)	3.840 (+7.3%)
$4_2 - 2_2$	1.7509 (−10.9%)	1.661 (−6.7%)	1.6115 (−13.9%)	1.5580 (−4.8%)
$6_2 - 4_2$	2.865 (+3.0%)	2.668 (+8.5%)	2.224 (−14.5%)	2.172 (+3.9%)
$8_2 - 6_2$	3.550 (+8.9%)	3.303 (+29.5%)	3.105 (+19.4%)	2.906 (+25.8%)
$2_2 - 0_1$	0.5581 (+2.4%)	0.4958 (+2.6%)	0.4800 (+8.1%)	0.4771 (11.0%)
$2_2 - 2_1$	0.8668 (−3.4%)	0.8362 (−3.3%)	0.9888 (−7.2%)	1.1406 (−7.3)
$2_2 - 4_1$	0.2949 (+29.9%)	0.3072 (−18.7%)	0.401 (+111.0%)	0.455 (+30.0%)
$4_2 - 2_1$	0.3471 (−17.2%)	0.2357 (−16.7%)	0.0572, (−71.8%)	−0.0402 (−130.9%)
$4_2 - 4_1$	1.2524 (+2.7%)	1.187 (+7.9%)	1.2849 (−10.5%)	1.309 (−3.1%)
$4_2 - 6_1$	0.634 (−5.4%)	0.640 (+12.2%)	0.867 (+31.3%)	0..587 (+46.8%)
$6_2 - 4_1$	0.1535 (−52.8%)	0.0141 (−88.9%)	−0.3927 (−301.4%)	−0.1797 (−360.4%)
$6_2 - 6_1$	1.406 (+2.6%)	1.276 (−12.6%)	1.123 (−36.2%)	1.105 (−25.9%)
$2_1 - 2_1$	−1.917 (−9.6%)	−1.795 (−3.8%)	−1.627 (−30.2%)	−1.411 (−16.7%)
$4_1 - 4_1$	−2.218 (−9.8%)	−2.017 (−0.8%)	−1.576 (−23.1%)	−1.104 (−51.3%)
$6_1 - 6_1$	−2.261 (−35.40%)	−1.987 (−24.2%)	−1.170 (−28.6%)	−0.822 (+29.2%)
$8_1 - 8_1$	−2.160 (+4.4%)	−1.874 (−35.8%)	−1.234 (−31.3%)	−0.719 (+45.1%)
$2_2 - 2_2$	1.917 (−9.6%)	1.795 (−14.5%)	1.627 (+6.3%)	1.4115 (+43.3%)
$4_2 - 4_2$	−1.179 (−5.3%)	−1.136 (+6.9%)	−1.102 (+15.6%)	−0.826 (+0.5%)
$6_2 - 6_2$	−2.168 (⊘)(⊘)	−1.938 (−45.7%)	−0.818 (−2.2%)	−0.751 (+44.4%)
$8_2 - 8_2$	−2.547 (⊘)(⊘)	−2.181 (⊘)(⊘)	−1.484 (−41.3%)	−0.999 (−9.7%)

4.3.2 K=4 Bands

The low-lying energies of the the $K^\pi = 4^+$ band heads (cf. Figure 21) qualitatively imply a triaxial structure but they are lower in energy than the triaxial rotor model suggests. While this is a clear failure of the model, the issue is not clear-cut because spectroscopic data indicates that the structure of the $K^\pi = 4^+$ bands is complex. Specifically, the 4^+ band heads exhibit not only collective $E2$ transitions to the $K^\pi = 2^+$ bands but also hexadecapole character, i.e., direct $E4$ population from the ground state [38] and proton "broken-pair" character from one-proton transfer spectroscopy [39]. This complex structure of low-lying $K^\pi = 4^+$ bands may even be widely occurring, [40].

The complex structure of these 4^+ bands suggests that other 4^+ bands should exist which would be the other "fragments" of these mixed configurations. If these were known, the $K^\pi = 4^+$ model space could be expanded and a full calculation could be carried out. However, they are not known. Therefore, we investigate the $E2$ strength associated with these bands as if the bands were pure triaxial rotor bands.

The calculated $K^\pi = 4^+$ band-head transitions and diagonal matrix elements are compared to the data in Table 8 and the results are shown in Table 12. The three different calculation types shown are: "FULL TRIAX" , "FULL F'-TRIAX", and "SUBSPACE($K = 2, 4$)". The "FULL TRIAX" parameters and calculations are for the full triaxial rotor model and it is a continuation of the model predictions in Table 10 using the starting parameters in Table 9. The triaxial rotor model clearly fails. The "FULL F'-TRIAX" parameters and calculations are for the adjusted traixal rotor Hamiltonian in Equation (75) which was used to approximate the effect of stronger K-admixtures. This approximation achieves better success at fitting the matrix element data than the full triaxial rotor ("FULL TRIAX") but it still fails. The "SUBSPACE($K = 2, 4$)" parameters and calculations are for the two-by-two ($K = 2, 4$) subspace of the triaxial rotor (where the intrinsic quadrupole deformation, Q_0, was fixed to the $K = 0, 2$ subspace). The $K = 2, 4$ subspace fit achieves the best agreement since it only has to accommodate 5 matrix elements with two adjusted parameters

(the triaxiality, γ, and the mixing, $\Gamma_{I,K=4}$ or $G_{\rm sub}/F_{\rm sub}$).

The "FULL F'-TRIAX" and "SUBSPACE($K = 2, 4$)" approximations reveal that the $K = 0, 2, 4$ space has additional K-admixtures. Both methods provide better agreement to the data than the triaxial rotor model but they fail to properly model the space for K-admixtures. The "FULL F'-TRIAX" alters the triaxial space (e.g., F to F') as opposed to adding additional K-admixtures into the model. The "SUBSPACE($K = 2, 4$)" uses a two-by-two space which is known to be too small in dimension (e.g., the $I = 4$ state amplitudes are significantly distributed amongst the possible body projections, K) and as a result, the triaxiality ($\gamma_{\rm sub}$) is significantly different. Furthermore, the $K = 2, 4$ subspace method does not fit $K = 4$ intraband transitions (i.e., none exist) so the stability of $\gamma_{\rm sub}$ in the $K = 2, 4$ subspace is unknown.

A separate and more direct way for testing possible K-admixtures in the $K = 0, 2, 4$ triaxial space is provided by using the quadrupole trace relation, cf., Equation (46), for the full $I = 4$ triaxial space and it is given by

$$Tr\{\hat{T}^{(2)}\}_{I=4} = Q_0 \cos\gamma \sqrt{\frac{5}{16\pi}}\sqrt{9} \times \{\langle 40; 20|40\rangle + \langle 42; 20|42\rangle + \langle 44; 20|44\rangle\} = 0. \qquad (78)$$

From the sum of the Clebsch-Gordan coefficients, the trace is zero for the model. Experimentally, the sum $\Sigma_{i=1,2,3}\langle 4_i||E2||4_i\rangle$ is equal to $-0.79(^{186}{\rm Os})$, $-0.54(^{188}{\rm Os})$, $-1.55(^{190}{\rm Os})$, and $-0.28(^{192}{\rm Os})$. This (with the hexadecapole and proton "broken-pair" data) indicates missing $K = 4$ (positive) diagonal strength.

Table 12: $K = 4$ calculated $\langle I_f||\hat{T}^{(2)}||I_i\rangle$'s, $(I_i \to I_f)$. The greater G/F, the stronger the mixing.

	"FULL TRIAX"	"FULL F'-TRIAX"	"SUBSPACE($K = 2, 4$)"
^{186}Os	Q_0 γ G/F	Q_0 γ $G'/F = 0.8115G/F$ $G'/F' = 2.136G/F$	$Q_{\rm sub} = Q_0$ $\gamma_{\rm sub} = 2.04\gamma$ $G_{\rm sub}/F_{\rm sub} = 23.30G/F$
$4_2 - 2_2{}^1$	1.6505 (−16.0%)	1.7509 (−10.9%)	1.9648 (0%)
$4_3 - 2_1$	0.045 (−44.1%)	$\sim$ 0.000 (−100.4%)	$\oslash$
$4_3 - 2_2$	0.935 (−21.5%)	0.7971 (−33.0%)	1.190 (0%)
$4_3 - 3_1$	0.781 (−48.6%)	0.975 (−35.8%)	2.057 (+35.4%)
$4_3 - 4_2$	0.526 (−71.2%)	0.899 (−50.8%)	1.858 (+1.5%)
$4_3 - 4_3$	3.511 (+49.4%)	3.397 (+44.5%)	1.710 (−27.2%)
^{188}Os	Q_0 γ G/F	Q_0 γ $G'/F = 0.8444G/F$ $G'/F' = 2.222G/F$	$Q_{\rm sub} = Q_0$ $\gamma_{\rm sub} = 1.45\gamma$ $G_{\rm sub}/F_{\rm sub} = 10.99G/F$
$4_2 - 2_2{}^1$	1.547 (−13.1%)	1.661 (−6.7%)	1.780 (0%)
$4_3 - 2_1$	0.0512 (−58.4%)	0.0058 (−95.2%)	$\oslash$
$4_3 - 2_2$	0.850 (+2.4%)	0.677 (−18.4)	0.830 (0%)
$4_3 - 3_1$	0.732 (−37.5%)	0.970 (−17.1%)	1.502 (28.3%)
$4_3 - 4_2$	0.508 (−69.0%)	0.975 (−40.5%)	1.491 (−9.1%)
$4_3 - 4_3$	3.310 (+23.5%)	3.153 (+17.7%)	2.550 (−4.9%)
^{190}Os	Q_0 γ G/F	Q_0 γ $G'/F = 0.7660G/F$ $G'/F' = 2.016G/F$	$Q_{\rm sub} = Q_0$ $\gamma_{\rm sub} = 1.70\gamma$ $G_{\rm sub}/F_{\rm sub} = 13.19G/F$
$4_2 - 2_2{}^1$	1.3996 (−25.2%)	1.6115 (−13.9%)	1.8667 (−0.2%)
$4_3 - 2_1$	0.1097 (+111.0%)	0.0395 (−24.1%)	$\oslash$
$4_3 - 2_2$	0.863 (+12.1%)	0.554 (−28.1%)	0.765 (−0.7%)
$4_3 - 3_1$	0.829 (−46.5.0%)	1.217 (−21.5%)	1.920 (+23.9%)
$4_3 - 4_2$	0.635 (−60.1%)	1.468 (−7.6%)	1.811 (+13.9%)
$4_3 - 4_3$	3.101 (+204.0%)	2.678 (+162.6%)	1.412 (+38.4%)
^{192}Os	Q_0 γ G/F	Q_0 γ $G'/F = 0.7764G/F$ $G'/F' = 2.043G/F$	$Q_{\rm sub} = Q_0$ $\gamma_{\rm sub} = 1.19\gamma$ $G_{\rm sub}/F_{\rm sub} = 3.82G/F$
$4_2 - 2_2{}^1$	1.2488 (−23.7%)	1.5580 (−4.8%)	1.6357 (−0.1%)
$4_3 - 2_1$	0.1743 (+51.6%)	0.0916 (−20.4%)	$\oslash$
$4_3 - 2_2$	0.8976 (+14.2%)	0.4206 (−46.5%)	0.7849 (−0.1%)
$4_3 - 3_1$	0.928 (−43.1%)	1.433 (−12.1%)	1.417 (−13.1%)
$4_3 - 4_2$	0.761 (−36.0%)	1.960 (+64.7%)	1.399 (+17.6%)
$4_3 - 4_3$	2.839 (+121.8%)	1.930 (+50.8)	2.270 (+77.4%)

CHAPTER V

CONCLUSION

Rotation plays a dominant role in even-even nuclear collectivity. In the cases studied, intraband transitions agree with rotor strengths for doubly-even collective nuclei. The details of the inertial flow have not been determined but it is found that they do not follow the simple idealization of rigid or irrotational flow. Nuclei appear to possess moments of inertia correlated to the quadrupole tensor but not according to irrotational or rigid flow.

The notable success of the rotor and band mixing in ^{166}Er (the most precise test ever) has built a foundation for the validity of the rotor and a better understanding of its breakdown. Less rotational nuclei can be studied in comparison with knowledge that the best symmetric rotor candidate breaks down in a simple systematic way (i.e., the mixing strength breaks down with spin).

The triaxial rotor has provided a means to view nuclear collectivity without any assumptions made to the inertial flow (by adding an additional parameter, Γ_I, to independently describe the inertia). From this perspective, it is realized that the inertia asymmetry (mixing angle, Γ_I) can behave constructively or destructively with the quadrupole triaxiality. This explains the limits of irrotational flow while accommodating data outside those limits.

The triaxial rotor generates several $\langle||E2||\rangle$'s (by fitting three matrix elements) that agree with the ^{186,188}Os local systematics and to a lesser degree the ^{190,192}Os systematics. Considering these nuclei are among the best triaxial (asymmetric) candidates and their $E2$ data correlate to the triaxial model parameters, it appears that triaxial rotation (e.g., rotation about the "symmetry" axis) is realized in nuclei.

The most dramatic and evident failure of the rotor model is the systematic breakdown in the mixing strength with increasing spin. This was first seen in the ^{166}Er precision study

to a small degree and it was confirmed in the ^{186,188,190,192}Os study (where it has a larger effect). Further, the band separation dependence (in K) breaks down for the Osmium isotopes sharply at $K = 4$. However, no global view for this has been studied.

More data are needed to test the triaxial rotor and to understand breakdowns for $K > 2$. Reduced $E2$ matrix elements for $3_1 \rightarrow I_\mathrm{f}$ transitions would be of great value in testing the model and the purity of the space (e.g., presence of K-admixtures from outside the model space) since its dimension of 1x1 reduces the mixing effects. Additionally, the ratio of $\langle 2_{1,2}||\hat{T}^{(2)}||3_1\rangle/\langle 0_1||\hat{T}^{(2)}||2_{2,1}\rangle = \pm\sqrt{\frac{5}{2}}$, cf., Equation (62), is the only constant relation of the model that is exact (except for the trace rule that sums to zero).

A global view of the $K = 4$ collective band requires more than the band-head ($I = 4$, $K = 4$) energy and transition strengths (where these are the only data for ^{186,188,190,192}Os). The band-head transitions can establish an off-diagonal deformation strength, $Q_0 \sin\gamma$, but this does not establish Q_0 or γ. Intraband transitions for the $K = 4$ band would need to be known as well to establish the diagonal quadrupole deformation strength, $Q_0 \cos\gamma$. Furthermore, additional $K = 4$ bands should be identified. Transitions from the $K = 6$ band head to the $K = 4$ band would provide even further constraints (e.g., mixing effects, F and G). A significant advance in understanding nuclear collectivity could be accomplished if these additional systematics are obtained.

APPENDIX A

TRIAXIAL TWO-BAND REDUCED $E2$ MATRIX ELEMENTS

$$\langle \text{final}||\hat{T}^{(2)}||\text{intial}\rangle$$

$$B(E2) = \frac{1}{2I_i+1}|\langle \text{final}||\hat{T}^{(2)}||\text{intial}\rangle|^2$$

$$\begin{aligned}
{}_{\text{even}}\langle I_1||\hat{T}^{(2)}||I_2\rangle_{\text{even}} = Q_0\sqrt{\frac{5}{16\pi}}\sqrt{2I_i+1}\times \\
[\cos\Gamma_f \sin\Gamma_i \cos\gamma\langle I_i 0; 20|I_f 0\rangle \\
+ \cos\Gamma_f \cos\Gamma_i \sin\gamma\langle I_i 2; 2,-2|I_f 0\rangle \\
- \sin\Gamma_f \cos\Gamma_i \cos\gamma\langle I_i 2; 20|I_f 2\rangle \\
- \sin\Gamma_f \sin\Gamma_i \sin\gamma\langle I_i 0; 22|I_f 2\rangle]
\end{aligned}$$

$$\begin{aligned}
{}_{\text{even}}\langle I_1||\hat{T}^{(2)}||I_1\rangle_{\text{odd}} = Q_0\sqrt{\frac{5}{16\pi}}\sqrt{2I_i+1}\times \\
[\cos\Gamma_f \sin\gamma\langle I_i 2; 2,-2|I_f 0\rangle \\
- \sin\Gamma_f \cos\gamma\langle I_i 2; 20|I_f 2\rangle]
\end{aligned}$$

$$\begin{aligned}
{}_{\text{even}}\langle I_1||\hat{T}^{(2)}||I_1\rangle_{\text{even}} = Q_0\sqrt{\frac{5}{16\pi}}\sqrt{2I_i+1}\times \\
[\cos\Gamma_f \cos\Gamma_i \cos\gamma\langle I_i 0; 20|I_f 0\rangle \\
- \cos\Gamma_f \sin\Gamma_i \sin\gamma\langle I_i 2; 2,-2|I_f 0\rangle \\
+ \sin\Gamma_f \sin\Gamma_i \cos\gamma\langle I_i 2; 20|I_f 2\rangle \\
- \sin\Gamma_f \cos\Gamma_i \sin\gamma\langle I_i 0; 22|I_f 2\rangle]
\end{aligned}$$

$$
\begin{aligned}
{}_{\text{even}}\langle I_2||\hat{T}^{(2)}||I_2\rangle_{\text{even}} = Q_0\sqrt{\frac{5}{16\pi}}\sqrt{2I_i+1}\times \\
&[\sin\Gamma_f \sin\Gamma_i \cos\gamma\langle I_i 0; 20|I_f 0\rangle \\
&+ \sin\Gamma_f \cos\Gamma_i \sin\gamma\langle I_i 2; 2,-2|I_f 0\rangle \\
&+ \cos\Gamma_f \cos\Gamma_i \cos\gamma\langle I_i 2; 20|I_f 2\rangle \\
&+ \cos\Gamma_f \sin\Gamma_i \sin\gamma\langle I_i 0; 22|I_f 2\rangle]
\end{aligned}
$$

$$
{}_{\text{odd}}\langle I_1||\hat{T}^{(2)}||I_1\rangle_{\text{odd}} = Q_0\sqrt{\frac{5}{16\pi}}\sqrt{2I_i+1}\cos\gamma\langle I_i 2; 20|I_f 2\rangle
$$

$$
\begin{aligned}
{}_{\text{even}}\langle I_2||\hat{T}^{(2)}||I_1\rangle_{\text{odd}} = Q_0\sqrt{\frac{5}{16\pi}}\sqrt{2I_i+1}\times \\
&[\sin\Gamma_f \sin\gamma\langle I_i 2; 2,-2|I_f 0\rangle \\
&+ \cos\Gamma_f \cos\gamma\langle I_i 2; 20|I_f 2\rangle]
\end{aligned}
$$

$$
\begin{aligned}
{}_{\text{odd}}\langle I_1||\hat{T}^{(2)}||I_2\rangle_{\text{even}} = Q_0\sqrt{\frac{5}{16\pi}}\sqrt{2I_i+1}\times \\
&[\cos\Gamma_i \cos\gamma\langle I_i 2; 20|I_f 2\rangle \\
&+ \sin\Gamma_i \sin\gamma\langle I_i 0; 22|I_f 2\rangle]
\end{aligned}
$$

γ-ground:

$$
\begin{aligned}
\langle 0_1||\hat{T}^{(2)}||2_2\rangle &= Q_0\sqrt{5}\sqrt{\frac{1}{16\pi}}\sin(\gamma+\Gamma_2) \\
\langle 2_1||\hat{T}^{(2)}||2_2\rangle &= Q_0\sqrt{5}\sqrt{\frac{5}{56\pi}}\sin(\gamma-2\Gamma_2) \\
\langle 4_1||\hat{T}^{(2)}||2_2\rangle &= Q_0\sqrt{5}\sqrt{\frac{5}{16\pi}}\left[\sqrt{\frac{36}{70}}\cos\Gamma_4\sin\Gamma_2\cos\gamma + \sqrt{\frac{1}{70}}\cos\Gamma_4\cos\Gamma_2\sin\gamma\right. \\
&\quad \left. - \sqrt{\frac{15}{70}}\sin\Gamma_4\cos(\Gamma_2-\gamma)\right]
\end{aligned}
$$

$$
\begin{aligned}
\langle 2_1||\hat{T}^{(2)}||3_1\rangle &= Q_0\sqrt{7}\sqrt{\frac{5}{16\pi}}\sqrt{\frac{5}{14}}\sin(\gamma+\Gamma_2) \\
\langle 4_1||\hat{T}^{(2)}||3_1\rangle &= Q_0\sqrt{7}\sqrt{\frac{5}{16\pi}}\sqrt{\frac{1}{7}}\left[\cos\Gamma_4\sin\gamma - \sqrt{\frac{12}{5}}\sin\Gamma_4\cos\gamma\right]
\end{aligned}
$$

Table 13: Clebsch-Gordan coefficients for $I_{\rm even} \to I_{\rm even}$

$\langle \vert \rangle$	$2 \to 0$	$2 \to 2$	$2 \to 4$	$4 \to 2$	$4 \to 4$	$4 \to 6$
$\langle I_i 0; 20 \vert I_f 0\rangle$	$\sqrt{\frac{1}{5}}$	$-\sqrt{\frac{2}{7}}$	$\sqrt{\frac{36}{70}}$	$\sqrt{\frac{2}{7}}$	$-\sqrt{\frac{20}{77}}$	$\sqrt{\frac{5}{11}}$
$\langle I_i 2; 2,-2 \vert I_f 0\rangle$	$\sqrt{\frac{1}{5}}$	$\sqrt{\frac{2}{7}}$	$\sqrt{\frac{1}{70}}$	$\sqrt{\frac{5}{42}}$	$\sqrt{\frac{27}{77}}$	$\sqrt{\frac{1}{33}}$
$\langle I_i 2; 20 \vert I_f 2\rangle$	0	$\sqrt{\frac{2}{7}}$	$\sqrt{\frac{15}{70}}$	$\sqrt{\frac{5}{42}}$	$-\frac{4}{\sqrt{385}}$	$\sqrt{\frac{112}{330}}$
$\langle I_i 0; 22 \vert I_f 2\rangle$	0	$\sqrt{\frac{2}{7}}$	$\sqrt{\frac{15}{70}}$	$\sqrt{\frac{1}{126}}$	$\sqrt{\frac{27}{77}}$	$\sqrt{\frac{14}{99}}$

$\langle \vert \rangle$	$6 \to 4$	$6 \to 6$	$6 \to 8$	$8 \to 6$	$8 \to 8$	$8 \to 10$
$\langle I_i 0; 20 \vert I_f 0\rangle$	$\sqrt{\frac{45}{(11)(13)}}$	$-\sqrt{\frac{42}{165}}$	$\sqrt{\frac{84}{195}}$	$\sqrt{\frac{28}{(5)(17)}}$	$-\sqrt{\frac{24}{(5)(19)}}$	$\sqrt{\frac{3(9)5}{17(19)}}$
$\langle I_i 2; 2,-2 \vert I_f 0\rangle$	$\sqrt{\frac{14}{(11)(13)}}$	$\sqrt{\frac{60}{165}}$	$\sqrt{\frac{1}{26}}$	$\sqrt{\frac{9}{(2)(51)}}$	$\sqrt{\frac{7}{19}}$	$\sqrt{\frac{14}{17(19)}}$
$\langle I_i 2; 20 \vert I_f 2\rangle$	$\sqrt{\frac{(12)(14)}{(5)(11)(13)}}$	$-\frac{30}{\sqrt{(165)(42)}}$	$\sqrt{\frac{135}{364}}$	$\sqrt{\frac{135}{(28)(17)}}$	$-\sqrt{\frac{10}{57}}$	$\sqrt{\frac{7(8)11}{17(19)5}}$
$\langle I_i 0; 22 \vert I_f 2\rangle$	$\sqrt{\frac{3}{(11)(13)}}$	$\sqrt{\frac{60}{165}}$	$\sqrt{\frac{3}{26}}$	$\sqrt{\frac{1}{34}}$	$\sqrt{\frac{7}{19}}$	$\sqrt{\frac{33}{17(19)}}$

$\langle \vert \rangle$	$10 \to 8$	$10 \to 10$	$10 \to 12$	$12 \to 10$	$12 \to 12$
$\langle I_i 0; 20 \vert I_f 0\rangle$	$\sqrt{\frac{5(9)}{19(7)}}$	$-\sqrt{\frac{10(11)}{19(23)}}$	$\sqrt{\frac{66}{7(23)}}$	$\sqrt{\frac{3(66)}{23(25)}}$	$-\sqrt{\frac{4(13)}{9(23)}}$
$\langle I_i 2; 2,-2 \vert I_f 0\rangle$	$\sqrt{\frac{11}{7(19)}}$	$\sqrt{\frac{3(6)9}{19(23)}}$	$\sqrt{\frac{15}{14(23)}}$	$\sqrt{\frac{7(13)}{23(50)}}$	$\sqrt{\frac{77}{9(23)}}$
$\langle I_i 2; 20 \vert I_f 2\rangle$	$\sqrt{\frac{88}{19(15)}}$	$-\frac{98}{\sqrt{19(110)23}}$	$\sqrt{\frac{13(15)}{23(22)}}$	$\sqrt{\frac{7(9)13}{2(23)55}}$	$-\frac{8}{\sqrt{23(13)}}$
$\langle I_i 0; 22 \vert I_f 2\rangle$	$\sqrt{\frac{2}{3(19)}}$	$\sqrt{\frac{3(6)9}{19(23)}}$	$\sqrt{\frac{13}{6(23)}}$	$\sqrt{\frac{9}{230}}$	$\sqrt{\frac{77}{23(9)}}$

$$\langle 2_1 || \hat{T}^{(2)} || 4_2 \rangle = Q_0 \sqrt{9} \sqrt{\frac{5}{16\pi}} \left[\sqrt{\frac{5}{42}} \cos\Gamma_4 \sin(\gamma - \Gamma_2) + \sqrt{\frac{2}{7}} \cos\Gamma_2 \sin\Gamma_4 \cos\gamma - \sqrt{\frac{1}{126}} \sin\Gamma_2 \sin\Gamma_4 \sin\gamma \right]$$

$$\langle 4_1 || \hat{T}^{(2)} || 4_2 \rangle = Q_0 \sqrt{9} \sqrt{\frac{5}{16\pi}} \frac{3}{\sqrt{77}} \left[\sqrt{3} \cos(2\Gamma_4) \sin\gamma - \frac{1}{\sqrt{5}} \sin(2\Gamma_4) \cos\gamma \right]$$

$$\langle 6_1 || \hat{T}^{(2)} || 4_2 \rangle = Q_0 \sqrt{9} \sqrt{\frac{5}{16\pi}} \left[\sqrt{\frac{150}{330}} \cos\Gamma_6 \sin\Gamma_4 \cos\gamma + \sqrt{\frac{10}{330}} \cos\Gamma_6 \cos\Gamma_4 \sin\gamma - \sqrt{\frac{112}{330}} \sin\Gamma_6 \cos\Gamma_4 \cos\gamma - \sqrt{\frac{14}{99}} \sin\Gamma_6 \sin\Gamma_4 \sin\gamma \right]$$

$$\langle 4_1 || \hat{T}^{(2)} || 5_1 \rangle = Q_0 \sqrt{11} \sqrt{\frac{5}{16\pi}} \sqrt{\frac{7}{22}} \left[\cos\Gamma_4 \sin\gamma + \sqrt{\frac{3}{5}} \sin\Gamma_4 \cos\gamma \right]$$

$$\langle 6_1 || \hat{T}^{(2)} || 5_1 \rangle = Q_0 \sqrt{11} \sqrt{\frac{5}{16\pi}} \left[\sqrt{\frac{2}{11}} \cos\Gamma_6 \sin\gamma - \frac{8}{\sqrt{385}} \sin\Gamma_6 \cos\gamma \right]$$

Table 14: Clebsch-Gordan coefficients for $I_{\rm odd} \to I_{\rm even}$

$\langle \vert \rangle$	$3 \to 2$	$3 \to 4$	$5 \to 4$	$5 \to 6$	$7 \to 6$	$7 \to 8$
$\langle I_i 2; 2, -2 \vert I_f 0 \rangle$	$\sqrt{\frac{5}{14}}$	$\sqrt{\frac{1}{7}}$	$\sqrt{\frac{7}{22}}$	$\sqrt{\frac{2}{11}}$	$\sqrt{\frac{3}{10}}$	$\sqrt{\frac{1}{5}}$
$\langle I_i 2; 20 \vert I_f 2 \rangle$	$-\sqrt{\frac{5}{14}}$	$\sqrt{\frac{12}{35}}$	$-\sqrt{\frac{(3)(7)}{(5)(22)}}$	$\frac{8}{\sqrt{385}}$	$-\sqrt{\frac{3}{28}}$	$\sqrt{\frac{2}{21}}$

$\langle \vert \rangle$	$9 \to 8$	$9 \to 10$	$11 \to 10$	$11 \to 12$
$\langle I_i 2; 2, -2 \vert I_f 0 \rangle$	$\sqrt{\frac{11}{38}}$	$\frac{2}{\sqrt{19}}$	$\sqrt{\frac{13}{46}}$	$\sqrt{\frac{5}{23}}$
$\langle I_i 2; 20 \vert I_f 2 \rangle$	$-\sqrt{\frac{77}{19(10)6}}$	$\sqrt{\frac{64}{19(55)}}$	$-\sqrt{\frac{9(13)}{10(11)23}}$	$\sqrt{\frac{20(7)}{11(13)23}}$

Table 15: Clebsch-Gordan coefficients for $I_{\rm odd} \to I_{\rm odd}$

$\langle \vert \rangle$	$3 \to 3$	$5 \to 3$	$5 \to 5$	$7 \to 5$	$7 \to 7$
$\langle I_i 2; 20 \vert I_f 2 \rangle$	0	$\sqrt{\frac{21}{110}}$	$-\frac{6}{\sqrt{30(13)}}$	$\sqrt{\frac{24}{91}}$	$-\frac{22}{\sqrt{13(14)17}}$

$\langle \vert \rangle$	$9 \to 7$	$9 \to 9$	$11 \to 9$	$11 \to 11$
$\langle I_i 2; 20 \vert I_f 2 \rangle$	$\sqrt{\frac{7(55)}{17(19)4}}$	$-\frac{78}{\sqrt{17(90)21}}$	$\sqrt{\frac{18(13)12}{11(23)35}}$	$-\frac{4}{\sqrt{77}}$

$$\langle 4_1 || \hat{T}^{(2)} || 6_2 \rangle = Q_0 \sqrt{13} \sqrt{\frac{5}{16\pi}} \left[\sqrt{\frac{45}{(11)(13)}} \cos\Gamma_4 \sin\Gamma_6 \cos\gamma + \sqrt{\frac{14}{(11)(13)}} \cos\Gamma_4 \cos\Gamma_6 \sin\gamma \right.$$
$$\left. - \sqrt{\frac{12(14)}{5(11)(13)}} \sin\Gamma_4 \cos\Gamma_6 \cos\gamma - \sqrt{\frac{3}{(11)(13)}} \sin\Gamma_4 \sin\Gamma_6 \sin\gamma \right]$$

$$\langle 6_1 || \hat{T}^{(2)} || 6_2 \rangle = Q_0 \sqrt{13} \sqrt{\frac{5}{16\pi}} \left[\sqrt{\frac{60}{165}} \cos(2\Gamma_6) \sin\gamma - \frac{6}{\sqrt{165(42)}} \sin(2\Gamma_6) \cos\gamma \right]$$

$$\langle 8_1 || \hat{T}^{(2)} || 6_2 \rangle = Q_0 \sqrt{13} \sqrt{\frac{5}{16\pi}} \left[\sqrt{\frac{84}{195}} \cos\Gamma_8 \sin\Gamma_6 \cos\gamma + \sqrt{\frac{30}{195(4)}} \cos\Gamma_8 \cos\Gamma_6 \sin\gamma \right.$$
$$\left. - \sqrt{\frac{135}{364}} \sin\Gamma_8 \cos\Gamma_6 \cos\gamma - \sqrt{\frac{3}{26}} \sin\Gamma_8 \sin\Gamma_6 \sin\gamma \right]$$

$$\langle 6_1 || \hat{T}^{(2)} || 7_1 \rangle = Q_0 \sqrt{15} \sqrt{\frac{5}{16\pi}} \sqrt{\frac{3}{10}} \left[\cos\Gamma_6 \sin\gamma + \sqrt{\frac{5}{14}} \sin\Gamma_6 \cos\gamma \right]$$

$$\langle 8_1 || \hat{T}^{(2)} || 7_1 \rangle = Q_0 \sqrt{15} \sqrt{\frac{5}{16\pi}} \sqrt{\frac{1}{5}} \left[\cos\Gamma_8 \sin\gamma - \sqrt{\frac{10}{21}} \sin\Gamma_8 \cos\gamma \right]$$

Table 16: Clebsch-Gordan coefficients for $I_{\rm even} \to I_{\rm odd}$

$\langle \vert \rangle$	$4 \to 3$	$6 \to 5$	$8 \to 7$	$10 \to 9$	$12 \to 11$
$\langle I_i 2; 20 \vert I_f 2\rangle$	$-\frac{2}{\sqrt{15}}$	$-\frac{8}{\sqrt{455}}$	$-\sqrt{\frac{10}{(7)(17)}}$	$-\sqrt{\frac{64}{33(35)}}$	$-\sqrt{\frac{28}{55(13)}}$
$\langle I_i 0; 22 \vert I_f 2\rangle$	$-\frac{1}{3}$	$-\sqrt{\frac{2}{13}}$	$-\sqrt{\frac{3}{17}}$	$-\frac{2}{\sqrt{21}}$	$-\sqrt{\frac{1}{5}}$

$$\begin{aligned}
\langle 6_1||\hat{T}^{(2)}||8_2\rangle &= Q_0\sqrt{17}\sqrt{\frac{5}{16\pi}}\left[\sqrt{\frac{28}{5(17)}}\cos\Gamma_6\sin\Gamma_8\cos\gamma + \sqrt{\frac{18}{(51)(4)}}\cos\Gamma_6\cos\Gamma_8\sin\gamma\right.\\
&\left. - \sqrt{\frac{135}{28(17)}}\sin\Gamma_6\cos\Gamma_8\cos\gamma - \sqrt{\frac{1}{34}}\sin\Gamma_6\sin\Gamma_8\sin\gamma\right]\\
\langle 8_1||\hat{T}^{(2)}||8_2\rangle &= Q_0\sqrt{17}\sqrt{\frac{5}{16\pi}}\left[\sqrt{\frac{7}{19}}\cos(2\Gamma_8)\sin\gamma - \frac{1}{2}\sqrt{\frac{38}{5415}}\sin(2\Gamma_8)\cos\gamma\right]\\
\langle 10_1||\hat{T}^{(2)}||8_2\rangle &= Q_0\sqrt{17}\sqrt{\frac{5}{16\pi}}\left[\sqrt{\frac{135}{323}}\cos\Gamma_{10}\sin\Gamma_8\cos\gamma + \sqrt{\frac{14}{323}}\cos\Gamma_{10}\cos\Gamma_8\sin\gamma\right.\\
&\left. - \sqrt{\frac{8(77)}{(19)(85)}}\sin\Gamma_{10}\cos\Gamma_8\cos\gamma - \sqrt{\frac{33}{323}}\sin\Gamma_{10}\sin\Gamma_8\sin\gamma\right]
\end{aligned}$$

$$\begin{aligned}
\langle 8_1||\hat{T}^{(2)}||9_1\rangle &= Q_0\sqrt{19}\sqrt{\frac{5}{16\pi}}\left[\sqrt{\frac{11}{38}}\cos\Gamma_8\sin\gamma + \sqrt{\frac{77}{19(60)}}\sin\Gamma_8\cos\gamma\right]\\
\langle 10_1||\hat{T}^{(2)}||9_1\rangle &= Q_0\sqrt{19}\sqrt{\frac{5}{16\pi}}\left[\frac{2}{\sqrt{19}}\cos\Gamma_{10}\sin\gamma - \sqrt{\frac{64}{19(55)}}\sin\Gamma_{10}\cos\gamma\right]
\end{aligned}$$

$$\begin{aligned}
\langle 8_1||\hat{T}^{(2)}||10_2\rangle &= Q_0\sqrt{21}\sqrt{\frac{5}{16\pi}}\left[\sqrt{\frac{5(9)}{19(7)}}\cos\Gamma_8\sin\Gamma_{10}\cos\gamma + \sqrt{\frac{11}{(7)(19)}}\cos\Gamma_8\cos\Gamma_{10}\sin\gamma\right.\\
&\left. - \sqrt{\frac{88}{19(15)}}\sin\Gamma_8\cos\Gamma_{10}\cos\gamma - \sqrt{\frac{2}{3(19)}}\sin\Gamma_8\sin\Gamma_{10}\sin\gamma\right]\\
\langle 10_1||\hat{T}^{(2)}||10_2\rangle &= Q_0\sqrt{21}\sqrt{\frac{5}{16\pi}}\left[\sqrt{\frac{3(6)9}{19(23)}}\cos(2\Gamma_{10})\sin\gamma - \frac{6}{\sqrt{19(110)23}}\sin(2\Gamma_{10})\cos\gamma\right]\\
\langle 12_1||\hat{T}^{(2)}||10_2\rangle &= Q_0\sqrt{21}\sqrt{\frac{5}{16\pi}}\left[\sqrt{\frac{66}{161}}\cos\Gamma_{12}\sin\Gamma_{10}\cos\gamma + \sqrt{\frac{15}{14(23)}}\cos\Gamma_{12}\cos\Gamma_{10}\sin\gamma\right.\\
&\left. - \sqrt{\frac{13(15)}{(23)(22)}}\sin\Gamma_{12}\cos\Gamma_{10}\cos\gamma - \sqrt{\frac{13}{6(23)}}\sin\Gamma_{12}\sin\Gamma_{10}\sin\gamma\right]
\end{aligned}$$

$$\langle 10_1||\hat{T}^{(2)}||11_1\rangle = Q_0\sqrt{23}\sqrt{\frac{5}{16\pi}}\left[\sqrt{\frac{13}{46}}\cos\Gamma_{10}\sin\gamma + \sqrt{\frac{9(13)}{23(110)}}\sin\Gamma_{10}\cos\gamma\right]$$

$$\langle 12_1||\hat{T}^{(2)}||11_1\rangle = Q_0\sqrt{23}\sqrt{\frac{5}{16\pi}}\left[\sqrt{\frac{5}{23}}\cos\Gamma_{12}\sin\gamma - \sqrt{\frac{20(7)}{11(13)23}}\sin\Gamma_{12}\cos\gamma\right]$$

$$\langle 10_1||\hat{T}^{(2)}||12_2\rangle = Q_0\sqrt{25}\sqrt{\frac{5}{16\pi}}\left[\sqrt{\frac{3(66)}{23(25)}}\cos\Gamma_{10}\sin\Gamma_{12}\cos\gamma + \sqrt{\frac{91}{1150}}\cos\Gamma_{10}\cos\Gamma_{12}\sin\gamma\right.$$
$$\left. - \sqrt{\frac{(63)13}{(46)55}}\sin\Gamma_{10}\cos\Gamma_{12}\cos\gamma - \sqrt{\frac{9}{230}}\sin\Gamma_{10}\sin\Gamma_{12}\sin\gamma\right]$$

$$\langle 12_1||\hat{T}^{(2)}||12_2\rangle = Q_0\sqrt{25}\sqrt{\frac{5}{16\pi}}\left[\sqrt{\frac{77}{9(23)}}\cos(2\Gamma_{12})\sin\gamma - \frac{1}{\sqrt{9(13)23}}\sin(2\Gamma_{12})\cos\gamma\right]$$

ground-ground:

$$\langle 0_1||\hat{T}^{(2)}||2_1\rangle = Q_0\sqrt{5}\sqrt{\frac{1}{16\pi}}\cos(\gamma+\Gamma_2)$$

$$\langle 2_1||\hat{T}^{(2)}||4_1\rangle = Q_0\sqrt{9}\sqrt{\frac{5}{16\pi}}\left[\sqrt{\frac{2}{7}}\cos\Gamma_2\cos\Gamma_4\cos\gamma - \sqrt{\frac{5}{42}}\sin(\gamma-\Gamma_2)\sin\Gamma_4\right.$$
$$\left. - \sqrt{\frac{1}{126}}\sin\Gamma_2\cos\Gamma_4\sin\gamma\right]$$

$$\langle 4_1||\hat{T}^{(2)}||6_1\rangle = Q_0\sqrt{13}\sqrt{\frac{5}{16\pi}}\left[\sqrt{\frac{45}{11(13)}}\cos\Gamma_4\cos\Gamma_6\cos\gamma - \sqrt{\frac{14}{11(13)}}\cos\Gamma_4\sin\Gamma_6\sin\gamma\right.$$
$$\left. + \sqrt{\frac{12(14)}{5(11)(13)}}\sin\Gamma_4\sin\Gamma_6\cos\gamma - \sqrt{\frac{3}{11(13)}}\sin\Gamma_4\cos\Gamma_6\sin\gamma\right]$$

$$\langle 6_1||\hat{T}^{(2)}||8_1\rangle = Q_0\sqrt{17}\sqrt{\frac{5}{16\pi}}\left[\sqrt{\frac{28}{5(17)}}\cos\Gamma_6\cos\Gamma_8\cos\gamma - \frac{1}{2}\sqrt{\frac{18}{51}}\cos\Gamma_6\sin\Gamma_8\sin\gamma\right.$$
$$\left. + \sqrt{\frac{135}{28(17)}}\sin\Gamma_6\sin\Gamma_8\cos\gamma - \sqrt{\frac{1}{34}}\sin\Gamma_6\cos\Gamma_8\sin\gamma\right]$$

$$\langle 8_1||\hat{T}^{(2)}||10_1\rangle = Q_0\sqrt{21}\sqrt{\frac{5}{16\pi}}\left[\sqrt{\frac{5(9)}{7(19)}}\cos\Gamma_8\cos\Gamma_{10}\cos\gamma - \sqrt{\frac{11}{7(19)}}\cos\Gamma_8\sin\Gamma_{10}\sin\gamma\right.$$
$$\left. + \sqrt{\frac{88}{19(15)}}\sin\Gamma_8\sin\Gamma_{10}\cos\gamma - \sqrt{\frac{2}{3(19)}}\sin\Gamma_8\cos\Gamma_{10}\sin\gamma\right]$$

$$\langle 10_1||\hat{T}^{(2)}||12_1\rangle = Q_0\sqrt{25}\sqrt{\frac{5}{16\pi}}\left[\sqrt{\frac{3(66)}{23(25)}}\cos\Gamma_{10}\cos\Gamma_{12}\cos\gamma - \sqrt{\frac{91}{1150}}\cos\Gamma_{10}\sin\Gamma_{12}\sin\gamma\right.$$
$$\left. + \sqrt{\frac{63(13)}{46(55)}}\sin\Gamma_{10}\sin\Gamma_{12}\cos\gamma - \sqrt{\frac{9}{230}}\sin\Gamma_{10}\cos\Gamma_{12}\sin\gamma\right]$$

$\underline{\gamma\text{-}\gamma}$:

$$\langle 2_2||\hat{T}^{(2)}||3_1\rangle = -Q_0\sqrt{7}\sqrt{\frac{5}{16\pi}}\sqrt{\frac{5}{14}}\cos(\gamma+\Gamma_2)$$

$$\begin{aligned}\langle 2_2||\hat{T}^{(2)}||4_2\rangle &= Q_0\sqrt{9}\sqrt{\frac{5}{16\pi}}\left[\sqrt{\frac{2}{7}}\sin\Gamma_2\sin\Gamma_4\cos\gamma+\sqrt{\frac{5}{42}}\cos\Gamma_4\cos(\gamma-\Gamma_2)\right.\\ &\quad\left.+\sqrt{\frac{1}{126}}\cos\Gamma_2\sin\Gamma_4\sin\gamma\right]\\ \langle 3_1||\hat{T}^{(2)}||4_2\rangle &= -Q_0\sqrt{9}\sqrt{\frac{5}{16\pi}}\frac{1}{3}\left[2\sqrt{\frac{3}{5}}\cos\Gamma_4\cos\gamma+\sin\Gamma_4\sin\gamma\right]\end{aligned}$$

$$\begin{aligned}\langle 3_1||\hat{T}^{(2)}||5_1\rangle &= Q_0\sqrt{11}\sqrt{\frac{5}{16\pi}}\sqrt{\frac{21}{110}}\cos\gamma\\ \langle 4_2||\hat{T}^{(2)}||5_1\rangle &= Q_0\sqrt{11}\sqrt{\frac{5}{16\pi}}\left[\sqrt{\frac{7}{22}}\sin\Gamma_4\sin\gamma-\sqrt{\frac{21}{110}}\cos\Gamma_4\cos\gamma\right]\end{aligned}$$

$$\begin{aligned}\langle 4_2||\hat{T}^{(2)}||6_2\rangle &= Q_0\sqrt{13}\sqrt{\frac{5}{16\pi}}\left[\sqrt{\frac{45}{11(13)}}\sin\Gamma_4\sin\Gamma_6\cos\gamma+\sqrt{\frac{14}{11(13)}}\sin\Gamma_4\cos\Gamma_6\sin\gamma\right.\\ &\quad\left.+\sqrt{\frac{12(14)}{5(11)(13)}}\cos\Gamma_4\cos\Gamma_6\cos\gamma+\sqrt{\frac{3}{11(13)}}\cos\Gamma_4\sin\Gamma_6\sin\gamma\right]\\ \langle 5_1||\hat{T}^{(2)}||6_2\rangle &= -Q_0\sqrt{13}\sqrt{\frac{5}{16\pi}}\sqrt{\frac{2}{13}}\left[8\sqrt{\frac{1}{70}}\cos\Gamma_6\cos\gamma+\sin\Gamma_6\sin\gamma\right]\end{aligned}$$

$$\begin{aligned}\langle 5_1||\hat{T}^{(2)}||7_1\rangle &= Q_0\sqrt{15}\sqrt{\frac{5}{16\pi}}\sqrt{\frac{24}{91}}\cos\gamma\\ \langle 6_2||\hat{T}^{(2)}||7_1\rangle &= Q_0\sqrt{15}\sqrt{\frac{5}{16\pi}}\left[\sqrt{\frac{3}{10}}\sin\Gamma_6\sin\gamma-\sqrt{\frac{3}{28}}\cos\Gamma_6\cos\gamma\right]\end{aligned}$$

$$\begin{aligned}\langle 6_2||\hat{T}^{(2)}||8_2\rangle &= Q_0\sqrt{17}\sqrt{\frac{5}{16\pi}}\left[\sqrt{\frac{28}{5(17)}}\sin\Gamma_6\sin\Gamma_8\cos\gamma+\sqrt{\frac{9}{2(51)}}\sin\Gamma_6\cos\Gamma_8\sin\gamma\right.\\ &\quad\left.+\sqrt{\frac{135}{28(17)}}\cos\Gamma_6\cos\Gamma_8\cos\gamma+\sqrt{\frac{1}{34}}\cos\Gamma_6\sin\Gamma_8\sin\gamma\right]\\ \langle 7_1||\hat{T}^{(2)}||8_2\rangle &= -Q_0\sqrt{17}\sqrt{\frac{5}{16\pi}}\sqrt{\frac{3}{17}}\left[\sqrt{\frac{10}{21}}\cos\Gamma_8\cos\gamma+\sin\Gamma_8\sin\gamma\right]\end{aligned}$$

$$\langle 7_1||\hat{T}^{(2)}||9_1\rangle = Q_0\sqrt{19}\sqrt{\frac{5}{16\pi}}\sqrt{\frac{7(55)}{17(19)4}}\cos\gamma$$

$$\langle 8_2||\hat{T}^{(2)}||9_1\rangle = Q_0\sqrt{19}\sqrt{\frac{5}{16\pi}}\left[\sqrt{\frac{11}{38}}\sin\Gamma_8\sin\gamma - \sqrt{\frac{77}{19(60)}}\cos\Gamma_8\cos\gamma\right]$$

$$\begin{aligned}\langle 8_2||\hat{T}^{(2)}||10_2\rangle = Q_0\sqrt{21}\sqrt{\frac{5}{16\pi}}\Bigg[&\sqrt{\frac{5(9)}{7(19)}}\sin\Gamma_8\sin\Gamma_{10}\cos\gamma + \sqrt{\frac{11}{7(19)}}\sin\Gamma_8\cos\Gamma_{10}\sin\gamma \\ &+ \sqrt{\frac{88}{19(15)}}\cos\Gamma_8\cos\Gamma_{10}\cos\gamma + \sqrt{\frac{2}{3(19)}}\cos\Gamma_8\sin\Gamma_{10}\sin\gamma\Bigg]\end{aligned}$$

$$\langle 9_1||\hat{T}^{(2)}||10_2\rangle = -Q_0\sqrt{21}\sqrt{\frac{5}{16\pi}}\left[\sqrt{\frac{64}{33(35)}}\cos\Gamma_{10}\cos\gamma + \frac{2}{\sqrt{21}}\sin\Gamma_{10}\sin\gamma\right]$$

$$\langle 9_1||\hat{T}^{(2)}||11_1\rangle = Q_0\sqrt{23}\sqrt{\frac{5}{16\pi}}\sqrt{\frac{18(13)12}{11(23)35}}\cos\gamma$$

$$\langle 10_2||\hat{T}^{(2)}||11_1\rangle = Q_0\sqrt{23}\sqrt{\frac{5}{16\pi}}\left[\sqrt{\frac{13}{46}}\sin\Gamma_{10}\sin\gamma - \sqrt{\frac{9(13)}{10(11)23}}\cos\Gamma_{10}\cos\gamma\right]$$

$$\begin{aligned}\langle 10_2||\hat{T}^{(2)}||12_2\rangle = Q_0\sqrt{25}\sqrt{\frac{5}{16\pi}}\Bigg[&\sqrt{\frac{3(66)}{23(25)}}\sin\Gamma_{10}\sin\Gamma_{12}\cos\gamma + \sqrt{\frac{91}{1150}}\sin\Gamma_{10}\cos\Gamma_{12}\sin\gamma \\ &+ \sqrt{\frac{(63)13}{46(55)}}\cos\Gamma_{10}\cos\Gamma_{12}\cos\gamma + \sqrt{\frac{9}{230}}\cos\Gamma_{10}\sin\Gamma_{12}\sin\gamma\Bigg]\end{aligned}$$

$$\langle 11_1||\hat{T}^{(2)}||12_2\rangle = -Q_0\sqrt{25}\sqrt{\frac{5}{16\pi}}\left[\sqrt{\frac{28}{13(55)}}\cos\Gamma_{12}\cos\gamma + \sqrt{\frac{1}{5}}\sin\Gamma_{12}\sin\gamma\right]$$

diagonal matrix elements:

$$
\begin{aligned}
T(2_1), T(2_2) &= \mp Q_0\sqrt{5}\sqrt{\frac{5}{16\pi}}\sqrt{\frac{2}{7}}\cos(\gamma - 2\Gamma_2) \\
T(3_1) &= 0 \\
T(4_1), T(4_2) &= \mp Q_0\sqrt{9}\sqrt{\frac{5}{16\pi}}\left[\sqrt{\frac{27}{77}}\sin(2\Gamma_4)\sin\gamma + \frac{3}{\sqrt{385}}\cos(2\Gamma_4)\cos\gamma \pm \frac{7}{\sqrt{385}}\cos\gamma\right] \\
T(5_1) &= -Q_0\sqrt{11}\sqrt{\frac{5}{16\pi}}\frac{6}{\sqrt{30(13)}}\cos\gamma \\
T(6_1), T(6_2) &= \mp Q_0\sqrt{13}\sqrt{\frac{5}{16\pi}}\left[\sqrt{\frac{60}{165}}\sin(2\Gamma_6)\sin\gamma + \frac{6}{\sqrt{165(42)}}\cos(2\Gamma_6)\cos\gamma\right. \\
&\quad \left. \pm \frac{36}{\sqrt{165(42)}}\cos\gamma\right] \\
T(7_1) &= -Q_0\sqrt{15}\sqrt{\frac{5}{16\pi}}\frac{22}{\sqrt{13(14)17}}\cos\gamma \\
T(8_1), T(8_2) &= \mp Q_0\sqrt{17}\sqrt{\frac{5}{16\pi}}\left[\sqrt{\frac{7}{19}}\sin(2\Gamma_8)\sin\gamma + \frac{1}{\sqrt{570}}\cos(2\Gamma_8)\cos\gamma \pm \frac{11}{\sqrt{570}}\cos\gamma\right] \\
T(9_1) &= -Q_0\sqrt{19}\sqrt{\frac{5}{16\pi}}\frac{78}{\sqrt{17(90)21}}\cos\gamma \\
T(10_1), T(10_2) &= \mp Q_0\sqrt{21}\sqrt{\frac{5}{16\pi}}\left[\sqrt{\frac{3(6)9}{19(23)}}\sin(2\Gamma_{10})\sin\gamma + \frac{6}{\sqrt{19(23)110}}\cos(2\Gamma_{10})\cos\gamma\right. \\
&\quad \left. \pm \frac{104}{\sqrt{19(23)110}}\cos\gamma\right] \\
T(11_1) &= -Q_0\sqrt{23}\sqrt{\frac{5}{16\pi}}\frac{4}{\sqrt{77}}\cos\gamma \\
T(12_1), T(12_2) &= \mp Q_0\sqrt{25}\sqrt{\frac{5}{16\pi}}\left[\sqrt{\frac{77}{9(23)}}\sin(2\Gamma_{12})\sin\gamma + \frac{1}{\sqrt{9(23)13}}\cos(2\Gamma_{12})\cos\gamma\right. \\
&\quad \left. \pm \frac{25}{\sqrt{9(23)13}}\cos\gamma\right]
\end{aligned}
$$

A.1 Useful Fitting Relations

$$Q_0 = \sqrt{\frac{16\pi}{5}}\sqrt{\langle 0_1||\hat{T}^{(2)}||2_2\rangle^2 + \langle 0_1||\hat{T}^{(2)}||2_1\rangle^2}$$

$$\gamma + \Gamma_2 = \arcsin\left(\frac{1}{\sqrt{1+\left[\frac{\langle 0_1||\hat{T}^{(2)}||2_1\rangle}{\langle 0_1||\hat{T}^{(2)}||2_2\rangle}\right]^2}}\right) = \arctan\left(\frac{\langle 0_1||\hat{T}^{(2)}||2_2\rangle}{\langle 0_1||\hat{T}^{(2)}||2_1\rangle}\right)$$

$$= \arcsin\left(\frac{\sqrt{\frac{14}{35}}\langle 2_1||\hat{T}^{(2)}||3_1\rangle}{\sqrt{\langle 0_1||\hat{T}^{(2)}||2_2\rangle^2 + \langle 0_1||\hat{T}^{(2)}||2_1\rangle^2}}\right)$$

$$= \arccos\left(-\frac{\sqrt{\frac{14}{35}}\langle 2_2||\hat{T}^{(2)}||3_1\rangle}{\sqrt{\langle 0_1||\hat{T}^{(2)}||2_2\rangle^2 + \langle 0_1||\hat{T}^{(2)}||2_1\rangle^2}}\right)$$

$$\gamma - 2\Gamma_2 = \arcsin\left(\sqrt{\frac{7}{10}}\frac{1}{\sqrt{\left[\frac{\langle 0_1||\hat{T}^{(2)}||2_2\rangle}{\langle 2_1||\hat{T}^{(2)}||2_2\rangle}\right]^2 + \left[\frac{\langle 0_1||\hat{T}^{(2)}||2_1\rangle}{\langle 2_1||\hat{T}^{(2)}||2_2\rangle}\right]^2}}\right)$$

$$= \arctan\left(\mp\frac{\langle 2_1||\hat{T}^{(2)}||2_2\rangle}{T(2_1), T(2_2)}\right)$$

$$= \arccos\left(\mp\frac{\sqrt{\frac{7}{10}}T(2_1), T(2_2)}{\sqrt{\langle 0_1||\hat{T}^{(2)}||2_2\rangle^2 + \langle 0_1||\hat{T}^{(2)}||2_1\rangle^2}}\right)$$

A.2 Additional Relations

$$\frac{\langle 0_1||\hat{T}^{(2)}||2_2\rangle}{\langle 0_1||\hat{T}^{(2)}||2_1\rangle} = \tan(\gamma+\Gamma_2)$$
$$\frac{\langle 2_1||\hat{T}^{(2)}||3_1\rangle}{\langle 0_1||\hat{T}^{(2)}||2_1\rangle} = \sqrt{\frac{5}{2}}\tan(\gamma+\Gamma_2)$$
$$\frac{\langle 0_1||\hat{T}^{(2)}||2_2\rangle}{\langle 2_2||\hat{T}^{(2)}||3_1\rangle} = -\sqrt{\frac{2}{5}}\tan(\gamma+\Gamma_2)$$
$$\frac{\langle 2_1||\hat{T}^{(2)}||3_1\rangle}{\langle 2_2||\hat{T}^{(2)}||3_1\rangle} = -\tan(\gamma+\Gamma_2)$$
$$\frac{\langle 2_1||\hat{T}^{(2)}||3_1\rangle}{\langle 0_1||\hat{T}^{(2)}||2_2\rangle} = \sqrt{\frac{5}{2}}$$
$$\frac{\langle 2_2||\hat{T}^{(2)}||3_1\rangle}{\langle 0_1||\hat{T}^{(2)}||2_1\rangle} = -\sqrt{\frac{5}{2}}$$
$$\frac{{}_{\rm odd}\langle I_1'||\hat{T}^{(2)}||I_1\rangle_{\rm odd}}{{}_{\rm odd}\langle I_1'''||\hat{T}^{(2)}||I_1''\rangle_{\rm odd}} = Constant$$
$$\frac{\langle 2_1||\hat{T}^{(2)}||3_1\rangle}{\langle 2_2||\hat{T}^{(2)}||3_1\rangle}\frac{\langle 0_1||\hat{T}^{(2)}||2_1\rangle}{\langle 0_1||\hat{T}^{(2)}||2_2\rangle} = -1$$
$$\frac{\langle 2_1||\hat{T}^{(2)}||3_1\rangle}{\langle 0_1||\hat{T}^{(2)}||2_1\rangle}\frac{\langle 2_2||\hat{T}^{(2)}||3_1\rangle}{\langle 0_1||\hat{T}^{(2)}||2_2\rangle} = -\frac{5}{2}$$

$$T(3_1) = 0$$

$$T(I_1)_{\rm odd} = -Constant\, Q_0\cos\gamma$$
$$\frac{T(I_1)_{\rm odd}}{T(I_1')_{\rm odd}} = Constant$$
$$\frac{T(2_1)}{T(2_2)} = -1$$

$$T(2_1)+T(2_2) = 0$$

$$T(4_1)+T(4_2) = -0.675Q_0\cos\gamma$$

$$T(6_1)+T(6_2) = -0.984Q_0\cos\gamma$$

$$T(8_1)+T(8_2) = -1.198Q_0\cos\gamma$$

$$Trace\{T(I)\}_{I=2\rightarrow I=8} = -2.857Q_0\cos\gamma$$

APPENDIX B

WIGNER-ECKART THEOREM

The Wigner-Eckart theorem is given in the laboratory frame by

$$\langle \alpha' J' M' | \hat{T}^{(k)}_{\pm\mu} | \alpha J M \rangle = (-1)^{J'-M'} \begin{pmatrix} J' & k & J \\ M' & \pm\mu & M \end{pmatrix} \langle \alpha' J' || \hat{T}^{(k)} || \alpha J \rangle$$

$$= \frac{\langle JM; k, \pm\mu | J' M' \rangle}{\sqrt{2J'+1}} \langle \alpha' J' || \hat{T}^{(k)} || \alpha J \rangle$$

where $\hat{T}^{(k)}_{\pm\mu} \propto Y_{k,\pm\mu}$ (a spherical harmonic). The "reduced" matrix element, $\langle \alpha' J' || \hat{T}^{(k)} || \alpha J \rangle$, is independent of the projection quantum numbers, M and M', and it is rotationally invariant. The expression in curved brackets is a Wigner-3j symbol (useful for permuting the labels) and it is related to the Clebsch-Gordan coefficient by

$$\begin{pmatrix} j_1 & j_2 & j_3 \\ m_1 & m_2 & m_3 \end{pmatrix} = (-1)^{j_1 - j_2 - m_3} \frac{\langle j_1 m_1; j_2 m_2 | j_3, -m_3 \rangle}{\sqrt{2j_3+1}};$$

and

$$\begin{pmatrix} j_1 & j_2 & j_3 \\ m_1 & m_2 & m_3 \end{pmatrix} = (-1)^{j_1+j_2+j_3} \begin{pmatrix} j_3 & j_2 & j_1 \\ m_3 & m_2 & m_1 \end{pmatrix}.$$

For nuclei, the system is modeled in the intrinsic frame (body frame) and it is rotated to the laboratory frame for matrix elements in that frame (e.g., $\Sigma\, T^{(k)}_{\pm q} D^{(k)}_{\mu q}$ where q is the intrinsic frame index). The rotor state and quadrupole operator are represented in general to carry both indices (laboratory and body frame) in the following way (see [7] and [8] for details)

$$|\alpha J M K\rangle \rightarrow \sqrt{\frac{2J+1}{8\pi^2}} \Phi(\alpha) D^{(J)}_{MK} \ , \quad \hat{T}^{(2)}_{\mu q} \rightarrow Q_0 \sqrt{\frac{5}{16\pi}} D^{(2)}_{\mu q} \ , \quad D^{*(J)}_{MK} = (-1)^{M+K} D^{(J)}_{-M-K} \ ,$$

where $\Phi(\alpha)$ is a separable factor in the wavefunction that is dependent on the internal degrees of freedom of the nucleus (we assume an adiabatic rotor, so this always integrates

to unity separately) and $Q_0\sqrt{\frac{5}{16\pi}}$ normalizes the quadrupole operator and scales it to some given strength.

The Wigner-Eckart theorem takes on a different form when both the laboratory and body frame indices are used (Wigner-D functions). For pure, unsymmetrized states,

$$\langle \alpha' J' M' K' | \hat{T}^{(2)}_{\pm\mu\pm q} | \alpha J M K \rangle = \frac{\langle JM; 2, \pm\mu | J' M' \rangle}{\sqrt{2J'+1}} \langle \alpha' J' K' || \hat{T}^{(2)}_{\pm q} || \alpha J K \rangle$$

and the reduced matrix element is

$$\langle \alpha' J' K' || \hat{T}^{(2)}_{\pm q} || \alpha J K \rangle = Q_0 \sqrt{\frac{5}{16\pi}} \sqrt{2J+1} \langle JK; 2, \pm q | J' K' \rangle,$$

where it has a Clebsch-Gordan coefficient since our operator is a Wigner-D function (laboratory and body frame indices) as opposed to a spherical harmonic. This can be obtained with the following relation

$$\frac{1}{8\pi^2} \int_0^{2\pi} \int_0^{\pi} \int_0^{2\pi} D^{(j_1)}_{m_1' m_1} D^{(j_2)}_{m_2' m_2} D^{(j_3)}_{m_3' m_3} d\alpha \sin\beta \, d\beta \, d\gamma = \begin{pmatrix} j_1 & j_2 & j_3 \\ m_1' & m_2' & m_3' \end{pmatrix} \begin{pmatrix} j_1 & j_2 & j_3 \\ m_1 & m_2 & m_3 \end{pmatrix}.$$

For example:

$$\begin{aligned} \langle \alpha' J' M' K' | \hat{T}^{(2)}_{\pm\mu\pm q} | \alpha J M K \rangle &= Q_0 \sqrt{\frac{5}{16\pi}} \frac{\sqrt{(2J'+1)(2J+1)}}{8\pi^2} \times \\ &\int_0^{2\pi} \int_0^{\pi} \int_0^{2\pi} D^{*(J')}_{M'K'} D^{(2)}_{\pm\mu\pm q} D^{(J)}_{MK} d\alpha \sin\beta \, d\beta \, d\gamma \\ &= Q_0 \sqrt{\frac{5}{16\pi}} \frac{\sqrt{2J+1}}{\sqrt{2J'+1}} \langle JM; 2, \pm\mu | J' M' \rangle \langle JK; 2, \pm q | J' K' \rangle \end{aligned}$$

Additional Comments: The "reduced" matrix elment, $\langle \alpha' J' K' || \hat{T}^{(2)}_{\pm q} || \alpha J K \rangle$, is not hermitian. Due to the Clebsch-Gordan coefficient, the even-odd or odd-even elements are anti-symmetric, e.g., $\langle I_f || \hat{T}^{(2)}_{\pm q} || I_i \rangle = (-1)^{I_f - I_i} \langle I_i || \hat{T}^{(2)}_{\pm q} || I_f \rangle$. Also, the reduced matrix elements are not independent of the projection quantum numbers since we are dealing with Wigner-D functions as opposed to the spherical harmonics.

APPENDIX C

QUADRUPOLE DEFORMATIONS

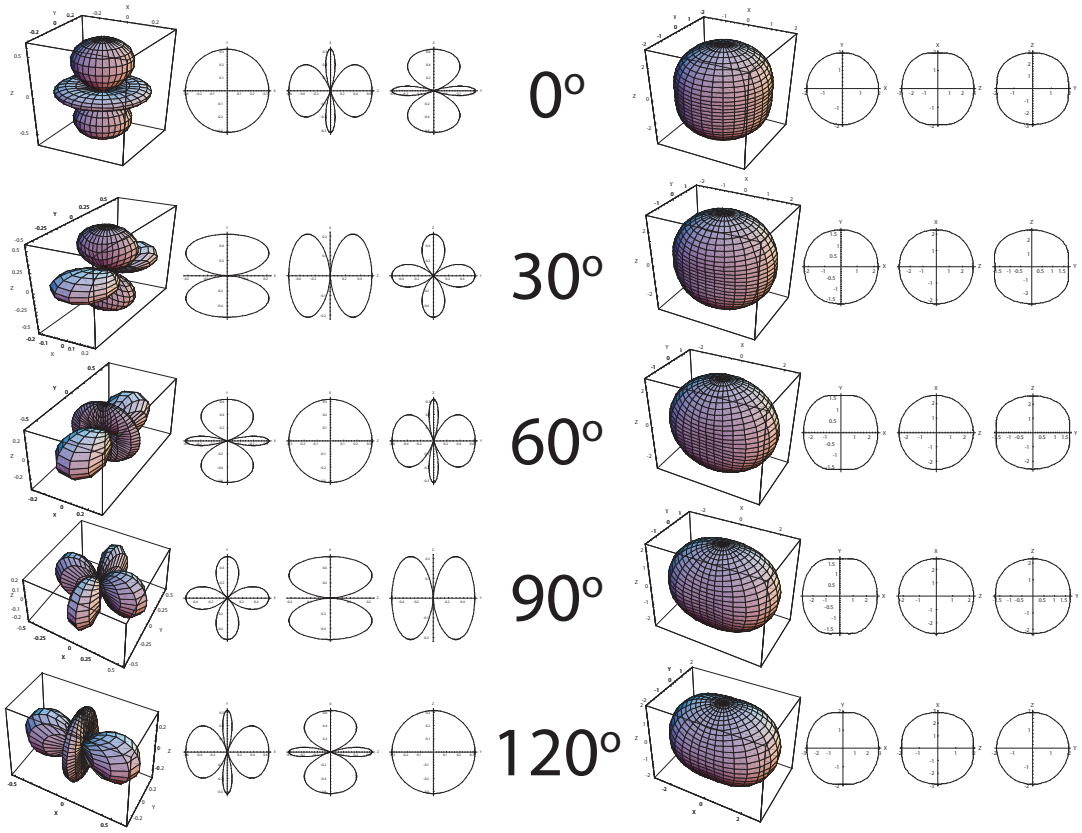

Figure 29: Quadrupole deformations of a sphere as a function of the asymmetry angle γ.

REFERENCES

[1] N. Bohr, Nature **137**, 344 (1936);
N. Bohr and F. Kalckar, K. Dan. Vidensk. Selsk. Mat.-Fys. Medd. **14**, No. 10 (1937);
N. Bohr and J.A. Wheeler, Phys. Rev. **56**, 426 (1939).

[2] J. Rainwater, Phys. Rev. **79**, 432 (1950);
J. Rainwater, Rev. Mod. Phys. **48**, 385 (1976).

[3] A. Bohr, Kongl. Dan. Vid. Selsk. Mat.-fys. Medd. **26**, no. 14 (1952);
A. Bohr, Rev. Mod. Phys. **48**, 365 (1976).

[4] R.L. Kronig and I.I. Rabi, Phys. Rev. **29**, 262 (1927).

[5] G. Alaga, K. Alder, A. Bohr, and B.R. Mottelson, Mat. Fys. Medd. Dan. Vid. Selsk. **29**, no. 9 (1955).

[6] V.M. Mikhailov, Izv. Akad. Nauk SSSR, ser. fiz. **28**, 308 (1964) [transl. Bull. Acad. Sci. USSR, phys. ser. **28**, 225]; *ibid.* **30**, 1334 (1966) [transl. **30**, 1392].

[7] A. Bohr and B.R. Mottelson, Nuclear Structure, Vol. 1 and Vol. 2 (W.A. Benjamin, Inc., Reading, Ma, 1975).

[8] A.S. Davydov and G.F. Filippov, Nucl. Phys. **8**, 237 (1958).

[9] A.S. Davydov, At. Energy Rev. **6**, 3 (1968).

[10] M. Goldhaber and A.W. Sunyar, Phys. Rev. **83**, 906 (1951).

[11] Online-ENSDF, http://ie.lbl.gov/databases/ensdfserve.html, (2002).

[12] W.D. Kulp and J.L. Wood, GTNDSE: the GA Tech nuclear data search engine, American Physical Society, Division of Nuclear Physics Fall Meeting, October 30 - November 1, 2003, Tucson, Arizona, MEETING ID: DNP03, abstract #GD.015.

[13] See E.M.O. Bernardes, J.U. Delgado, L. Tauhata, C.J. da Silva, A. Iwahara, R. Poledna, and A.S. Paschoa, Appl. Radiat. Isotop. **56**, 157 (2002) and references therein.

[14] W.D. Kulp, J.M. Allmond, P. Hatcher, and J.L. Wood, Phys. Rev. C **73**, 014308 (2006).

[15] J.P. Martin, D.C. Radford, *et al.*, Nucl. Instrum. Methods Phys. Res. A **257**, 301 (1987).

[16] W.D. Kulp, Ph.D. dissertation, Georgia Institute of Technology, (2001).

[17] E.N. Shurshikov and N.V. Timofeeva, Nucl. Data Sheets **67**, 45 (1992) (note: there is a decimal point error in the listing of the 305 keV line intensity).

[18] W.D. Hamilton, H. Marshak, and K. Kumar, J. Phys. G **16**, L219 (1990).

[19] J. Loats, Ph.D. dissertation, Oregon State Univ., (2004).

[20] J.L. Wood, A.M. Oros-Peusquens, R. Zaballa, J.M. Allmond, and W.D. Kulp, Phys. Rev. C **70**, 024308 (2004).

[21] J.L. Wood, *et al.*, Phys. Repts. **215**, 101 (1992).

[22] C.Y. Wu, D. Cline, *et al.*, Nucl. Phys. A **607**, 178 (1996).

[23] C. Fahlander, I. Thorslund, B. Varnestig, A. Bäcklin, L.E. Svensson, D. Disdier, L. Kraus, I. Linck, N. Schultz, J. Pedersen, and D. Cline, Nucl. Phys A **537**, 183 (1992).

[24] I. Thorslund, C. Fahlander, A. Bäcklin, B. Kotlinski, D. Cline, A.T. Renalds, and E.G. Vogt, Z. Phys, A **342**, 35 (1992).

[25] T. Ichihara, H. Sakaguchi, M. Nakamura, M. Yosoi, M. Ieiri, Y. Takeuchi, H. Togawa, T. Tsustsumi, and S. Kobayashi, Phys. Rev. C **36**, 1754 (1987).

[26] F.K. McGowan, W.T. Milner, R.L. Robinson, P.H. Stelson, and Z. Grabowski, Nucl. Phys. A **297**, 51 (1978).

[27] H.J. Wollersheim and T.W. Elze, Z. Phys. A **280**, 277 (1977).

[28] C. Baktash, J.X. Saladin, J. O'Brien, I.Y. Lee, and J.E. Holden, Phys. Rev. C **10**, 2265 (1974).

[29] C.E. Bemis, P.H. Stelson, F.K. McGowan, W.T. Milner, J.L.C. Ford, R.L. Robinson, and W. Tuttle, Phys. Rev. C **8**, 1934 (1973).

[30] J.M. Domingos, G.D. Symons, and A.C. Douglas, Nucl. Phys. A **180**, 600 (1972).

[31] P.O. Tjøm and B. Elbek, Nucl. Phys. A **107**, 385 (1968).

[32] S. Raman, C.W. Nestor, Jr., and P. Tikkanen, At. Data Nucl. Data Tables **78**, 1 (2001).

[33] D.G. Burke, Phys. Rev. C **66**, 039801 (2002).

[34] C.Y. Wu, D. Cline, Phys. Rev. C **66**, 039802 (2002).

[35] D.G. Burke, Phys. Lett. B **406**, 200 (1997).

[36] C.Y. Wu and D. Cline, Phys. Lett. B **382**, 214 (1996).

[37] W. Andrejtscheff and P. Petkov, Phys. Rev. C **48**, 2531 (1993).

[38] F.T. Baker *et al.*, Nucl. Phys. A **501**, 546 (1989);
F.T. Baker *et al.*, ibid. A **258**, 43 (1976).

[39] R.D. Bagnell, *et al.*, Phys. Rev. C **20**, 42 (1979).

[40] D.G. Burke, Phys. Rev. Lett. **73**, 1899 (1994).

VITA

James Mitchell Allmond (known to friends as Mitch) was born in Augusta, Georgia to parents Don Allmond and Karen Hill. He was raised on a thoroughbred farm (along with two sisters, Natalie and Krista) outside the city which cultured his fondness for nature and the outdoors. A keen interest in mechanics was also developed by building structures and maintaining equipment on the farm. After high school, Mitch moved to Atlanta, Georgia where he completed his studies at The Georgia Institute of Technology.